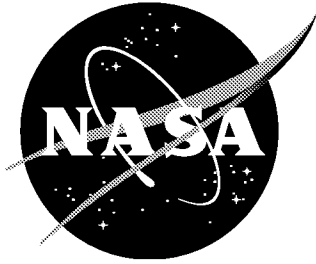


NASA/CR-2000-210116



# Identification of Terrestrial Reflectance From Remote Sensing

*R. Alter-Gartenberg and Scott R. Nolf  
Computer Sciences Corporation, Hampton, Virginia*

---

May 2000

## The NASA STI Program Office ... in Profile

Since its founding, NASA has been dedicated to the advancement of aeronautics and space science. The NASA Scientific and Technical Information (STI) Program Office plays a key part in helping NASA maintain this important role.

The NASA STI Program Office is operated by Langley Research Center, the lead center for NASA's scientific and technical information. The NASA STI Program Office provides access to the NASA STI Database, the largest collection of aeronautical and space science STI in the world. The Program Office is also NASA's institutional mechanism for disseminating the results of its research and development activities. These results are published by NASA in the NASA STI Report Series, which includes the following report types:

- **TECHNICAL PUBLICATION.** Reports of completed research or a major significant phase of research that present the results of NASA programs and include extensive data or theoretical analysis. Includes compilations of significant scientific and technical data and information deemed to be of continuing reference value. NASA counterpart of peer-reviewed formal professional papers, but having less stringent limitations on manuscript length and extent of graphic presentations.
- **TECHNICAL MEMORANDUM.** Scientific and technical findings that are preliminary or of specialized interest, e.g., quick release reports, working papers, and bibliographies that contain minimal annotation. Does not contain extensive analysis.
- **CONTRACTOR REPORT.** Scientific and technical findings by NASA-sponsored contractors and grantees.

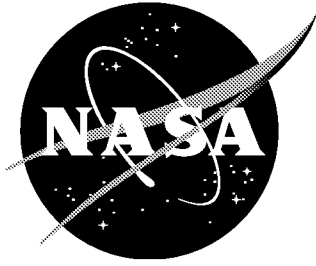
- **CONFERENCE PUBLICATION.** Collected papers from scientific and technical conferences, symposia, seminars, or other meetings sponsored or co-sponsored by NASA.
- **SPECIAL PUBLICATION.** Scientific, technical, or historical information from NASA programs, projects, and missions, often concerned with subjects having substantial public interest.
- **TECHNICAL TRANSLATION.** English-language translations of foreign scientific and technical material pertinent to NASA's mission.

Specialized services that complement the STI Program Office's diverse offerings include creating custom thesauri, building customized databases, organizing and publishing research results ... even providing videos.

For more information about the NASA STI Program Office, see the following:

- Access the NASA STI Program Home Page at <http://www.sti.nasa.gov>
- E-mail your question via the Internet to [help@sti.nasa.gov](mailto:help@sti.nasa.gov)
- Fax your question to the NASA STI Help Desk at (301) 621-0134
- Phone the NASA STI Help Desk at (301) 621-0390
- Write to:  
NASA STI Help Desk  
NASA Center for Aerospace Information  
7121 Standard Drive  
Hanover, MD 21076-1320

NASA/CR-2000-210116



# Identification of Terrestrial Reflectance From Remote Sensing

*Rachel Alter-Gartenberg and Scott R. Nolf  
Computer Sciences Corporation, Hampton, Virginia*

National Aeronautics and  
Space Administration

Langley Research Center  
Hampton, Virginia 23681-2199

Prepared for Langley Research Center  
under Contract NAS1-20431

---

May 2000

---

Available from:

NASA Center for AeroSpace Information (CASI)  
7121 Standard Drive  
Hanover, MD 21076-1320  
(301) 621-0390

National Technical Information Service (NTIS)  
5285 Port Royal Road  
Springfield, VA 22161-2171  
(703) 605-6000

# Contents

<b>1</b>	<b>Introduction</b>	<b>3</b>
<b>2</b>	<b>Remote-Sensing Imagery</b>	<b>4</b>
2.1	Irradiance . . . . .	5
2.2	Radiance . . . . .	8
2.3	Adjacency Effects . . . . .	11
2.4	Apparent Reflectance . . . . .	17
<b>3</b>	<b>Simulation</b>	<b>20</b>
3.1	Radiometry and Sensors . . . . .	20
3.2	Assumptions . . . . .	22
3.3	The Spatio-Spectral Target . . . . .	24
<b>4</b>	<b>Atmospheric Correction Techniques</b>	<b>26</b>
4.1	Bowker Reflectance Recovery Technique . . . . .	26
4.2	Richter Reflectance Recovery Technique . . . . .	27
4.3	Assessment Tools . . . . .	30
<b>5</b>	<b>Deterministic Evaluation</b>	<b>31</b>
5.1	Spectral Assessment . . . . .	31
5.2	Spatio-Spectral Assessment . . . . .	31
<b>6</b>	<b>Stochastic Evaluation of the Bowker Technique</b>	<b>35</b>
6.1	End-to-End Stochastic Simulation . . . . .	36
<b>7</b>	<b>Stochastic Evaluation of the Richter Technique</b>	<b>39</b>
7.1	End-to-End Stochastic Simulation . . . . .	39
7.2	Sensitivity to Sensor Noise . . . . .	42

7.3	Perturbation of the Initial Reflectance Signature . . . . .	48
7.4	Perturbations in the Atmospheric Conditions . . . . .	51
7.5	Incorrect Acquisition Assumptions . . . . .	54
<b>8</b>	<b>Summary</b>	<b>58</b>
<b>A</b>	<b>Appendix:</b>	
	<b>Assessment Tables</b>	<b>59</b>
A.1	Deterministic Recovery Summary . . . . .	59
A.2	Bowker Recovery with Known Reflectance Signatures . . . . .	60
A.3	Richter Reflectance Recovery Summary . . . . .	70

# Identification of Terrestrial Reflectance from Remote Sensing

Rachel Alter-Gartenberg and Scott R. Nolf

Computer Sciences Corporation, 3217 N. Armistead Ave., Hampton, VA 23666.

## Abstract

Correcting for atmospheric effects is an essential part of surface-reflectance recovery from radiance measurements. Model-based atmospheric correction techniques improve the accuracy of the identification and classification of terrestrial reflectances from multi-spectral imagery. Successful and efficient removal of atmospheric effects from remote-sensing data is a key factor in the success of Earth observation missions. This report assesses the performance, robustness and sensitivity of two atmospheric-correction and reflectance-recovery techniques as part of an end-to-end simulation of hyper-spectral acquisition, identification and classification.

## 1 Introduction

One of the tasks of space-borne Earth observation systems is mapping and monitoring changes in terrestrial reflectances. Future hyper-spectral remote-sensing imagery will record solar radiance reflected by the Earth and scattered by the atmosphere, using up to 250 spectral channels from the near UV through the visible to the short-wavelength IR ( $0.4 - 3.0\mu m$ ). The atmosphere attenuates the irradiance reflected from the ground and creates a path scattered contribution in the received signal, which has little to do with the underlying surface. Therefore, any meaningful identification and classification of terrestrial reflectances from remote sensing imaging under varying atmospheric conditions requires a model-based atmospheric radiative transfer correction technique, which accounts for the atmospheric attenuation and scattering.

This report presents a spatio-spectral sensitivity assessment of two atmospheric correction techniques in the context of an end-to-end hyper-spectral reflectance recovery simulation. The sensitivity assessment begins with 1-D deterministic assessments of spectral reflectance recovery and extends to stochastic assessments of the recovery of 3-D spatio-spectral image cubes. The acquisition model includes deterministic and stochastic presentations of randomly selected terrestrial reflectance image cubes, simulation of various

atmospheric conditions, the subsequent deterministic and stochastic simulations of the atmospheric effects, and the simulation of the spectral filtering and spatial optical filtering for each spectral band. This report uses the MODTRAN 3.7 software package as the atmospheric radiative transfer model [1], which is an evolutionary development of LOWTRAN [2], to compute the irradiance at the surface, the transmittance, and the beam and path radiance components, which comprise the measured total radiance at the observer's location for a given surface.

This report further assesses the ability of the atmospheric-correction and reflectance-recovery techniques to restore and identify the initial reflectance, and their sensitivity to uncertainty in the atmospheric conditions. The reflectance-recovery techniques include Bowker's correction technique [3, 4] which is based on a relatively simple modeling of the atmospheric effects, and the more recent Richter's correction technique [5, 6] which is based on a heuristic modeling of the same atmospheric effects. Following Slater's formulation [7], the end-to-end modeling presented here extends previous work by Bowker *et. al* [3, 4] and Huck *et. al* [8, 9] to include a more detailed and realistic simulation and evaluation of the atmospheric effects. Ground reflectances are obtained from a data-base of reflectance signatures [4]. The results assess the correct identification and classification of 27 pre-selected terrestrial reflectances from their measured radiance. Finally, the report assesses the robustness and sensitivity of each technique to uncertainties related to the acquisition conditions.

## 2 Remote-Sensing Imagery

A general model-based expression for the acquisition process of a hyper-spectral cube typically considers the following components: the spectral distribution on the irradiance on the target surface  $E(\lambda)$ , the atmospheric transmittance  $T(\lambda)$ , the spectral reflectance of the target  $\rho(x, y, \lambda)$  at an  $(x, y)$  spatial location, the spectral sensor response of each channel  $\Phi_i(\lambda)$  which defines the spectral center wavelength  $\lambda_i$ , and the spatial response of the optics  $\tau_g(x, y; \lambda_i)$  at each center wavelength  $\lambda_i$ , as given by

$$L_m(x, y; \lambda_i) = \tau_g(x, y; \lambda_i) * \int_{\lambda} E(\lambda) T(\lambda) \rho(x, y, \lambda) [\Phi_i(\lambda) + n_{\Phi_i}(\lambda)] d\lambda + n_g(x, y; \lambda_i). \quad (1)$$

The image-cube  $L_m(x, y, \lambda_i)$  is the radiance measurement of the average surface reflectance at the center wavelength of the  $i$ th channel at the spatial location  $(x, y)$ , and  $*$  denotes spatial convolution of the measured radiance with the optical response  $\tau_g(x, y; \lambda_i)$  for the  $i$ th spectral channel. The hyper-spectral model recognizes two separate noise sources, the spectral sensor noise  $n_{\Phi_i}$  associated with the sensor for the  $i$ th spectral channel, and the spatial electronic noise  $n_g(x, y; \lambda_i)$  associated with the optical image at



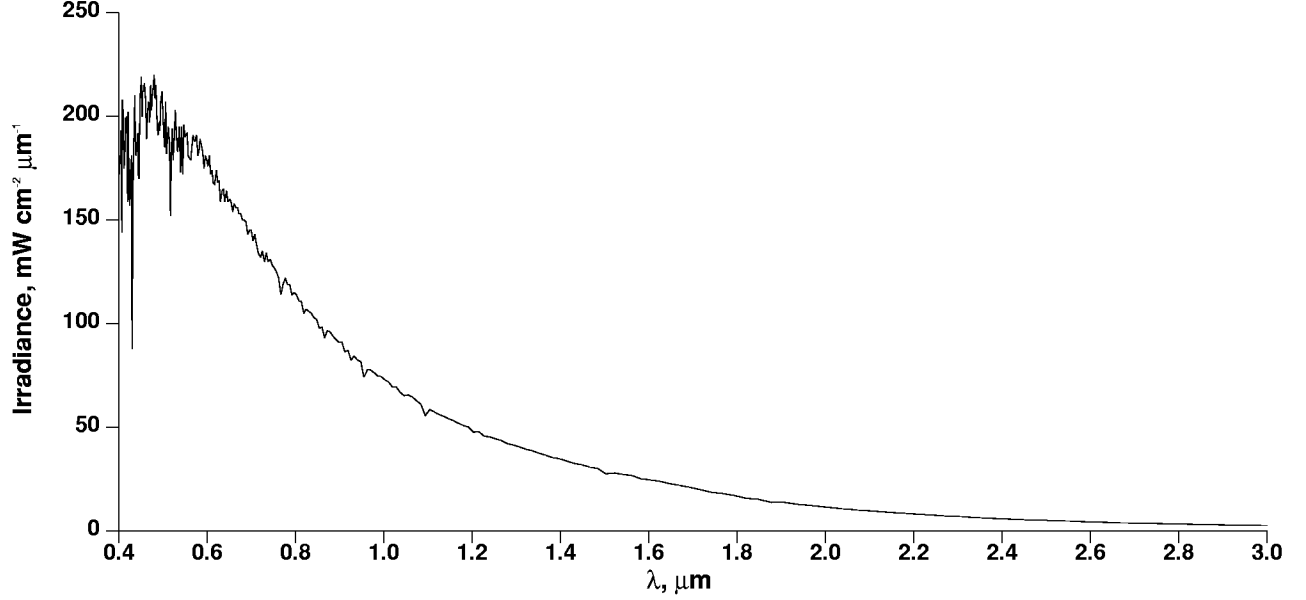


Figure 1: Exoatmospheric solar irradiance flux  $E_s(\lambda)$  for a solar zenith angle of  $0^\circ$  and  $d = 1$ .

the  $i$ th spectral band. The following sub-sections model the various components that define the measured radiance  $L(x, y, \lambda)$  in the context of remote-sensing imagery.

## 2.1 Irradiance

The exoatmospheric solar irradiance (solar irradiance outside the atmosphere)  $E_s(\lambda)$ , illustrated in Fig. 1, is attenuated by the atmosphere on its path to the Earth's surface. The global solar flux (irradiance) on the surface is the sum of the direct (non-scattered) and diffuse (sky) irradiances,

$$E(\lambda) = E_d(\lambda) + E_p(\lambda). \quad (2)$$

The direct irradiance for a solar zenith angle of  $\theta_z$  is given by [7]

$$E_d(\lambda, T_d; \theta_z, d) = \frac{E_s(\lambda) \cos(\theta_z)}{d^2} T_d(\lambda; \theta_z), \quad (3)$$

where  $d$  is the ratio of the Sun-Earth distance at a given date to its mean value, and  $T_d(\lambda)$  is the direct Sun-to-surface atmospheric transmittance, given as a function of the atmospheric optical depth  $\tau(\lambda)$  by

$$T_d(\lambda, \tau; \theta_z) = \exp \left\{ -\frac{\tau(\lambda)}{\cos(\theta_z)} \right\}. \quad (4)$$

The indirect (diffuse) irradiance component  $E_p(\lambda)$ , often called the “sky” irradiance, also contributes to the total irradiance at the surface. Diffuse irradiance is caused by multiple scattering of photons on their way through the atmosphere (Rayleigh and aerosol scattering) and additional multiple scattering of photons that are first reflected from the Earth’s surface and subsequently re-scattered downward to the surface by molecules and aerosols in the atmosphere.

The optical depth  $\tau(\lambda)$  is a linear combination of the aerosol optical depth (turbidity)  $\tau_a(\lambda; V)$  and the molecular (Rayleigh) optical depth  $\tau_m(\lambda)$  [10]

$$\tau(\lambda; V) = \tau_a(\lambda; V) + \tau_m(\lambda), \quad (5)$$

where  $V$ , the atmospheric visual range, varies with the aerosol density in the boundary layer. Therefore, the atmospheric visual range  $V$ , for a given aerosol density  $\tau_a$ , is an alternative measure to  $\tau(\lambda)$ , when most of the aerosol lies in the surface boundary layer of 0 to 2km. Visual ranges considered in this report are between  $V = 5\text{km}$  (hazy condition) and  $V = 50\text{km}$  (very clear condition) in a rural atmosphere. The relationship between the visual range and the aerosol optical depth (turbidity)  $\tau_a(\lambda)$  can be obtained from the nearly linear relationship between  $\ln(V)$  and  $\ln(\tau_a)$ . The slope of this linear relationship is given by

$$S(\lambda) = \frac{\ln\{\tau_a(\lambda; V = 23)\} - \ln\{\tau_a(\lambda; V = 5)\}}{\ln(23) - \ln(5)} \quad (6)$$

and the corresponding aerosol optical depth  $\tau_a(\lambda; V)$  for a given visual range  $V$ , is given by

$$\tau_a(\lambda; V) = \tau_a(\lambda; V = 5) \left(\frac{V}{5}\right)^{S(\lambda)}. \quad (7)$$

Although visual range and visibility are not equivalent [1], this report terms visual range as visibility. Bearing in mind that a clear visibility at the surface does not account for a potential thick layer of aerosol higher in the atmosphere, our modular and robust simulation can incorporate aerosol layers anywhere in the atmosphere.

Figure 2 illustrates the total, direct and diffuse components of the irradiance at the Earth for surface reflectances of 0.1, 0.4, and 0.7 respectively, for a solar zenith angle of  $\theta_z = 30^\circ$ , and for visibilities of  $V = 23\text{km}$  and  $5\text{km}$  respectively. The irradiance is calculated for the 93rd day of the year (April 3), when the Earth is at its mean distance from the Sun ( $d = 1$ ). The attenuation of the irradiance from about  $230 \text{ mW cm}^{-2} \mu\text{m}^{-1}$  at  $\lambda = 0.5\mu\text{m}$  (Fig. 1) to about  $170 \text{ mW cm}^{-2} \mu\text{m}^{-1}$  for  $V = 23\text{km}$  (Fig. 2 top) and  $140 \text{ mW cm}^{-2} \mu\text{m}^{-1}$  for  $V = 5\text{km}$  (Fig. 2 bottom) is due to molecular and aerosol attenuation and scattering. The direct irradiance for the lower visibility conditions decreases, while the diffuse component increases considerably, relative to these components for the higher visibility condition. Fig. 2 also shows

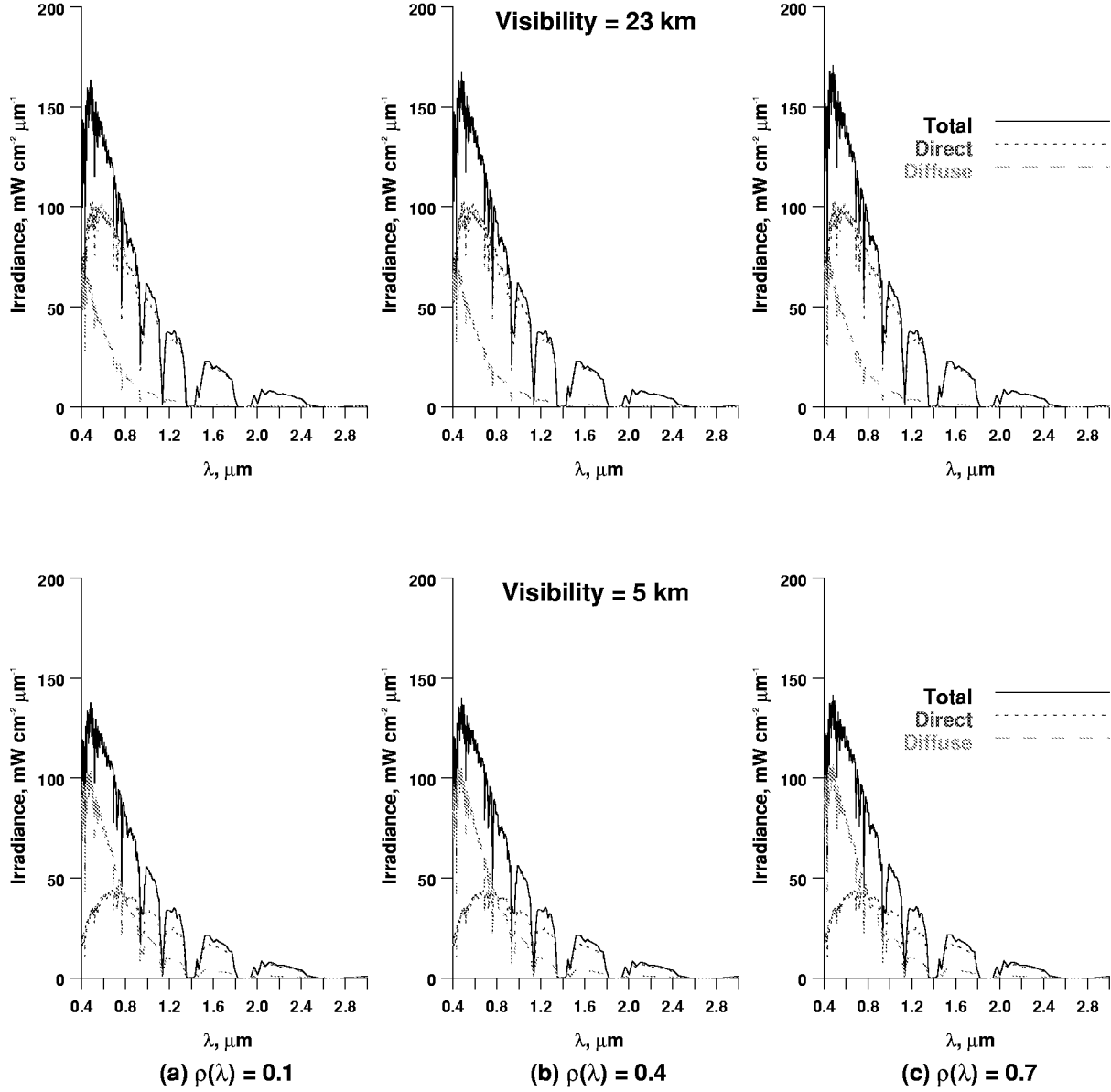


Figure 2: Total, direct and diffuse components of the solar irradiance,  $E(\lambda)$ ,  $E_d(\lambda)$  and  $E_p(\lambda)$ , for  $\theta_z = 30^\circ$  and a surface reflectance of (a)  $\rho(\lambda) = 0.1$ , (b)  $\rho(\lambda) = 0.4$ , and (c)  $\rho(\lambda) = 0.7$ .

Species	Band ( $\mu m$ )
$O_2$	0.688
$H_2O$	0.721
$O_2$	0.762–0.767
$H_2O$ in lower atmosphere	0.919
$O_2$	0.933–0.978
$H_2O$	1.114–1.157
$H_2O$	1.179
$O_2$ and a $CO_2$	1.322–1.503
$H_2O$	1.794–2.003
$CO_2$ and $H_2O$	2.072
$H_2O$	2.402–2.7
$CO_2$ and $H_2O$	2.7–3.0

Table 1: Significant molecular absorption bands in the spectral region of  $0.4 - 3.0\mu m$

that the direct irradiance on a clear day (e.g., visibility of  $V = 23\text{km}$ ) exceeds the diffuse irradiance at all wavelengths  $\lambda > 0.45\mu m$ , whereas on a hazy day (e.g., visibility of  $V = 5\text{km}$ ), the diffuse irradiance exceeds the direct irradiance at all wavelengths  $\lambda < 0.7\mu m$ , regardless of the magnitude of the surface reflectance. The sensitivity of the irradiance components to the original reflectance  $\rho(\lambda)$  is minimal. Regions of significant molecular absorption are evident from the dips in the total solar irradiance curves, and are summarized in Table 1.

## 2.2 Radiance

Assuming Lambertian reflectance  $\rho(\lambda)$ , the surface radiance, as measured on the ground, is given by

$$L_s(\lambda) = \pi^{-1} E(\lambda) \rho(\lambda) \quad (8)$$

where  $E(\lambda)$  is the surface global irradiance given by Eq. 2. When viewed by a remote sensor, the total measured radiance  $L_T(\lambda)$  is the sum of the beam and path radiances  $L_b(\lambda)$  and  $L_p(\lambda)$ ,

$$L_T(\lambda) = L_b(\lambda) + L_p(\lambda). \quad (9)$$

The beam radiance is made up of photons that are reflected from the surface and transmitted directly to the remote sensor without further scattering in that direction,

$$\begin{aligned} L_b(\lambda) &= L_s(\lambda)T_b(\lambda) \\ &= \pi^{-1}E(\lambda)\rho(\lambda)T_b(\lambda), \end{aligned} \tag{10}$$

where  $T_b(\lambda)$ , the surface-to-sensor atmospheric transmittance, is given by Eq. 4 when the zenith angle is replaced with the nadir-viewing angle. The path radiance  $L_p(\lambda)$  consists of photons that are either back-scattered off the atmosphere, emitted by the atmosphere, or surface-reflected and subsequently scattered by the atmosphere on their way to the sensor. All path-radiance photons constitute a noise source, which interferes with the inference of the actual surface reflectance  $\rho(\lambda)$ . For the range of wavelengths considered in this study, the fraction of photons emitted by the atmosphere as thermal energy is negligible, whereas the back-scattered and path-scattered photons are significant, especially at the shorter wavelengths. As a result, the path radiance  $L_p(\lambda)$  is given by

$$\begin{aligned} L_p(\lambda) &= L_o(\lambda) + L_s(\lambda)T_p(\lambda) \\ &= L_o(\lambda) + \pi^{-1}E(\lambda)\rho(\lambda)T_p(\lambda), \end{aligned} \tag{11}$$

where  $L_o(\lambda)$  is the radiance of a zero-reflectance (black body) target viewed through the atmosphere, and  $T_p(\lambda)$  is the diffuse transmittance. The zero-reflectance radiance  $L_o(\lambda)$  consists solely of photons that are back-scattered off the atmosphere, independent of the reflectance of the underlying surface. Therefore, its magnitude depends only on the solar zenith angle, the aerosol density and the sensor viewing geometry.

Figure 3 illustrates the path and beam radiance components for surface reflectance of  $\rho(\lambda) = 0.1$ , 0.4, and 0.7, with visibilities of 23km (top) and 5km visibility (bottom). In general, information about the surface is contained mainly in the beam radiance, while the path radiance consists mostly of light scattered into the path from the atmosphere and from the surrounding reflectances. Both the beam and the path radiances increase with increasing surface reflectance, where the path radiance contribution decreases with increasing wavelength due to diminished scattering at longer wavelengths. The relative contributions of beam and path radiance components however, vary significantly with changes in the visibility conditions. The wavelength beyond which the magnitude of the beam component exceeds that of the path component decreases with increasing surface reflectance, due to the higher fraction of beam radiance at longer wavelengths. For the 23km-visibility case, the cross-over wavelengths are 0.6, 0.47, and 0.43  $\mu m$ , for  $\rho(\lambda) = 0.1$ , 0.4, and 0.7 respectively. For the 5km-visibility case, the respective cross-over wavelengths shift to 1.1, 0.87, and 0.82  $\mu m$ , respectively, demonstrating the more dominant role of path

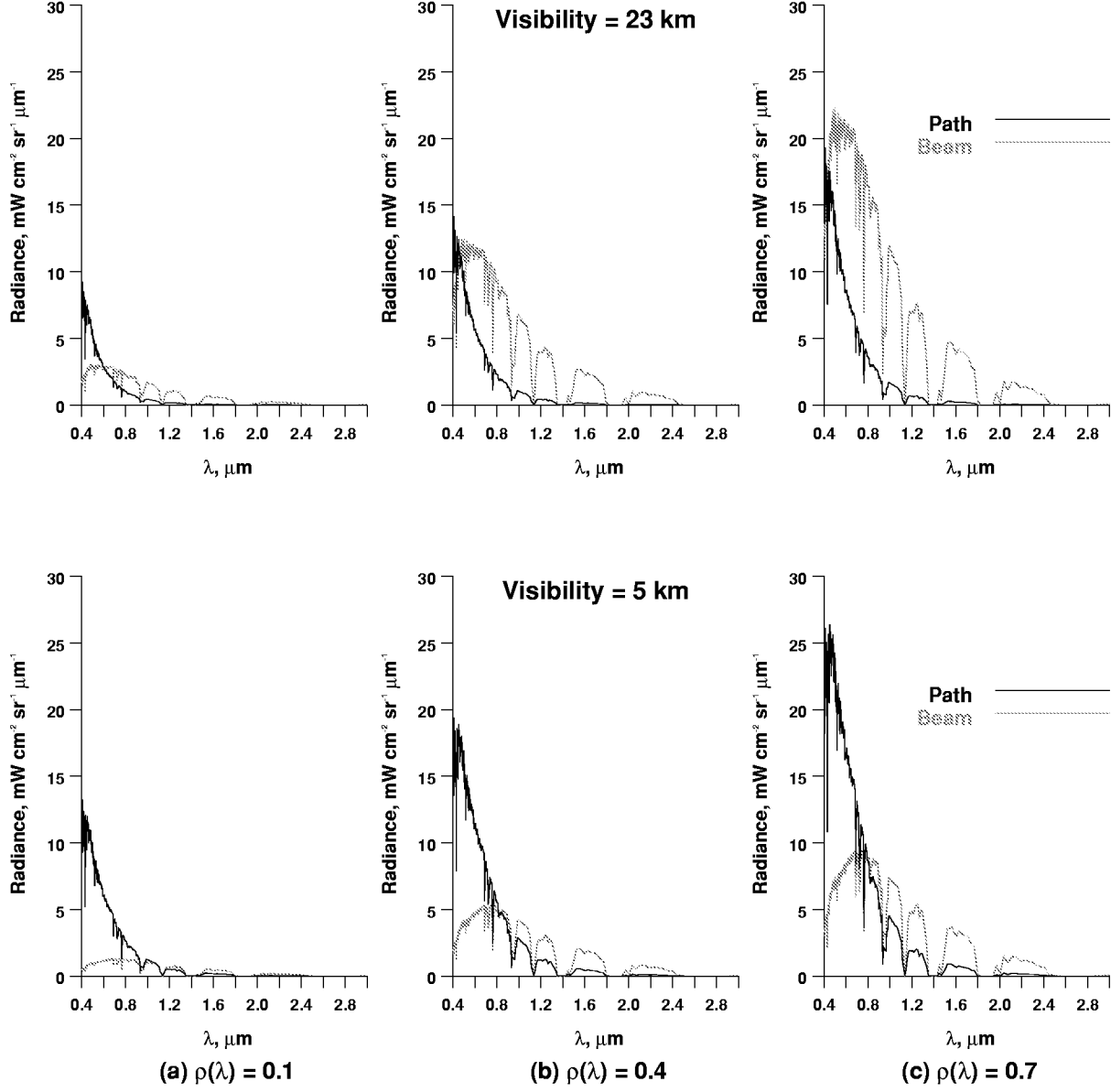


Figure 3: Beam and path radiance components,  $L_p$  and  $L_b$ , for  $V = 23\text{ km}$  (top) and  $V = 5\text{ km}$  (bottom),  $\theta_z = 30^\circ$  and (a)  $\rho(\lambda) = 0.1$ , (b)  $\rho(\lambda) = 0.4$ , and (c)  $\rho(\lambda) = 0.7$ .

radiance in low-visibility conditions. For example, for the 5km visibility case, the path radiance exceeds the beam radiance at all wavelengths in the visible region.

### 2.3 Adjacency Effects

The above 1-D spectral model does not account for the effects of radiance contributions from surrounding pixels (adjacency effects [11]). The MODTRAN package computes each of the model's 1-D components independent of the surrounding spatial contributions, whereas radiance contributions from surrounding pixels are similar to the effects of spatial optical blurring [11]. Kaufman's empirical approximation of the adjacency effects for a square target of edge-length  $l$  with a uniform reflectance  $\rho_f$ , surrounded by a uniform background reflectance  $\rho_b$ , as a function of the molecular (Rayleigh) and aerosol optical thickness  $\tau_m(\lambda)$  and  $\tau_a(\lambda)$  respectively, and the molecular and aerosol average heights  $H_m$  and  $H_a$  respectively, is given by the fraction weight function  $\zeta(l, \lambda)$  [11]

$$\zeta(l, \lambda) = 0.7\tau_m(l, \lambda) \exp\left(\frac{-l}{2H_m}\right) + 0.37\tau_a(l, \lambda) \exp\left(\frac{-l}{H_a}\right) + 0.32\tau_a(l, \lambda) \exp\left(\frac{-l}{6H_a}\right). \quad (12)$$

The weight  $\zeta(l, \lambda)$  indicates the transfer fraction of the surrounding radiance fields in the measured radiance, and therefore models the measured radiance as a linear combination of the target and its adjacent fields, as given by

$$L(l, \lambda) = L(\rho_b)\zeta(l, \lambda) + L(\rho_f)[1 - \zeta(l, \lambda)]. \quad (13)$$

The molecular optical thickness  $\tau_m(\lambda)$  is not affected by the visual range  $V$ , and can be obtained by  $\tau_m(\lambda) = -\ln(T_m(\lambda))$ , where  $T_m(\lambda)$  is the molecular transmittance of the atmosphere between the observer and sea level. Similarly, the aerosol transmittance, a part of the direct surface-to-sensor path atmospheric transmittance (Eq. 11) for a given visibility condition  $V$ , can be extracted using Eq. 4 for the nadir-viewing angle, as  $\tau_a(\lambda; V) = -\ln(T_a(\lambda; V))$ , or by using Eq. 7.

Fig. 4 illustrates the  $l - \lambda$  plane of  $\zeta(l, \lambda)$  for  $V = 10\text{km}$ , assuming  $H_m = 8\text{km}$ , and  $H_a = 2\text{km}$  as the average height of the molecular and aerosol boundary layers respectively, while Fig. 5 illustrates 1-D spatial projections of the fraction weight function  $\zeta$ . These figures show that the fraction of scattered radiance from background reflectances decreases with increasing edge-field length  $l$  and with increasing wavelength  $\lambda$ . As expected, Fig. 5(b) also shows that the fraction of scattered radiance increases with decreased visibility. However, these figures reveal unrealistically high contributions from background scattering. For example, according to this formulation, for  $\lambda = 0.4\mu\text{m}$  and  $V = 23\text{km}$ , 20% of the measured radiance of the target field with an edge-field length of 10km comes from the surrounding areas. This contribution

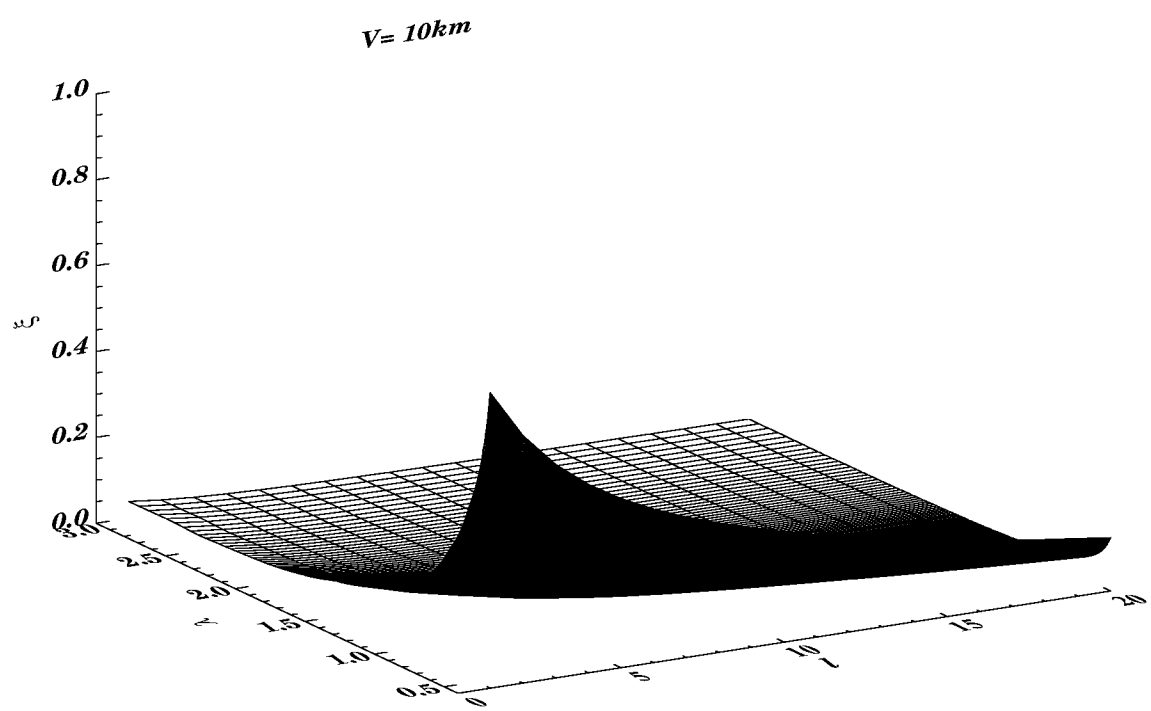


Figure 4: The transfer fraction function  $\zeta(l, \lambda)$  for 10km visibility.



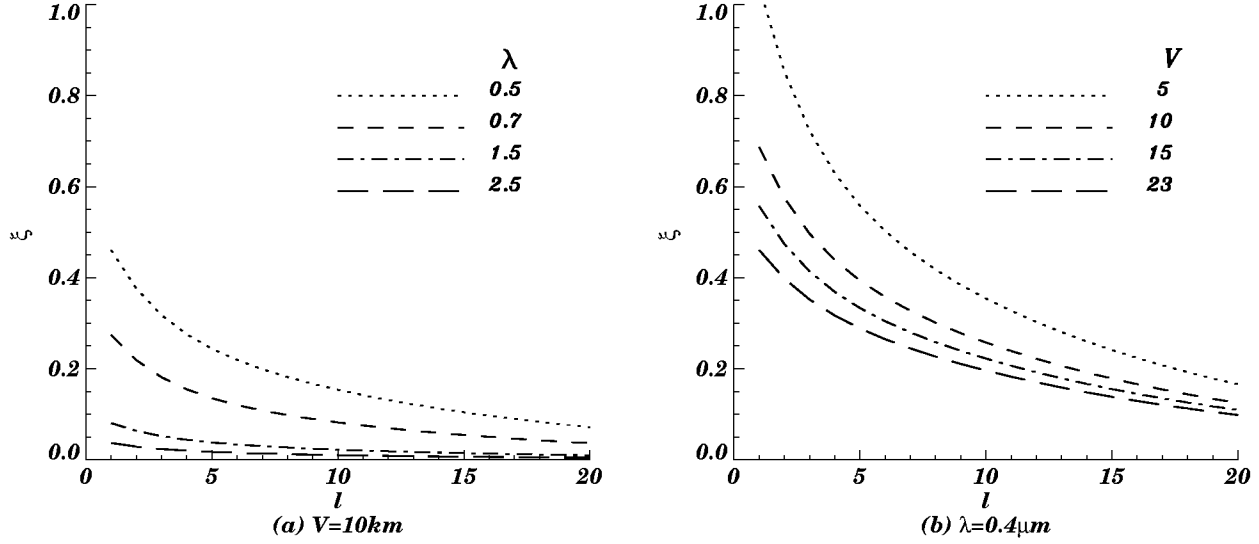


Figure 5: Projections of the transfer fraction function  $\zeta(l, \lambda)$  illustrated in Fig. 4 for (a)  $\lambda = 0.5, 0.7, 1.5$ , and  $2.5 \mu\text{m}$  for  $V = 5 \text{ km}$ , and for (b)  $V = 5, 10, 15$ , and  $23 \text{ km}$  for  $\lambda = 0.4 \mu\text{m}$

increases to 35% for low visibility of 5 km. Slater ([7], pp. 220) indicates that reflectances within 100 meters of the borders are affected by the adjacency effects under normal turbidity conditions. Even under zero-turbidity conditions, reflectances within ten meters of the borders are affected, and only under highly turbid conditions does this effect extends to one kilometer from the target's boundary. Therefore, while the trend of the proposed  $\zeta$ -function is correct, it requires spatial re-scaling to achieve a more realistic contributions radius.

Kaufman's model is restricted to a two-reflectance model, i.e., the target and its surround. It does not account for scattering from multiple surrounding reflectances. To overcome this limitation,  $L(\rho_f)$  and  $L(\rho_b)$  can be replaced with a spatio-spectral cube, and the weighting fraction function  $\zeta$  can be replaced by a convolution with an equivalent spatio-spectral blurring filter cube with the path radiance spatio-spectral cube  $L_p(x, y, \lambda)$ .

To extend this empirical approximation to the  $x - \lambda$  plane, the field-edge  $l$  is replaced with the scaled Euclidean distance  $d_s = s|x - x_0|$  between the spatial location  $x_0$  and all the scattering locations  $x$ ,  $-\infty < x < \infty$ , where  $s > 1$  is a spatial scale factor. For every spectral band  $\lambda$ , the extended adjacency

effects model is therefore given by

$$L(x_0; \lambda) = \frac{\int_{x, x \neq x_0} L(x; \lambda) \zeta(d_s; \lambda)}{2 \int_x \zeta(d_s; \lambda)} + \left[ 1 - \frac{\int_{x, x \neq x_0} \zeta(d_s; \lambda)}{2 \int_x \zeta(d_s; \lambda)} \right] L(x_0; \lambda), \quad (14)$$

where the normalization factor ensures that the weight of the scattered radiance remains a probability function. Consequently, Eq. 14 can be re-written as a spatial convolution between the path radiance  $L_p(x, \lambda)$  and the kernel  $Z(x, \lambda)$ , given in terms of  $d_s$  as

$$Z(d_s, \lambda) = \begin{cases} \frac{\zeta(d_s, \lambda)}{\int_d \zeta(d_s, \lambda)} & \text{for } d \neq 0 \\ 1 - \frac{\int_{d, d \neq 0} \zeta(d_s, \lambda)}{\int_d \zeta(d_s, \lambda)} & d = 0 \end{cases}. \quad (15)$$

The resulting total measured radiance, after accounting for the adjacency effects, is therefore given by

$$L_T(x, \lambda) = L_b + L_p(x, \lambda) * Z(d_s, \lambda). \quad (16)$$

To account for fluctuations in the amount of scattered radiance, Eq. 16 can be replaced with

$$L_T(x, \lambda) = L_b + \left( L_p(x, \lambda) [1 + n_{L_p}(x, \lambda)] \right) * Z(d_s, \lambda), \quad (17)$$

where  $n_{L_p}$  is a uniform random white noise in the  $[-a, a]$  range,  $a < 1$ . Typical fluctuations are between  $a = 0.05$  and  $0.1$ , indicating fluctuations of 5% – 10% around the path radiance. Fig. 6 illustrates the fraction kernel  $Z(d, \lambda)$  for visibility of 10km and for  $x \geq 0$  and a spatial scale factor of  $s = 1$ . As expected, a comparison of this figure with Fig. 4 shows the same general response. Eq. 15 can be easily extended to 2-D spatial coordinates, thus obtaining the desired spatio-spectral blurring effect.

Fig. 7 illustrates the measured radiance of a spatio-spectral target of only three discrete reflectances,  $\rho(\lambda) = 0.4, 0.1$ , and  $0.7$ , each spread over 80 processing pixels for  $\theta_z = 30^\circ$ ,  $V = 5, 10$  and  $15$  km, and  $s = 2$  and  $s = 3$ . It assesses the difference between a model that ignores the adjacency effects (Eq. 9), drawn in gray, and the measured radiance which accounts for these effects (Eq. 13), drawn in black. It shows that the adjacency effects blur the transitions between reflectances. A comparison between Fig. 7(a) and (b) illustrates the spread factor control on the amount of blur. The spatial spread of the blur reduces from 20 pixels on each size of the edge for a spatial scale factor of  $s = 2$  in Fig. 7(a), to 10 pixels on each size of the edge for a spread scale factor of  $s = 3$  in Fig. 7(b). Assuming as an example remote sensing images with a resolution of 100m, this spread translates to 2km on each side of the edge for a spread scaler of  $s = 2$ ,

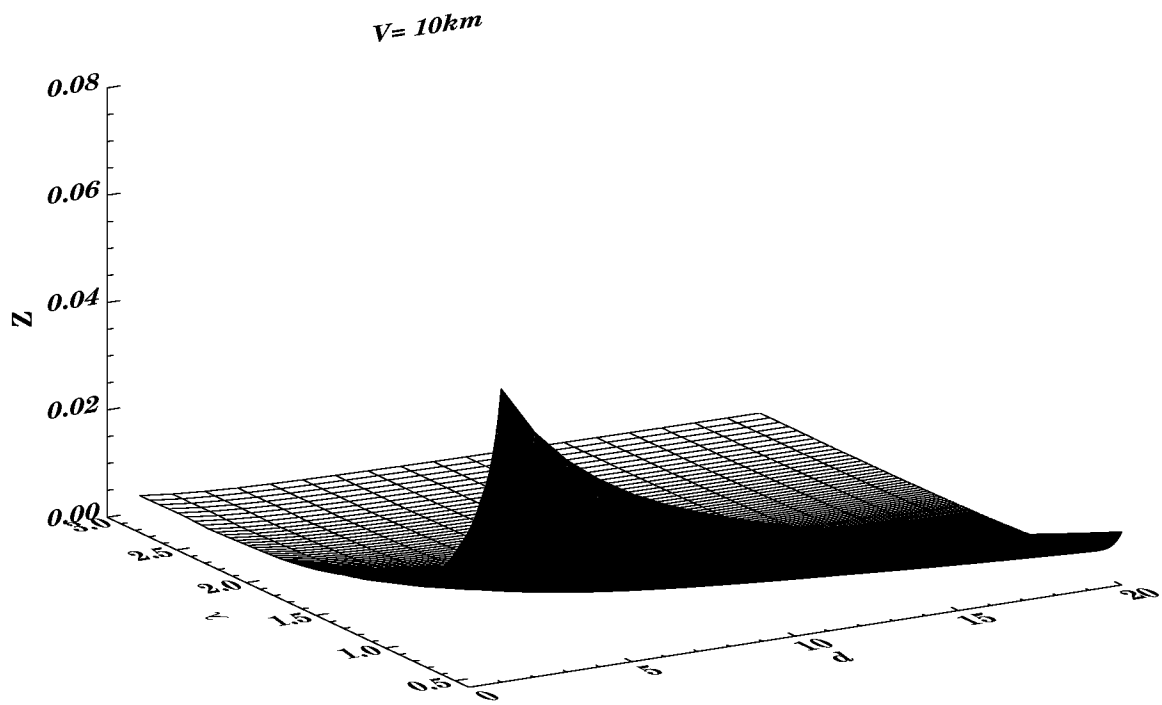


Figure 6: The kernel fraction function  $Z(d, \lambda)$  for visibility of 10km and spatial scale factor of  $s = 1$ .

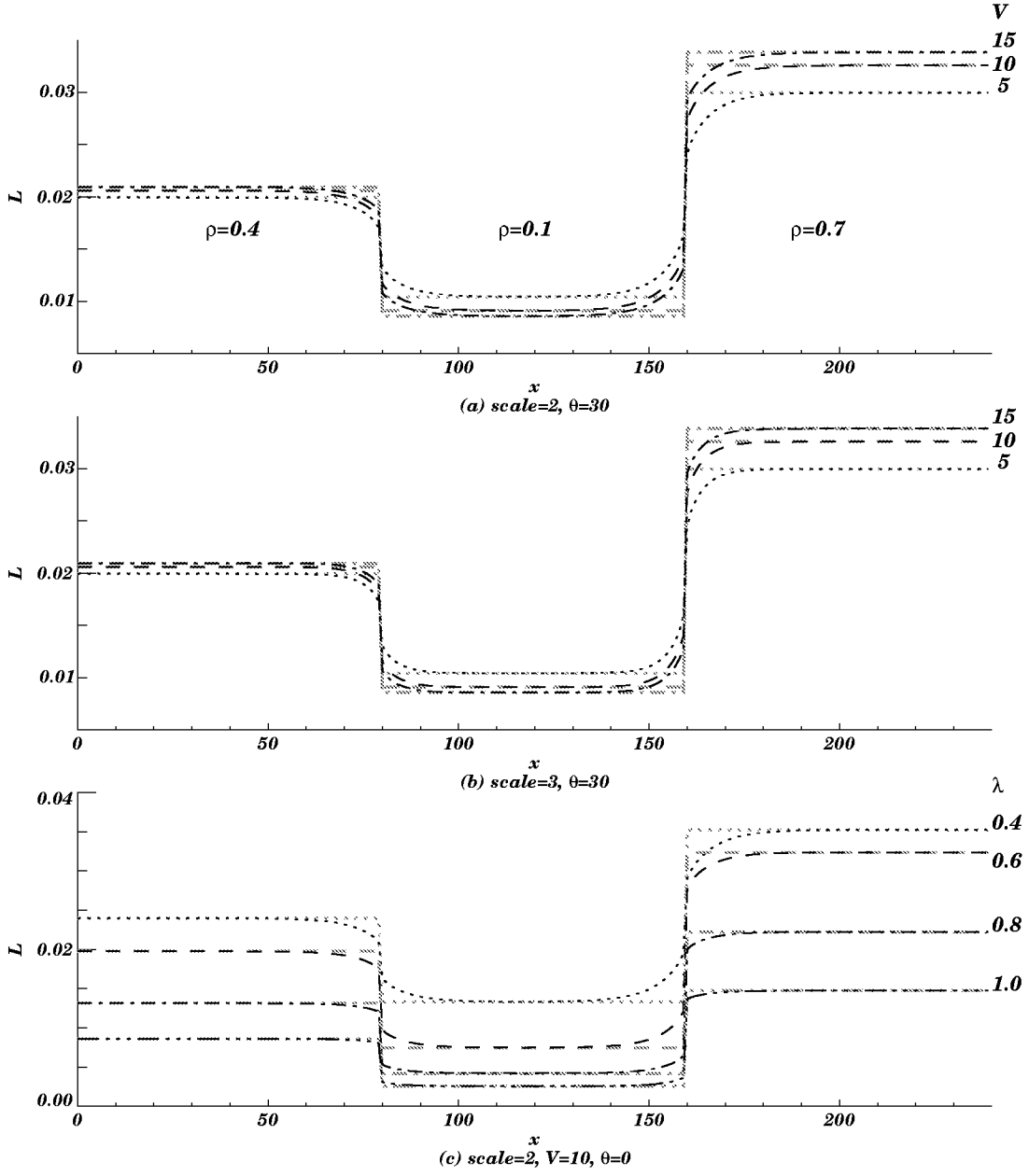


Figure 7: Measured radiance with and without adjacency effects, using Eqs. 16 and 9 respectively. (a)  $\theta_z = 30^\circ$ ,  $s = 2$ , and  $\lambda = 0.5\mu m$ , (b)  $\theta_z = 30^\circ$ ,  $s = 3$ , and  $\lambda = 0.5\mu m$ , (c)  $V = 10\text{km}$ ,  $\theta_z = 0^\circ$  and  $s = 2$  at different wavelengths.

and 1km for a spread scaler of  $s = 3$ . As expected, the amount of blur is controlled by the visibility. Both figures show that the lower the visibility, the higher the contribution from the adjacency effects. Fig. 7(c) illustrates a cut through the measured radiance for  $V = 10\text{km}$  and  $\theta_z = 0^\circ$  at different wavelengths for a scale factor of  $s = 2$ . This figure shows that adjacency blurring effects diminish with increased  $\lambda$ , as the wavelength shifts from the visible into the IR.

## 2.4 Apparent Reflectance

The apparent reflectance (albedo), as defined by

$$\rho_a(\lambda) = \frac{\pi d^2}{E_s \cos(\theta_z) \cos(\theta_s)} L_T(\lambda), \quad (18)$$

is often used to estimate the reflectance from the measured radiance  $L_T(\lambda)$ . Figure 8 illustrates the albedo dependency on surface reflectance and visibility condition, as viewed from a satellite, based on the acquisition conditions used in Fig. 2. This figure also compares the effects of stratospheric aerosol density, by simulating a case with a normal level of stratospheric aerosol (top), and the conditions following a volcanic eruption (bottom), to assess the sensitivity of the visibility parameter to layers of aerosol higher in the atmosphere. This figure shows that for rural aerosols, the albedo for low reflectance equals or exceeds the reflectance value at all wavelengths, except within the absorption band regions, and is lower for reflectances that are higher than 0.21, as illustrated in Figs. 8(b) and (c). For  $\rho(\lambda) = 0.1$ , the albedo in the visible band  $0.4\text{--}0.8\mu\text{m}$  increases as visibility decreases because the path radiance, which increases with decreased visibility, is dominant for low-reflectance conditions, as illustrated in Fig. 8(a). This phenomenon does not hold for  $\lambda > 1\mu\text{m}$ , where scattering is negligible, and the albedo is independent of turbidity, or for higher reflectances, as illustrated in Figs. 8(b) and (c), where the beam radiance is dominant and the albedo increases with increased visibility. Changes in the albedo between the top and bottom figures can be attributed to increased attenuation in the beam radiance described above, while the increase in the troughs is caused by increased back-scattering off the stratospheric aerosol.

Figure 9 illustrates the effects of the atmosphere on the albedo as a function of the sensor's altitude, for visibilities ranging from  $V = 5\text{km}$  to  $23\text{km}$ , using the same simulation conditions as in Fig. 8. The figure covers the  $0.4\text{--}0.8\mu\text{m}$  region to highlight important differences in the visible and near-IR regions of the spectrum. It demonstrates that the albedo is most sensitive to atmospheric degradation at the shortest wavelengths, due to increased scattering. For  $V = 23\text{km}$  the albedo is relatively unperturbed at wavelengths beyond 0.7, 0.57, and  $0.5\mu\text{m}$ , for  $\rho = 0.1$ , 0.4, and 0.7 respectively. This figure shows a significant increase in albedo as altitude increases and the reflectance decreases. For very low reflectances,

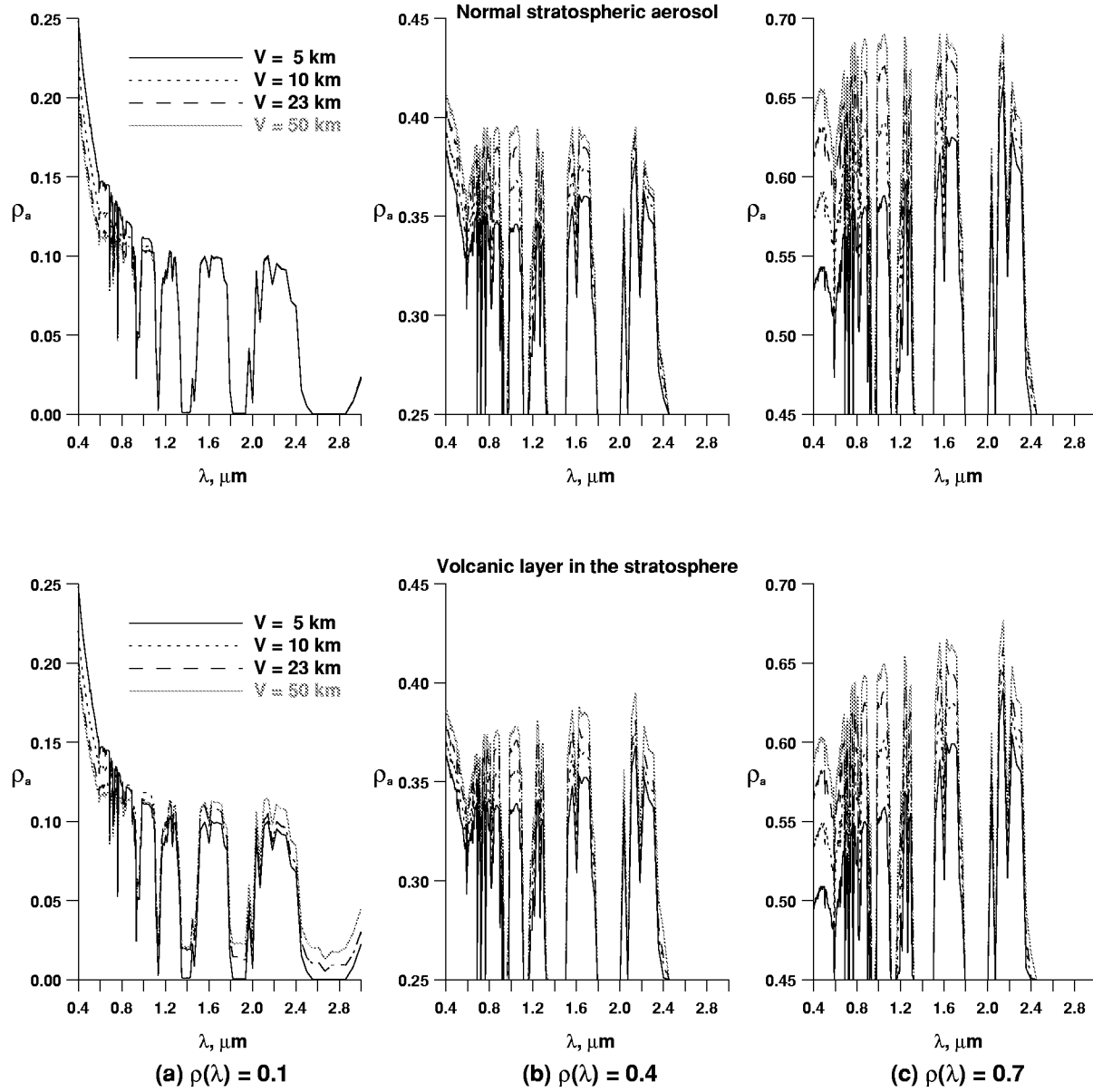


Figure 8: Apparent reflectance (albedo)  $\rho_a(\lambda)$  for a surface reflectance of (a)  $\rho(\lambda) = 0.1$ , (b)  $\rho(\lambda) = 0.4$ , and (c)  $\rho(\lambda) = 0.7$ , with visibilities of  $V = 50, 23, 10$  and  $5 \text{ km}$  in the surface boundary layer and with a normal background loading of aerosol higher in the atmosphere (top), and a thick layer of volcanic aerosol higher in the atmosphere (bottom), solar zenith angle of  $\theta_z = 30^\circ$ , and a satellite altitude of  $H = 800 \text{ km}$ .

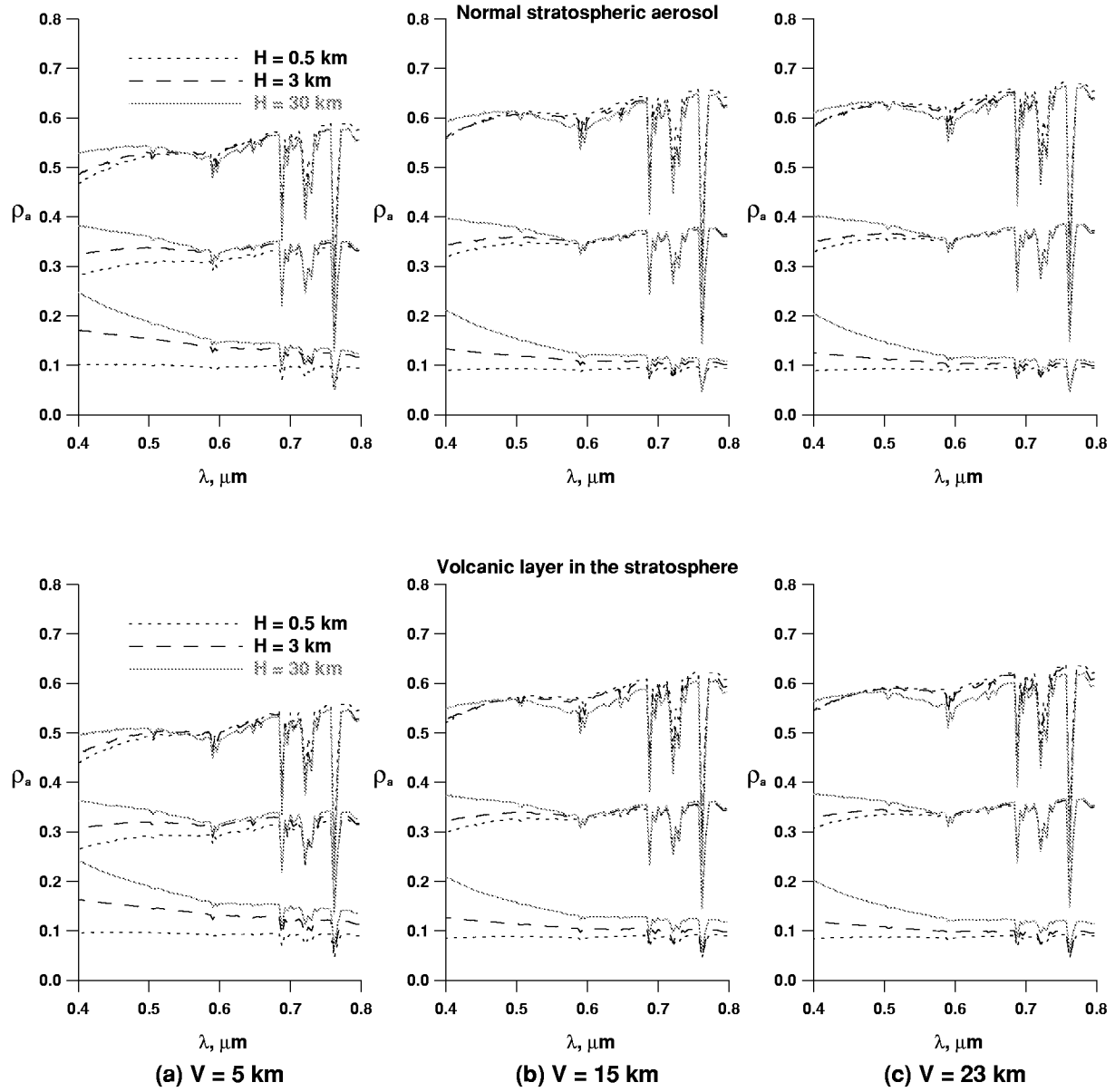


Figure 9: Apparent reflectance (albedo)  $\rho_a(\lambda)$  for a surface reflectance of  $\rho(\lambda) = 0.1, 0.4$ , and  $0.7$ , for sensor altitudes of  $H = 0.5, 3$ , and  $30$  km, solar zenith angle of  $\theta_z = 30^\circ$ , and visibility of (a)  $V = 5$  km (b)  $V = 15$  km, and (c)  $V = 23$  km

illustrated in Fig. 9(a), the albedo exceeds the true reflectance because of increased optical depth, which, in turn, increases the path radiance. With just a normal background aerosol loading higher in the atmosphere (“normal” case), this increase is negligible above 30km. Comparison of this “normal” case with that of a thick layer of volcanic aerosol shows that the albedo in the latter case is smoother than in the former. For both top and bottom sets of figures, a comparison between the albedo at  $V = 23$  and 5km for a range between  $0.57$  and  $0.7\mu m$  reveals an abrupt albedo decrease at the 30km altitude to levels that are below the 5km altitude for higher reflectances. This phenomenon is caused by the stratospheric ozone layer, which has some absorption at these wavelengths, and thus decreases the beam radiance, particularly for high reflectances. Figs. 8 and 9 clearly demonstrate the limitations of the albedo approximation, and the need to account for atmospheric degradations before the reflectance identification and classification processes take place.

### 3 Simulation

#### 3.1 Radiometry and Sensors

Substituting Eqs. 10 and 11 into Eq. 9 yields

$$\begin{aligned} L_T(\lambda) &= L_o(\lambda) + \pi^{-1}E(\lambda)\rho(\lambda) [T_b(\lambda) + T_p(\lambda)] \\ &= L_o(\lambda) + \pi^{-1}E_T(\lambda)\rho(\lambda), \end{aligned} \tag{19}$$

where

$$E_T(\lambda) = E(\lambda)T_t(\lambda) \tag{20}$$

is defined as the “effective irradiance”, and

$$T_t(\lambda) = T_b(\lambda) + T_p(\lambda), \tag{21}$$

is the corresponding total transmittance. With the definition of the “effective irradiance”  $E_T(\lambda)$ , the measured surface radiance from remote sensing  $L_T$  (Eq. 19) parallels the measured surface  $L_s$  radiance right at the ground (Eq. 8), where the irradiance  $E$  is replaced with the effective irradiance  $E_T$ , and  $L_o$  constitutes a pure scattering noise term. Fig. 10 illustrates the direct (path), diffuse and total transmittance components for  $\theta_z = 30^\circ$ ,  $V = 5$  and 23km, and  $\rho(\lambda) = 0.1, 0.4$ , and  $0.7$ , respectively. This figure shows that the total transmittance decreases with decreasing visibility. Specifically, it shows that the path component decreases while the diffuse component increases with decreasing visibility. It also shows that the effects of



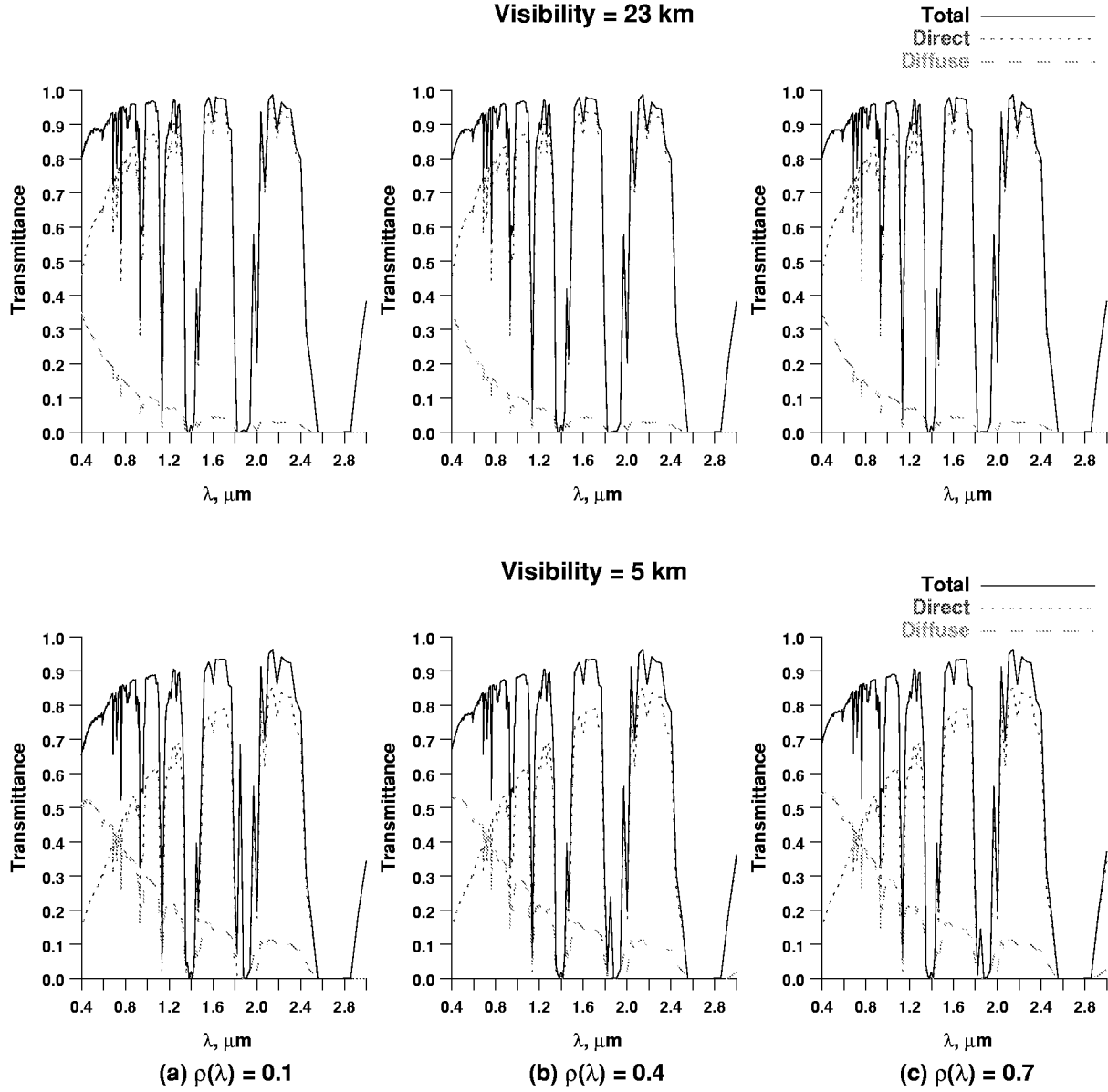


Figure 10: Total, direct (path) and diffuse transmittance components,  $T_t(\lambda)$ ,  $T_b(\lambda)$  and  $T_p(\lambda)$ , for  $\theta_z = 30^\circ$  and a surface reflectance of (a)  $\rho(\lambda) = 0.1$ , (b)  $\rho(\lambda) = 0.4$ , and (c)  $\rho(\lambda) = 0.7$ .

the diffuse transmittance diminishes at longer wavelengths. These observations help explain the decrease in the adjacency blurring effect for longer wavelengths and the blur increase with decreased visibility.

Substituting Eq. 19 into Eq. 1 yields the remote-sensing measured radiance for the  $i$ th channel,

$$L_m(x, y, \lambda_i) = \tau_g(x, y; \lambda_i) * \pi \int_{\lambda} L_T(x, y, \lambda) [\Phi_i(\lambda) + n_{\Phi_i}(\lambda)] d\lambda + n_g(x, y; \lambda_i). \quad (22)$$

The radiance-to-digital conversion for the  $i$ th channel is given by

$$L_{m_d}(x, y, \lambda_i) = L_m(x, y, \lambda_i) [c_0(i) + c_1(i)D], \quad (23)$$

where  $\lambda_i$  is the center wavelength of the  $i$ th channel,  $D$  is the digital number, and  $c_0(i)$  and  $c_1(i)$  are the offset and slope of the calibration coefficients respectively. The permissible wavelength regions to be used in Eqs. 22 and 23 exclude the natural absorption bands summarized in Table 1. Avoiding the absorption bands minimizes the errors arising from the wide variation in the atmospheric water-vapor content.

### 3.2 Assumptions

The parameters used to simulate the atmospheric acquisition conditions are:

- 93rd day of the year (April 3)
- 1976 Standard Atmosphere
- Nadir view angle of  $0^\circ$ .
- Sensor altitude of 800km.
- Solar zenith angles of  $0^\circ$ ,  $30^\circ$ , and  $45^\circ$ .
- Surface visibility 5, 10, 15, and 23km, in rural aerosol.
- Surface terrain angle of  $0^\circ$ .

To assess the correction techniques, the simulation assumes non-overlapping spectral filters  $\Phi_i(\lambda)$ , one for each spectral frequency assessed in our simulation, i.e.,  $\Phi_i(\lambda) = 0$  for the  $\lambda$  bands specified in Table 1, and  $\Phi(\lambda_i) = \delta(\lambda_i)$  for all the remaining spectral frequencies within the  $0.4 - 3.0\mu m$  range. The simulation also assumes no radiance-to-digital errors, i.e.,  $L_{m_d}(\lambda) \equiv L_m(\lambda)$ . The simulation uses the  $(x, y)$  dependency to allow a stochastic treatment of the spatial representation of the different reflectances, with uncertainty

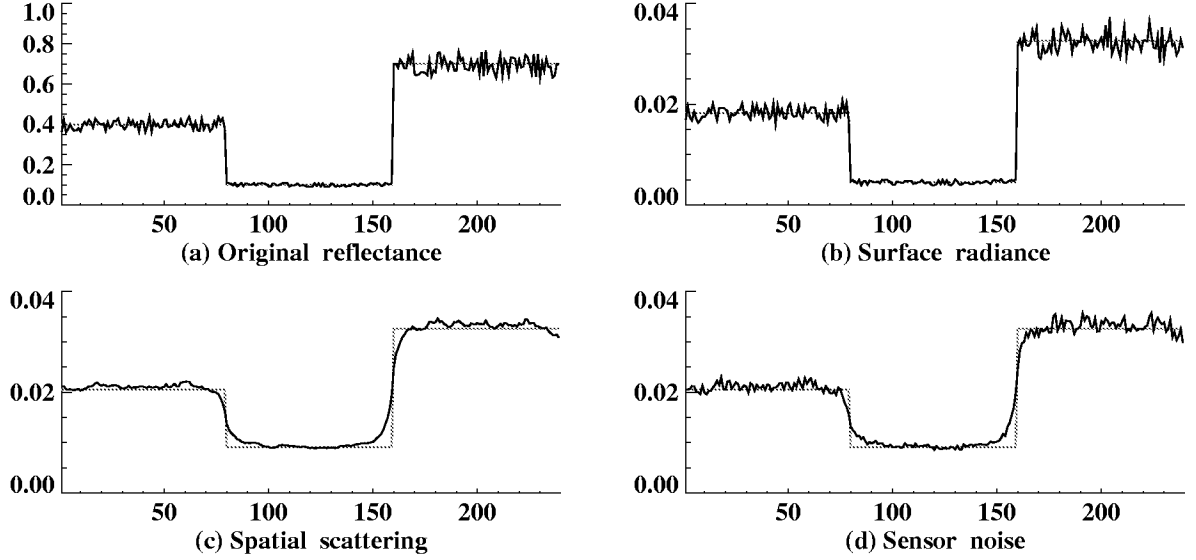


Figure 11: The simulation of Eq. 22.

around a mean value for each  $\lambda$ . Without *a priori* knowledge of the initial reflectance, the recovery techniques assume a constant initial reflectance of  $\rho(\lambda) = 0.4$  for the simulation of  $\tilde{E}(\lambda)$ , and  $\tilde{T}_p(\lambda)$ .

The simulations use targets with large mean spatial details relative to the processing (pixel) size. The discrete  $(x, y)$  locations are at the pixels' centers, and the sampling lattice is identical to the processing lattice. The spectral frequency  $\nu$  is defined with a  $\Delta\nu$  interval of  $0.0083 \text{ cm}^{-1}$ , which, in turn, defines the wavelength vector  $\lambda_i$  as  $\lambda = 1/\nu$  for the  $(0.4 - 3.0 \mu\text{m})$  range. Therefore, the numerical implementation of this simulation is dense enough in both the spatial and the spectral domains, and the signals are bandlimited to the processing passband in the spatio-spectral domains. We assume an acquisition device with a spatial-frequency response given by

$$\tau_g(v, \omega; \lambda_i) = \exp \left\{ \frac{v^2 + \omega^2}{\sigma_g^2(\lambda_i)} \right\}, \quad (24)$$

where  $\sigma_g(\lambda_i)$  is the optical-response index and  $(v, \omega)$  are given in cycles/pixel.

Figure 11 illustrates the the effects of different components in Eq. 22 on the measured radiance, using the same 240-pixels reflectance target used in Fig. 7, namely, an  $x - \lambda$  spatio-spectral target of three constant reflectances,  $\rho(\lambda) = 0.4, 0.1$ , and  $0.7$ , each spread over 80 processing pixels. Fig. 11(a) illustrates the effects of 10% fluctuations in the reflectance signature. Fig. 11(b) illustrates the effects of this uncertainty on the measured surface radiance  $L_s$ , assuming  $V = 10\text{km}$ ,  $\theta_z = 30^\circ$ , and a 5% uncertainty in the atmospheric

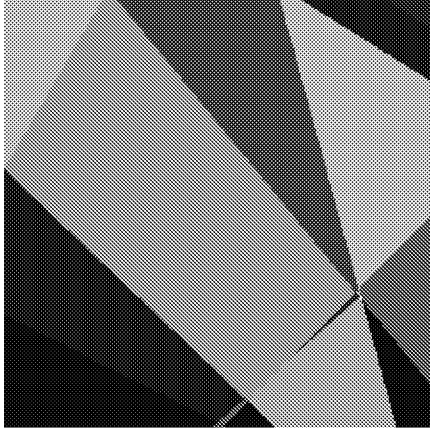


Figure 12: A random reflectance test target

conditions, simulated with 5% perturbations around the total irradiance  $E$ . Fig. 11(c) illustrates the remote-sensing measured radiance of the surface radiance measured in (b), with spatial path-radiance fluctuations  $n_{L_p}$  of 10%, and adjacency effects with a spatial scale factor of  $s = 3$ . Fig. 11(d) illustrates the addition of 5% sensor noise  $n_{\Phi_i}$  to the total measured radiance. This figure demonstrates the ability of the proposed model to simulate stochastic radiance measurement in the spatio-spectral domain.

### 3.3 The Spatio-Spectral Target

Figure 12 illustrates a 256-by-256 pixel random-polygon test target with a mean spatial detail of 40 pixels. The reflectance for each polygon is randomly selected from the set of 25 reflectance signatures listed in Table 2, where each reflectance signature response is taken from [4], and assigned a unique gray-level. The stochastic process randomly selected 14 reflectance signatures from the database, and assigned them into the randomly divided polygon areas. Subsequently, Fig. 12 visualizes a hyper-spectral random data-cube, where each of the 14 gray levels represents a unique spectral signature associated with the spatial  $(x, y)$  location. This figure is a more realistic representation of a natural target, as imaged by a remote sensing system, than the typical square uniform target with uniform background, and will be used to assess the ability to identify and classify the correct reflectance signature after implementing each of the correction techniques. Fig. 13 superimposes the boundaries of the spectral reflectance cube on the original target, identifies the spatial location of each of the 14 selected reflectance signatures, and associates the assigned gray-level with the size (in pixels) of each selected reflectance signature. Together, these figures serve as

Vegetation		Soil		Water
Crops	Forests	Identified	Samples	
Barley	American Elm	Basalt	Multi-mineral	Water
Beans	Silver Maple	Dry red clay	Whitley County	
Oats	Burr Oak	Wet red clay	Powell Grassland	
Potatoes	Ponderosa Pine	Gypsum sand	Dry sand	
Soybeans	Sycamore	Silicon sand	Wet sand	
Tobacco	Kentucky Blue Grass			
Wheat				
Fallow field				

Table 2: Reflectance signatures for the three different categories studied in this report

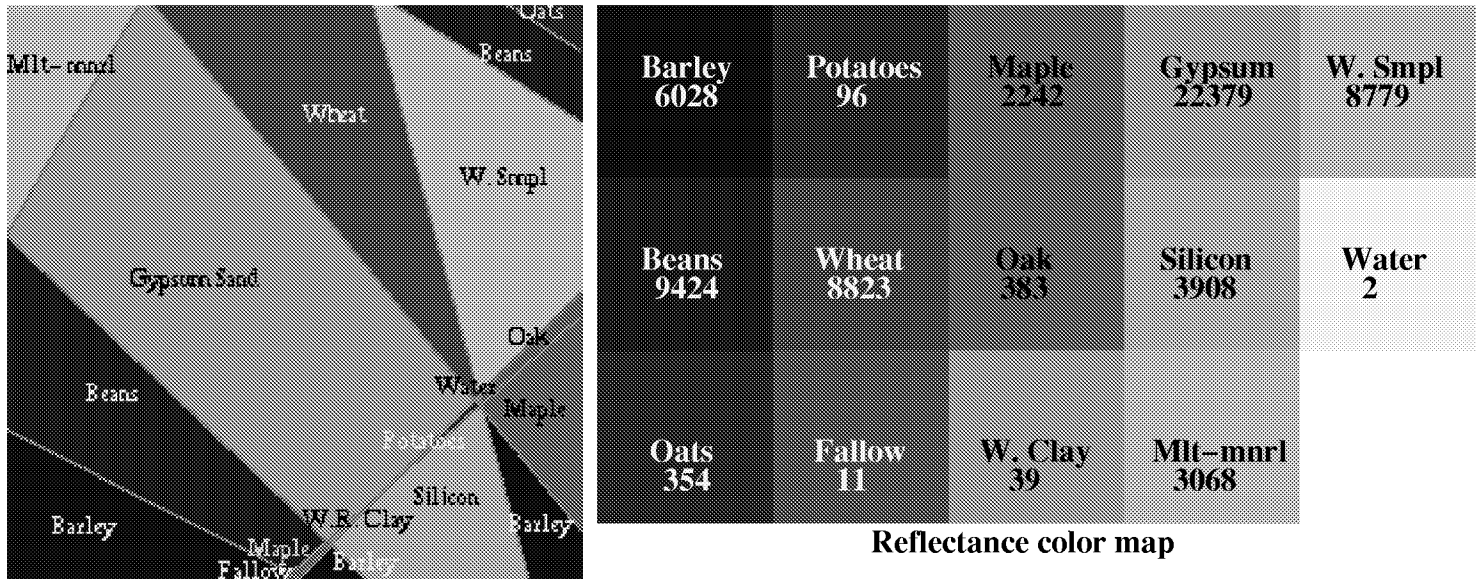


Figure 13: A random reflectance test target, where each major reflectance area is identified and marked, the corresponding “color” map, and the number of pixels of each reflectance in the target.

the bench mark to quantify the effectiveness of each recovery technique.

## 4 Atmospheric Correction Techniques

The approximated albedo  $\tilde{\rho}_a(\lambda)$  as extracted from the measured radiance  $L_m(\lambda)$  by the remote sensing system, is commonly derived from Eqs. 8, 18 and 22 as

$$\tilde{\rho}_a(\lambda) = \frac{\pi d^2}{E_s(\lambda) \cos(\theta_z) \cos(\theta_s)} L_m(\lambda), \quad (25)$$

where  $\sim$  indicates estimated terms. While the albedo  $\rho_a(\lambda)$  is a useful measure for several applications, it does not account for the perturbations imposed by the transmittance components,  $T_d(\lambda)$ ,  $T_b(\lambda)$  and  $T_p(\lambda)$  and the path radiance  $L_p(\lambda)$ . Therefore, it differs from the surface reflectance  $\rho(\lambda)$ , as illustrated in Figs. 8 and 9.

Figure 14(a) illustrates the albedo estimate of the deterministic and stochastic measured radiance signal illustrated in Fig. 11. The dotted line indicates the original reflectance at  $\lambda = 0.5\mu\text{m}$ , the solid gray line is the albedo estimate from the deterministic measured radiance (no added noise or uncertainties) after the addition of the adjacency blurring effects with a spatial scale factor of  $s = 3$ , and the solid black line indicates the albedo estimate from the stochastic measured radiance illustrated in Fig. 11(d). As expected, this figure shows that the albedo estimate is too high for low reflectances and too low for high reflectances.

### 4.1 Bowker Reflectance Recovery Technique

Bowker's atmospheric correction technique [3] uses Eqs. 9 and 10 to estimate the surface reflectance  $\rho(\lambda)$  from the radiance  $L_m(\lambda)$  measured by a remote sensing system. By subtracting the path radiance from the measured radiance (Eq. 9), and substituting Eq. 10 for the result, the estimated reflectance is given by

$$\tilde{\rho}(\lambda) = \frac{\pi}{\tilde{E}(\lambda)T_b(\lambda)} [L_m(\lambda) - \tilde{L}_p(\lambda)] \quad (26)$$

where  $T_b(\lambda)$  is the surface-to-sensor direct atmospheric transmittance. When the original reflectance is unknown,  $L_p(\lambda)$  is estimated from a constant reflectance of  $\rho(\lambda) = 0.4$ . Since  $L_p(\lambda)$  depends directly on  $\rho(\lambda)$ , the difference between  $\tilde{L}_p(\lambda)$  and  $L_p(\lambda)$  poses an accuracy problem.

Similar to Fig. 14(a), Fig. 14(b) illustrates the performance of Bowker's reflectance estimate of the deterministic and stochastic total radiance signal. This figure shows that Bowker's estimate is very accurate

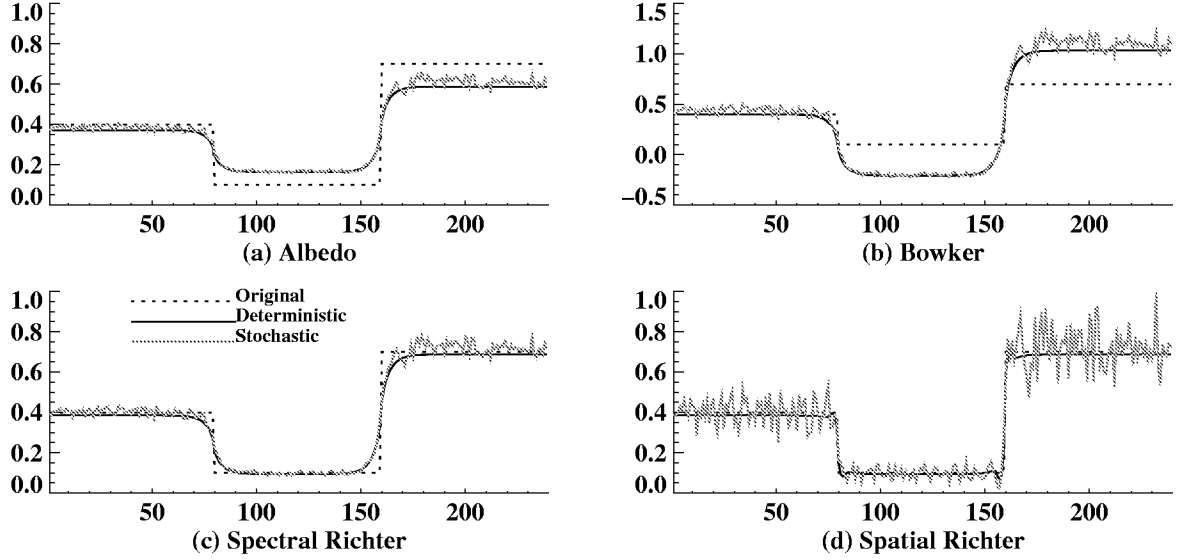


Figure 14: The correction techniques.

when  $L_p(\lambda) = \tilde{L}_p(\lambda)$ , as indicated from the recovery of the  $\rho = 0.4$  segment. However, this technique is extremely inaccurate when  $L_p(\lambda)$  differs from  $\tilde{L}_p(\lambda)$  as indicated from the recoveries of  $\rho = 0.1$  and  $0.7$  to the physically unreasonable reflectance values of  $-0.2$  and  $1.03$  respectively.

## 4.2 Richter Reflectance Recovery Technique

Richter's technique, developed for fast atmospheric correction of Landsat Thematic Mapper (TM) images, can be divided into a spectral correction that accounts for the effective irradiance  $E_T$  (Eq. 20), followed by a spatial correction that accounts for the adjacency blurring effects. The spectral reflectance correction is derived from the measured radiance, using Eqs. 19 and 22 [5, 6]

$$\begin{aligned}
 \tilde{\rho}^{(1)}(\lambda) &= \frac{\pi}{\tilde{E}(\lambda) [\tilde{T}_b(\lambda) + \tilde{T}_p(\lambda)]} [L_m(\lambda) - L_o(\lambda)] \\
 &= \frac{\pi}{\tilde{E}(\lambda) \tilde{T}_t(\lambda)} [L_m(\lambda) - L_o(\lambda)] \\
 &= \frac{\pi}{\tilde{E}_T(\lambda)} [L_m(\lambda) - L_o(\lambda)],
 \end{aligned} \tag{27}$$

where  $\tilde{E}(\lambda)$  and  $\tilde{T}_p(\lambda)$  are the estimated values of the total irradiance and diffuse atmospheric transmittance respectively, for a constant reflectance of  $\rho(\lambda) = 0.4$ , and  $L_m(\lambda)$  is the measured digital radiance given

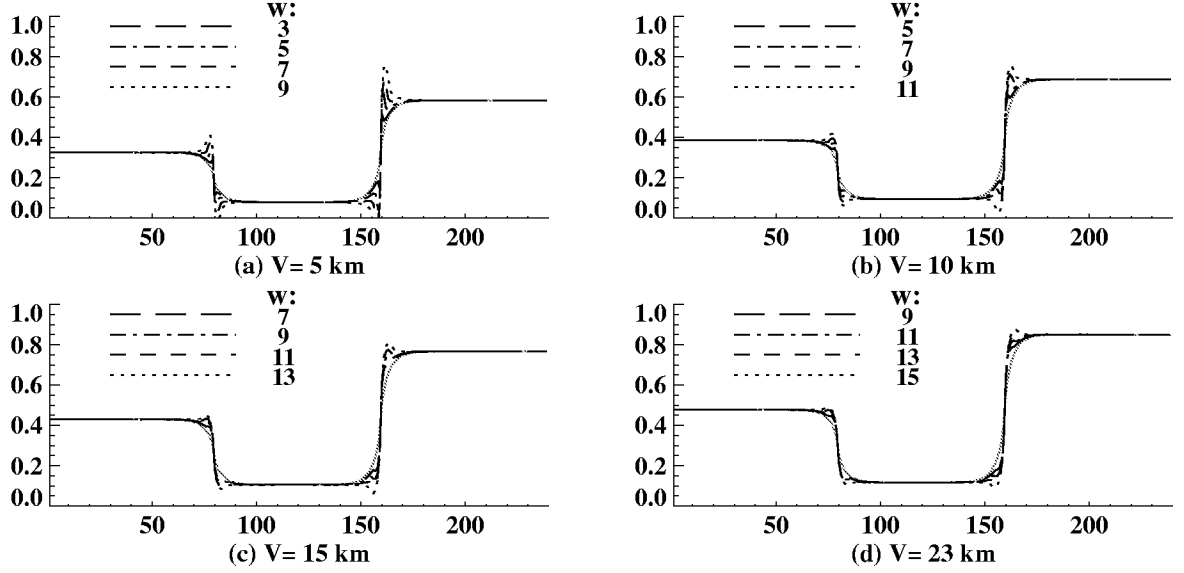


Figure 15: Richter's spatial correction.

by Eq. 22. Accurate corrections depend on an accurate knowledge of the solar zenith angle (within 5 degrees) and a relatively accurate estimation of the atmospheric conditions, including the haze type and visibility. In contrast to Bowker's technique, Richter's spectral correction subtracts  $L_o(\lambda)$ , which is a pure atmospheric noise term, instead of subtracting  $L_p(\lambda)$ , which depends on  $\rho(\lambda)$ . Therefore, this technique is self-correcting and less susceptible to inaccuracies when the underlying surface reflectance is unknown.

Figure 14(c) assesses Richter's spectral reflectance correction estimate. In contrast to Bowker's correction technique, Richter's spectral correction is very accurate throughout the whole reflectance range, and is not sensitive to the assumption of a constant reflectance of  $\rho = 0.4$ . However, it does not correct for the adjacency blurring effects, because it assumes a constant average surface reflectance value for the viewed area. Therefore, it is a very good approximation for a small uniform area of square kilometers, but does not account for the effects of radiance scattered from surrounding pixels of different reflectance signatures.

The spectral approximation is updated by the spatial correction given by

$$\tilde{\rho}^{(2)}(\lambda) = \tilde{\rho}^{(1)}(\lambda) + q \left[ \tilde{\rho}^{(1)}(\lambda) - \bar{\rho}^{(1)}(\lambda) \right], \quad (28)$$

where

$$q = \frac{\tilde{T}_p(\lambda)}{\tilde{T}_b(\lambda)},$$



is the ratio between the diffuse and path transmittance at the  $(x, y)$  spatial location, and

$$\bar{\rho}^{(1)}(x, y, \lambda; w) = \frac{1}{w^2} \sum_{i=1}^w \sum_{j=1}^w \tilde{\rho}^{(1)}(x + i - w/2, y + j - w/2, \lambda),$$

is the spatial summation (average) of  $w$ -by- $w$  neighboring spectral reflectance estimates. Neither the spectral nor the spatial corrections account for random noise. The underlying assumption of the spatial correction technique is that the center/surround numerical differentiation operation in Eq. 28,  $[\tilde{\rho}^{(1)}(\lambda) - \bar{\rho}^{(1)}(\lambda)]$ , enhances only the adjacency blurring affects. However, in the presence of noise, and away from the edge, this operation differentiates, and therefore enhances, pure random fluctuations (noise). Therefore, the spatial correction, which is designed as a deblurring operator for a noiseless signal, has the potential of boosting the noisy elements at spatial locations away from the edge.

Figure 15 evaluates the spatial recovery as a function of  $w$  for a deterministic simulation with different visibility conditions and a constant solar zenith of  $\theta_z = 30^\circ$ . The solid gray line illustrates Richter's spectral recovery for the  $\lambda = 0.5\mu\text{m}$  band, and is compared to Richter's spatial correction as a function of  $w$ , illustrated in black patterned lines. Optimal widths  $w$  for this deterministic case are 5, 9, 11, and 13 pixels for visibilities of 5, 10, 15, and 23km respectively. This figure shows that selecting a  $w$  that is too narrow does not deblur the recovered reflectance estimate near the edge. However, a  $w$  that is too wide enhances the edge by creating Mach-bands around it, similar to the non-linear Retinex filter with a wide surround [12, 13]. This phenomenon perceptually sharpens the overall spatial signal at each spectral band, at the cost of correct identification at the target's edges.

Figure 14(d) assesses the effects of Richter's spatial reflectance correction estimate with  $w = 9$ , relative to its spectral correction illustrated in Fig. 14(c). This figure shows that Richter's spatial correction deblurs the adjacency blurring effect, as demonstrated by the sharp and accurate edge transition for both the deterministic and stochastic signals. The deterministic estimate differs from the original reflectance by only 1%, and therefore exhibits a very accurate recovery. However, as predicted, this technique boosts the local random fluctuation away from the edge. To minimize the effect of random fluctuations, and enhance the measurement of the spatial blurring defects, the above difference operation can be replaced by a difference between two smoothed signals, each with a different width  $w$ . The first, a smoothing filter by a relatively small  $w$ , will minimize the local random fluctuations. The second filter, performed on the already smoothed signal, will use a wider  $w$  to capture the adjacency blurring degradations and correct for them.

### 4.3 Assessment Tools

The spectral accuracy of each recovery technique at each pixel  $(x, y)$  is defined by the root-mean-square error (*rmse*) metric, applied to the relative difference between the original and the recovered reflectances,  $\rho(x, y, \lambda)$  and  $\tilde{\rho}(x, y, \lambda)$ , over the set of permissible spectral wavelengths  $\{\lambda_i\}$ ,

$$\varepsilon(x, y; \tilde{\rho}) = \left( \overline{\left\{ \left( \frac{\rho(\lambda_i) - \tilde{\rho}(x, y, \lambda_i)}{\rho(\lambda_i)} \right)^2 \right\}_{\{\lambda_i\}}} \right)^{1/2} \quad (29)$$

respectively, where  $\overline{\{\bullet\}}_{\{\lambda_i\}}$  denotes the statistical mean over the  $\{\lambda_i\}$  set. Similarly, the global recovery accuracy for each spectral signature area  $\rho(x, y, \lambda)$  is defined by the relative *rmse* between the original  $\rho(\lambda)$  and the averaged recovered reflectances  $\bar{\rho}(\lambda)$ , across the set of pixels  $\{(x, y)_\rho\}$  that belongs to that reflectance area,

$$\varepsilon(\tilde{\rho}) = \overline{\{\varepsilon(x, y; \tilde{\rho})\}}_{\{(x, y)_\rho\}}. \quad (30)$$

Accordingly, the identification process seeks the spectral signature that is closest, in the *rmse* sense, to the recovered signature. Hence, if  $\{\rho_j(\lambda)\}$  represents the set of possible signatures, and  $\{\varepsilon_j\}$  denotes the set of *rmse*'s between  $\tilde{\rho}(\lambda)$  and each of the spectral signatures  $\rho_j(\lambda)$ , as given by

$$\varepsilon_j(x, y; \tilde{\rho}) = \left( \overline{\left\{ \left( \frac{\rho_j(\lambda_i) - \tilde{\rho}(x, y, \lambda_i)}{\rho_j(\lambda_i)} \right)^2 \right\}_{\{\lambda_i\}}} \right)^{1/2},$$

then the identification process is defined by the index  $j$  that minimizes the set  $\{\varepsilon_j\}$ . The local identification error for each pixel  $(x, y)$ ,  $\varepsilon(x, y)$ , which associates  $\rho_j$  with the recovered reflectance  $\tilde{\rho}$ , is given by

$$\varepsilon(x, y; \rho_j) = \min_j \{\varepsilon_j(x, y; \tilde{\rho})\}. \quad (31)$$

Similarly, the global identification error  $\varepsilon$  that associates  $\rho_j$  with  $\tilde{\rho}$  over the set of pixels  $\{(x, y)\}$  is given by

$$\varepsilon = \min_j \{\varepsilon_j(\tilde{\rho})\}. \quad (32)$$

The identification and classification process is also accompanied by the fraction of misidentified pixels  $F_m$ , the fraction of unidentified pixels  $F_u$ , and the assessment of the misidentified and unidentified pixels-location distribution in the set  $\{(x, y)\}$ . An unidentified pixel is defined as a pixel for which the process finds more than one index  $j$  with the same minimum  $\varepsilon(x, y; \rho_j)$ , or for which the *rmse* is above a specified threshold. On one hand, without any threshold, there will always be a minimum  $\varepsilon(x, y; \rho_j)$ , and therefore no unidentified pixels. On the other hand, a low threshold will increase  $F_u$  and decrease  $F_m$ . Therefore, there is a tradeoff between the pre-determined *rmse* threshold and the values of  $F_u$  and  $F_m$ .

## 5 Deterministic Evaluation

### 5.1 Spectral Assessment

This section assesses the recovery techniques presented in Sec. 4 for the deterministic case, i.e., when all the components in Eq. 19 are well defined, with no inaccuracies, noise, or uncertainties. Fig. 16 compares the Bowker (Eq. 26) and Richter (Eq. 27) 1-D spectral reflectance recovery techniques to the well-known apparent reflectance (albedo) approximation (Eq. 18) for constant initial reflectances of  $\rho(\lambda) = 0.1, 0.4$ , and  $0.7$ , over the set of permissible spectral bands  $\{\lambda_i\}$ , as functions of the solar zenith angle and the visibility. This purely 1-D spectral simulation complements Fig. 14 which illustrates a spatial cut-through at the spectral band of  $\lambda = 0.5\mu\text{m}$ . The recovery processes have no *a priori* knowledge of the initial reflectance, and assume a constant spectral reflectance of  $\rho(\lambda) = 0.4$ . Results show that the accuracy for all the recovery techniques increases with increased reflectance, improved visibility, and decreased optical depth (decreased solar zenith angle). Bowker’s technique performs well only for *a priori* known initial reflectances, as demonstrated by the recovery of the  $\rho(\lambda) = 0.4$  case. For unknown initial reflectance, however, this estimate deteriorates, particularly in the visible and near-IR range. By contrast, Richter’s technique performs consistently better for the whole range of reflectances, visibility conditions, and solar zenith angles, a robustness that is also affirmed by simulation results summarized in Appendix A.1, Tables A.1–A.3.

### 5.2 Spatio-Spectral Assessment

Figure 17 illustrates the recovered hyper-spectral cube illustrated in Fig. 12 and 13(a), after the identification process from the albedo, Bowker, and Richter approximations, respectively. The simulation parameters range from high visibility of 23km to low visibility of 5km, and from solar zenith angle of  $0^\circ$  to  $45^\circ$ . Adjacency blurring is simulated with a spatial spread scale factor of  $s = 3$ . The recovery techniques assume a constant spectral reflectance of  $\rho(\lambda) = 0.4$ . For each pixel, the recovered spectral signature is identified by the process described in Section 4.3, in which each recovered signature is compared to the bank of reflectance signatures listed in Table 2. The closest signature in the minimum *rmse* sense is classified as the pixel’s reflectance, and is assigned the gray level associated with that reflectance, while unidentified pixels are marked in white. The identification threshold for the *rmse* in these simulations was set to 1.5. The global *rmse* is marked on each recovered image. Tables A.4–A.6 in Appendix A.1 summarize the identification process for each reflectance selected for Fig. 13.

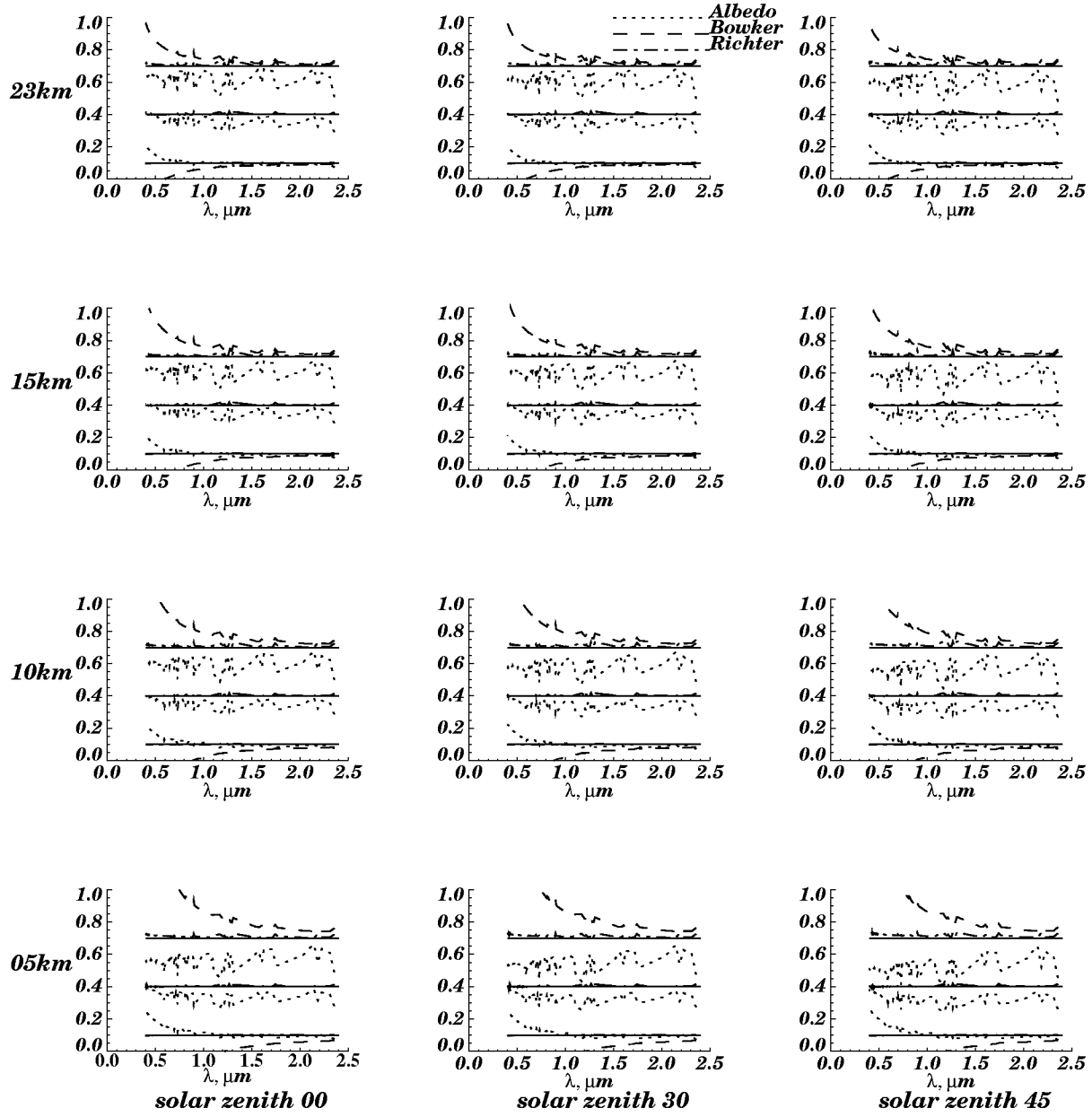


Figure 16: 1-D recovery of the 0.1, 0.4, and 0.7 reflectances, using the apparent reflectance (albedo), Bowker and Richter techniques.

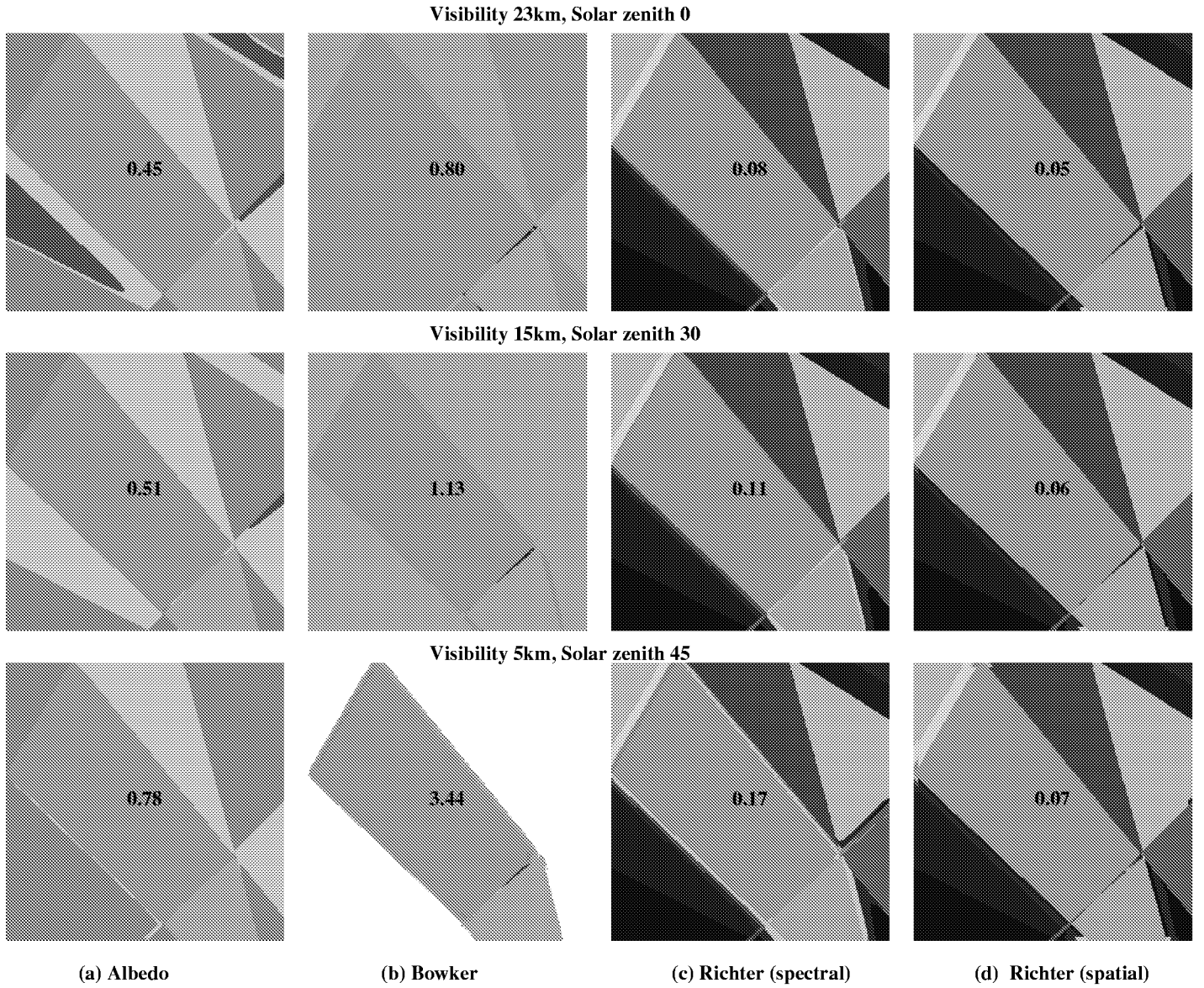


Figure 17: Recovery of the polygon test target using the (a) apparent reflectance (albedo) (b) Bowker, (c) Richter and (d) spatial correction to Richter with  $w = 9$ . The global  $rmse$  is marked on each image.

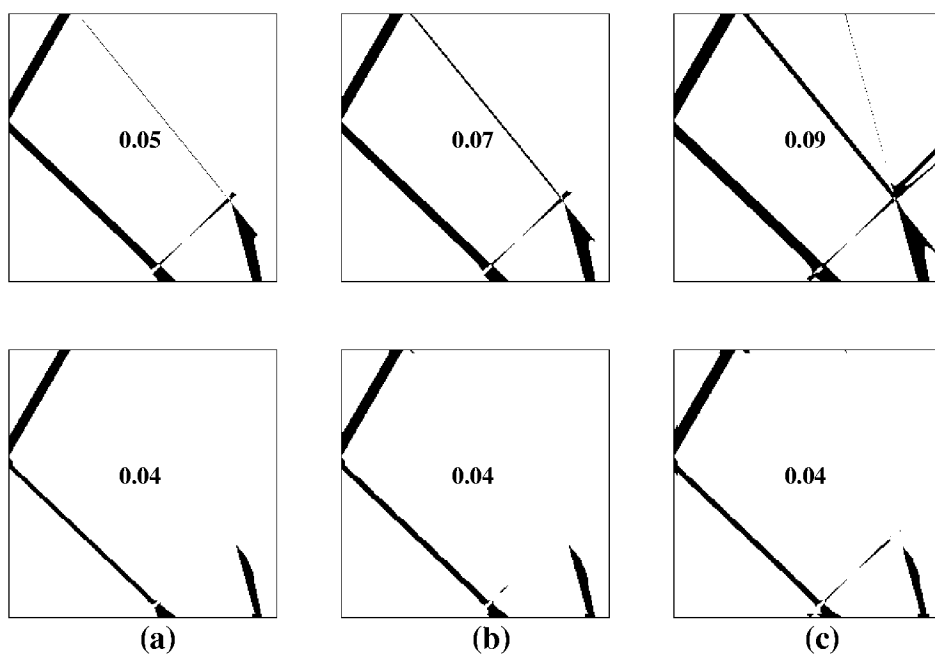


Figure 18: Location of the misidentified pixels after Richter's spectral (top) and spatial (bottom) recoveries for visibilities of (a)  $V = 23\text{km}$ , (b)  $V = 15\text{km}$ , and (c)  $V = 5\text{km}$ . The global fraction of mismatched pixels is marked on each image.

Assessment of the spatio-spectral deterministic simulation by Tables A.4–A.6 and by Fig. 17 shows that the classification process that follows the apparent reflectance approximation correctly identifies only two reflectances and misidentifies twelve, independent of the acquisition conditions. The identified signatures, gypsum sand and silicon sand, cover 40% of the target. Classification from Bowker reflectance estimates correctly adds potatoes and wet red clay to the identification process for visibilities of 23km and 15km, despite their relatively small area in the target (a total of 96 and 39 pixels respectively). However, for the low visibility of 5km, Bowker’s technique correctly identifies only two signatures, misidentifies nine, and can not identify the reflectances of fallow field, oats, and Whitley County soil. The spectral Richter recovery technique correctly identifies eleven reflectance signatures, independent of the acquisition conditions, and misidentifies potatoes (96 pixels), wet red clay (39 pixels), and water (2 pixels). By contrast to both the Bowker and the albedo approximations, misidentification in Richter’s spectral recovery technique is centered along the target’s edges, as illustrated in the top row of Fig. 18, which depicts the location of misidentified pixels for the spectral (top) and spatial (bottom) Richter recoveries. As demonstrated by both the decreasing *rmse* of the recovery illustrated in Fig. 17, and the decreasing misidentification fraction whose location is depicted in Fig. 18, the spatial correction by Eq. 28 with  $w = 9$  minimizes the adjacency effects in the identification process, enables a correct identification of all the reflectances, and reduces the total fraction of misidentified pixels by a factor of two, as illustrated in the bottom row of Fig. 18. Figs. 17 and 18 also show that the misidentification error for Richter’s recovery technique increases with decreased visibility.

Consequently, these results show that Richter’s recovery technique is robust to different acquisition conditions and performs well for a variety of reflectances, without a prior knowledge of their reflectance signature. By contrast, the apparent reflectance and Bowker estimates are sensitive to both the acquisition conditions and the lack of knowledge of the original reflectance. Inaccuracies in Richter’s recovery technique stem from the adjacency effects, while inaccuracies in Bowker’s technique stem from inaccuracies in the estimate of the path radiance component  $L_p$ . These results suggest that the performance of both the albedo approximation and Bowker’s recovery technique may worsen for the stochastic case, where random noise, uncertainties, and perturbations are added to the simulation of the measured radiance.

## 6 Stochastic Evaluation of the Bowker Technique

The main shortcoming of the Bowker recovery technique lies in the necessity of obtaining a good estimate of the path radiance response  $\tilde{L}_p(\lambda)$ , a term that is dependent on the actual reflectance. This section as-

sesses the sensitivity of Bowker’s recovery technique to perturbations and uncertainties when the original reflectance is known a priori. Correct identification and robustness of this technique under these conditions will make it suitable for the detection of irregularities in areas of known reflectance signatures, and monitoring homogeneous areas by locating invading substances. It will not, however, enable the identification of the invading substances, as it will only verify their existence and monitor their location within each monitored area.

## 6.1 End-to-End Stochastic Simulation

The performance of Bowker’s technique for known reflectances is simulated for the set of acquisition conditions identified in this report, namely, solar zenith angles of  $\theta_z = 0^\circ$ ,  $30^\circ$ , and  $45^\circ$ , for visibility conditions of  $V = 5\text{km}$ ,  $10\text{km}$ ,  $15\text{km}$ , and  $23\text{km}$ . Adjacency blurring effects are simulated with 10% perturbation of the path radiance  $L_p$ , and a spatial spread factor of  $s = 3$ . Additional stochastic perturbation includes 10% uncertainty in the reflectance signature, global irradiance perturbations of 10%, and random sensor noise  $n_{\Phi_i}$  of 5% around the received radiance signal.

Tables A.7–A.9 in Appendix A.2 summarize the performance of this simulation as functions of the visibility and the solar zenith angle, for the ten reflectance areas that are larger than 100 pixels in the target illustrated in Fig 12. Figs. 19 and 20 illustrate the results of the identification process after Bowker’s recovery process and the spatial location of the misidentified reflectances, respectively. Similar to Fig. 18, misidentified pixels are marked black in Fig. 20. The global *rmse* is marked on each recovered image in Fig. 19, while the global fraction of mismatched pixels is marked on each illustration in Fig. 20. None of the four reflectances with areas smaller than 100 pixels were correctly identified. All the remaining ten reflectances were correctly identified for visibility of 23km, five of which had no mismatched pixels throughout their respective reflectance areas. Similarly, all the remaining ten reflectances were correctly identified for visibility of 15km, with only a mild increase in the fraction of misidentified pixels in the remaining five reflectances. This performance deteriorates as the visibility decreases, as is evident by the increase in the fraction of mismatched pixels. Only three signatures were completely identified with no error for  $V = 10\text{km}$ , and only two for  $V = 5\text{km}$ , where four out of the ten reflectance signatures are completely misidentified, and the fraction of misidentified pixels increases. The concentration of misidentified pixels at the border between reflectance areas, as illustrated in Fig. 20, shows that the Bowker recovery technique is sensitive to adjacency effects. In addition, these figures show that for very low visibility, this technique is also very sensitive to perturbations and random noise. This sensitivity increases with the increase of the irradiance path components – a result of larger solar zenith angles. However, the identification process for



Visibility:

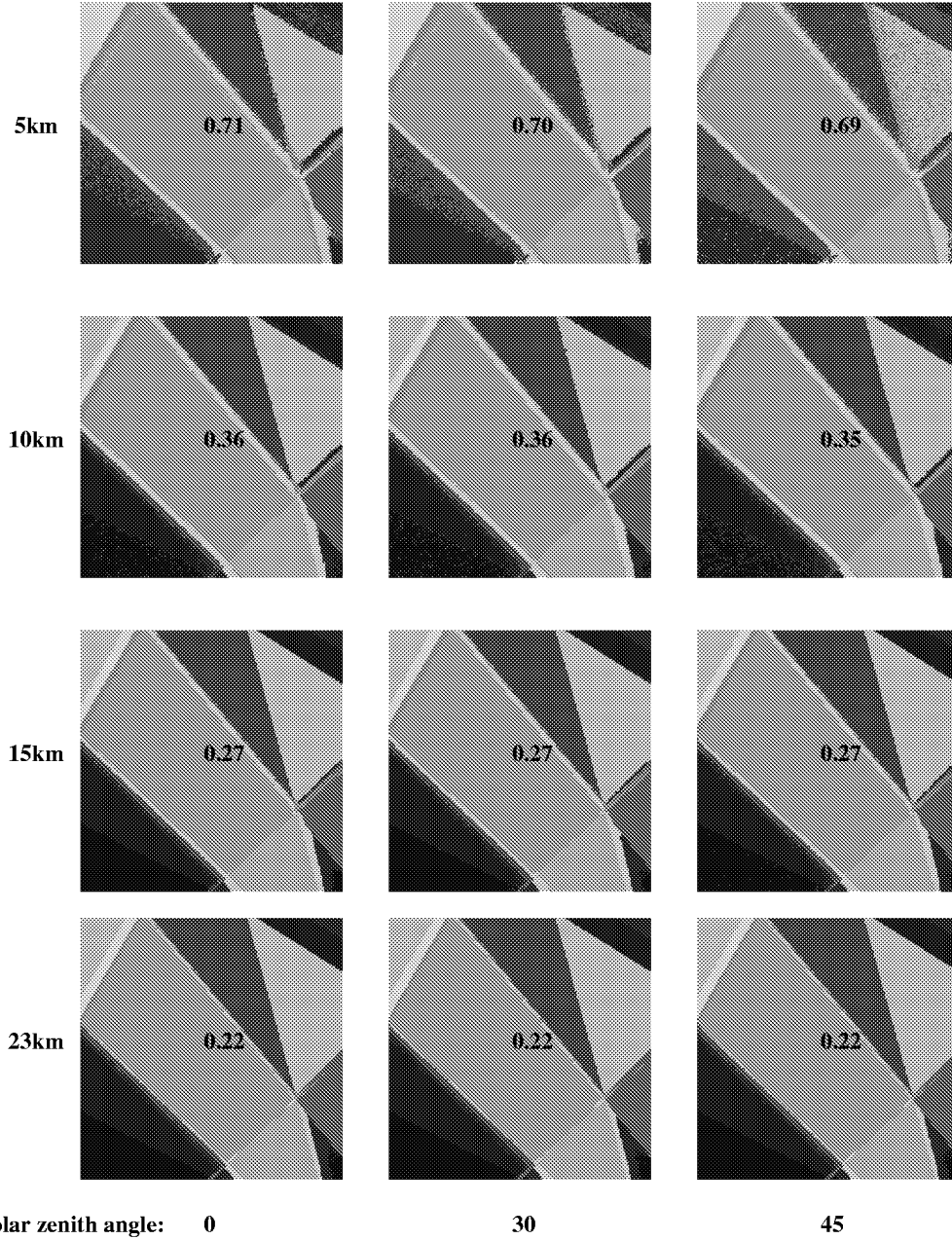


Figure 19: Reflectance recovery of the polygon test target using Bowker's technique with *a priori* known reflectances. The global *rmse* is marked on each image.

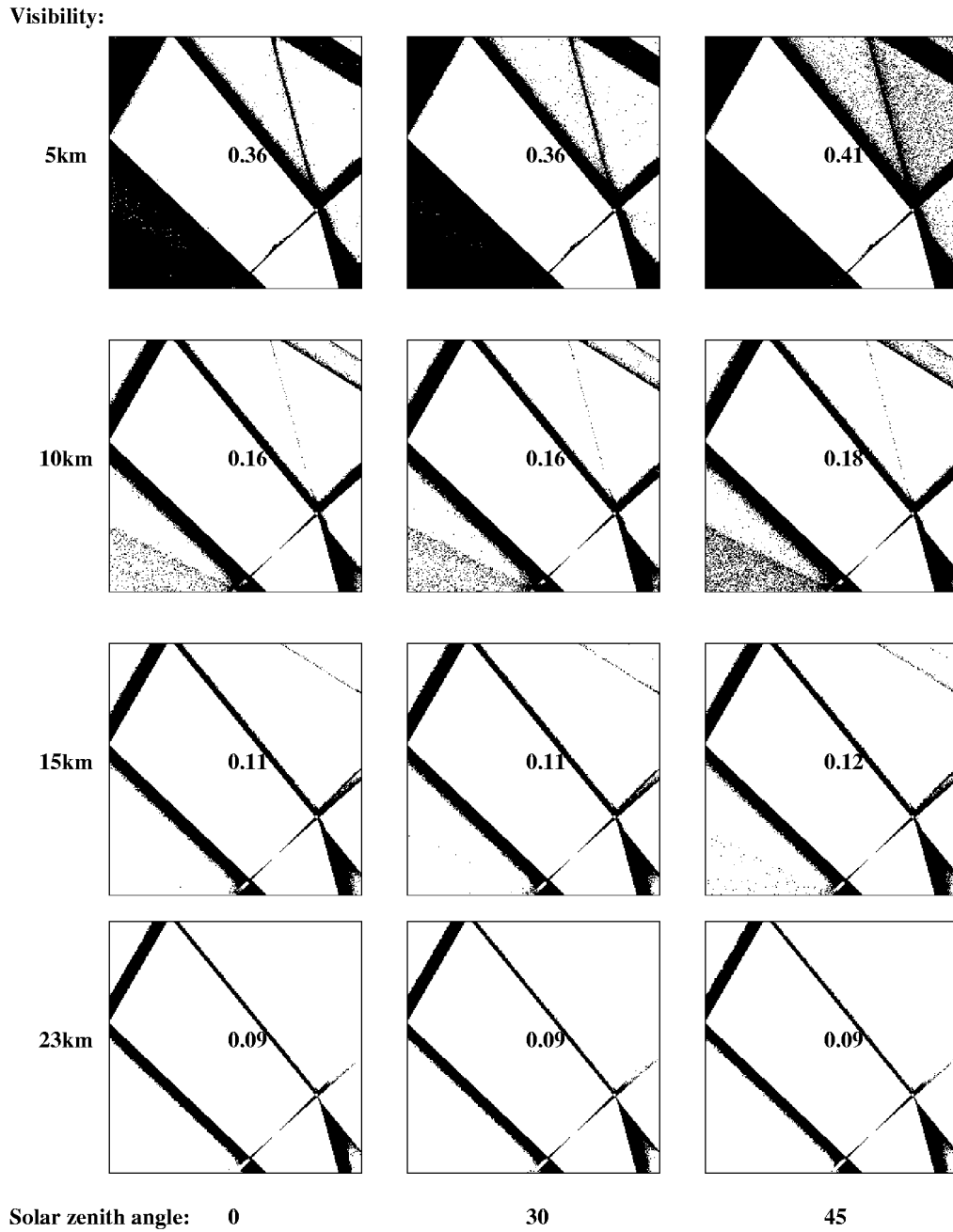


Figure 20: Spatial location of misidentified reflectance signatures in Fig. 19. The global fraction of mismatched pixels is marked on each image.

the stochastic process works well as the visibility improves.

## 7 Stochastic Evaluation of the Richter Technique

This section assesses the sensitivity and robustness of Richter’s recovery technique to perturbations in the measured radiance. Section 7.1 assesses the end-to-end stochastic performance of Richter’s recovery technique. Section 7.2 assesses the sensitivity of Richter’s recovery technique to sensor noise. Section 7.3 assesses the sensitivity of Richter’s recovery technique to small perturbations of the reflectance signature. Section 7.4 assesses the sensitivity of Richter’s recovery technique to small perturbations of the irradiance. Finally, Section 7.5 assesses the robustness of Richter’s recovery technique to wrong acquisition assumptions.

### 7.1 End-to-End Stochastic Simulation

This section assesses the general performance of Richter’s reflectance recovery from a hyper-spectral measured radiance cube simulated by the stochastic process given by Eq. 22. The simulation for this section assumes acquisition with solar zenith angles of  $\theta_z = 0^\circ$ ,  $30^\circ$ , and  $45^\circ$ , and visibility conditions of  $V = 5\text{km}$ ,  $10\text{km}$ ,  $15\text{km}$ , and  $23\text{km}$ . Spatial background scattering is simulated with 10% perturbation of the path radiance  $L_p$ , and a spatial spread factor of  $s = 3$ . Additional stochastic perturbation includes 10% uncertainty in the reflectance signature, irradiance perturbations of 10%, and random sensor noise  $n_{\Phi_i}$  of 5% around the received radiance signal.

Figure 21 illustrates results of the identification process for the simulated measured radiance after Richter’s recovery technique. The widths  $w$  used for this recovery match the optimal widths determined in Section 4.2 for the deterministic case, namely, widths of 5, 9, 11, and 13 pixels for visibilities of 5, 10, 15, and 23km respectively. The recovery global *rmse* is marked on each illustrated recovery. Fig. 22 illustrates the location of the respective mismatched pixels, where the global fraction of mismatched pixels is marked on each image. Quantitative performance assessment for  $\theta_z = 30^\circ$  and for all the major identified reflectance signatures for each reflectance area, as a function of their relative fraction, is summarized in Appendix A.3, Table A.10. Results show that for the high-visibility conditions of  $V = 15\text{km}$ , and  $23\text{km}$ , the identification process identifies all 14 reflectances of the target illustrated in Fig. 12, including the two pixels of water. Moreover, a comparison between this stochastic simulation and the deterministic case illustrated in Figs. 17 and 18 shows improvement near the edges for the stochastic recovery, probably due

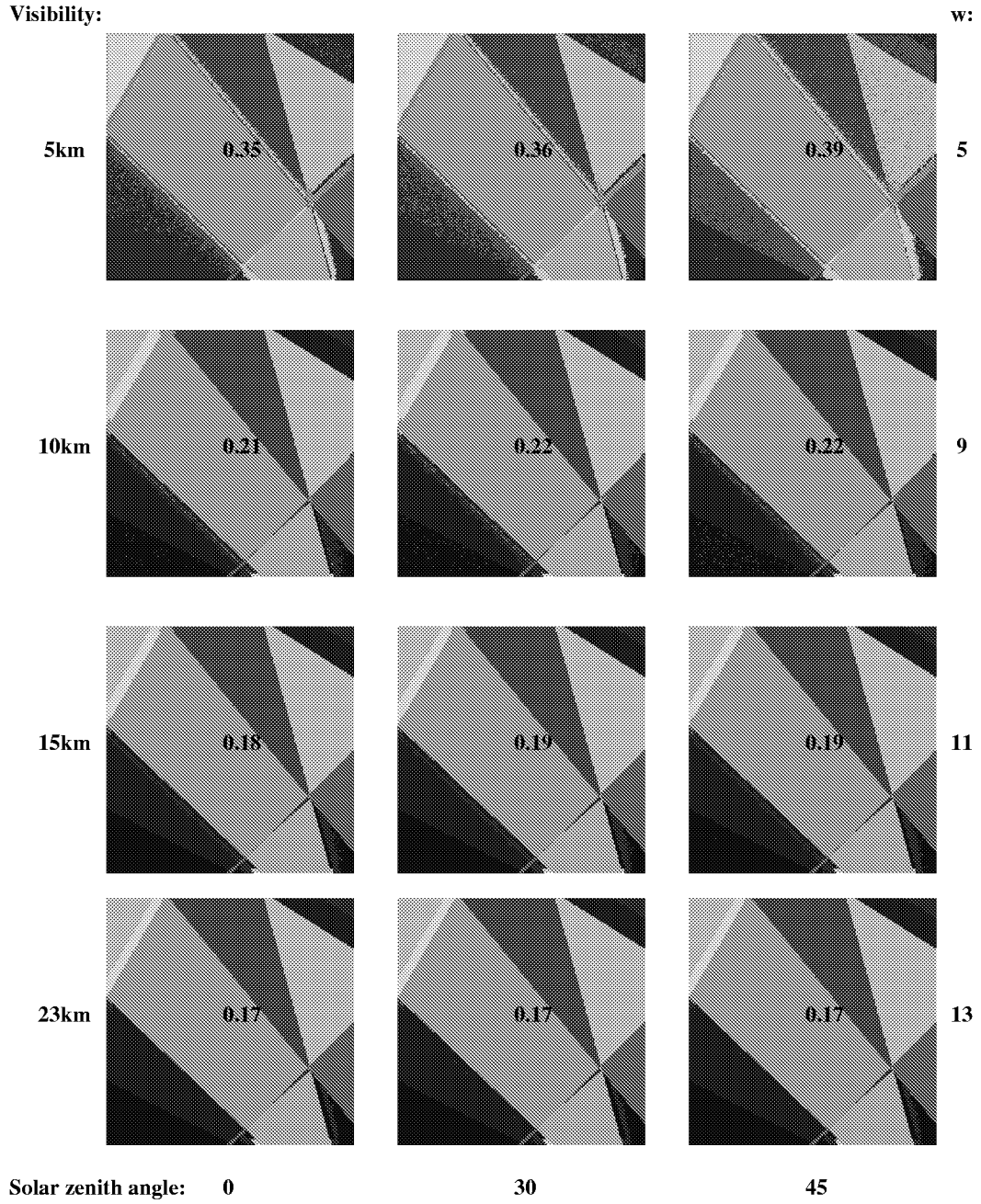


Figure 21: Reflectance recovery of the polygon test target using the spatio-spectral Richter. The global *rmse* is marked on each image.

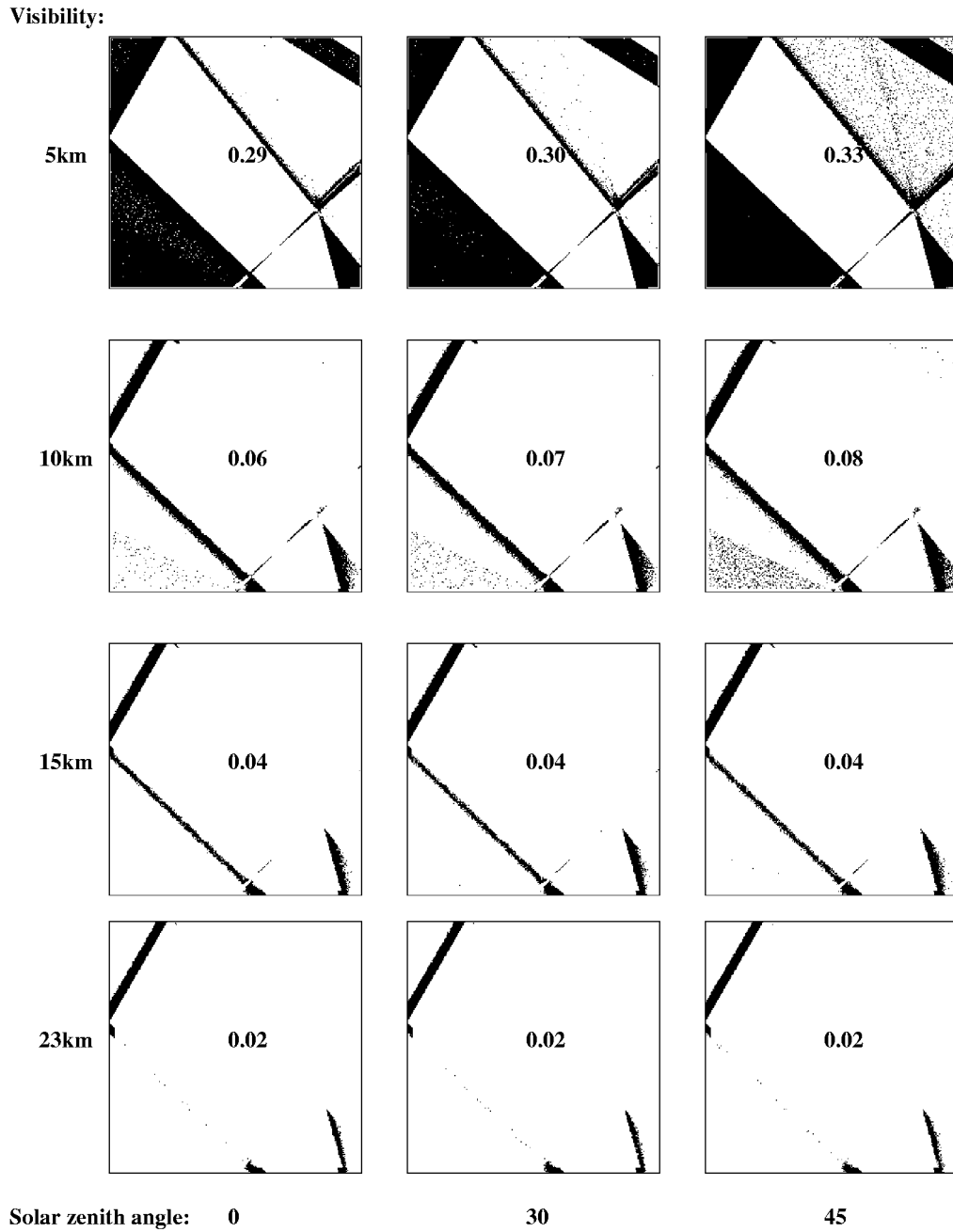


Figure 22: Spatial location of misidentified reflectance signatures in Fig. 21. The global fraction of mis-matched pixels is marked on each image.

to a wider  $w$  parameter. Inaccuracies, which constitute only 2-4% of the target, are centered around a few edges, where the spatial correction fails to completely correct for the adjacency blurring effect. This performance deteriorates with decreased visibility and increased path length (higher solar zenith angle), when noise sources combined with low visibility decrease the ability of Richter’s technique to accurately identify the correct reflectance. Moreover, recovered images for  $V = 10\text{km}$  and  $5\text{km}$  show Mach-bands around most of the target’s transitions.

## 7.2 Sensitivity to Sensor Noise

This section assesses the sensitivity of Richter’s spectral and spatial recovery techniques to sensor noise. The simulation assumes acquisition with a solar zenith angle of  $30^\circ$ , and visibility conditions of  $V = 5\text{km}$ ,  $10\text{km}$ ,  $15\text{km}$ , and  $23\text{km}$ . The adjacency effects are simulated by 10% perturbation of the path radiance  $L_p$ , and a spatial spread factor of  $s = 3$ . To simulate sensor noise levels of 5% and 10%, the stochastic process perturbs the deterministic hyper-spectral radiance cube  $L_T(x, y, \lambda_i)$  at each  $(x, y)$  location with a random additive noise of uniform distribution in the range  $[-n\%, n\%]L_T(x, y, \lambda_i)$ , where  $n = 5$ , and  $10$ , respectively. The case with no sensor noise serves as a performance benchmark.

Figures 23 and 24 assess the sensitivity of Richter’s spectral recovery by Eq. 27 to sensor noise  $n_{\Phi_i}$  as a function of the visibility for the above simulation parameters. Figs. 25 and 26 assess the corresponding performance of the spatial correction by Eq. 28. Consistent with Fig. 21, the width  $w$  used for the spatial correction as a function of the visibility is 5, 9, 11, and 13 pixels for visibilities of 5, 10, 15, and 23km respectively. The first column in each figure, illustrating the performance without sensor noise, serves as a benchmark for the stochastic optimal performance in presence of adjacency effects. Fig. 26 shows an average improvement by a factor of two in the fraction of misidentified pixels relative to the fractions in Fig. 24. Fig. 25 also shows the creation of Mach bands for the 5km visibility compared to Fig. 23. Consistent with Fig. 14(d), however, spatial correction in presence of random sensor noise boosts the noise elements by differentiating noise elements instead of reflectance transitions, thereby impeding the identification process. Therefore, the spatial correction improves the identification process near the edges at the cost of increased misidentified pixels within each reflectance area. Moreover, the spatial recovery technique completely fails for very low visibility, where the fraction of misidentified pixels reaches 57%. However, for reasonable visibility conditions above 10km, and reasonable sensors with noise levels that do not exceed 5% of the received signal, Richter’s spatial technique improves the performance of Richter’s spectral recovery.

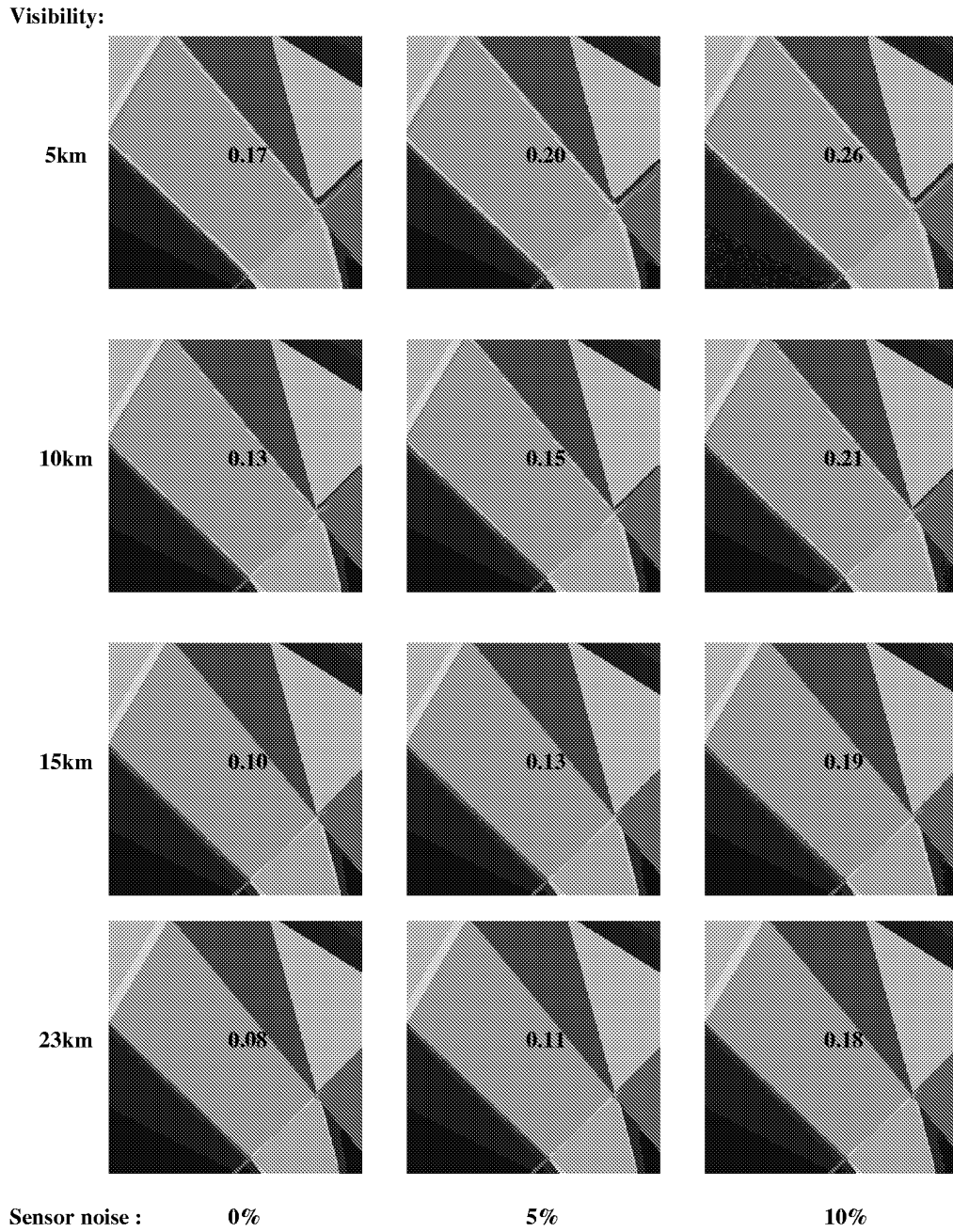


Figure 23: Richter's spectral reflectance recovery as a function of a sensor random noise. The global *rmse* is marked on each recovered image.

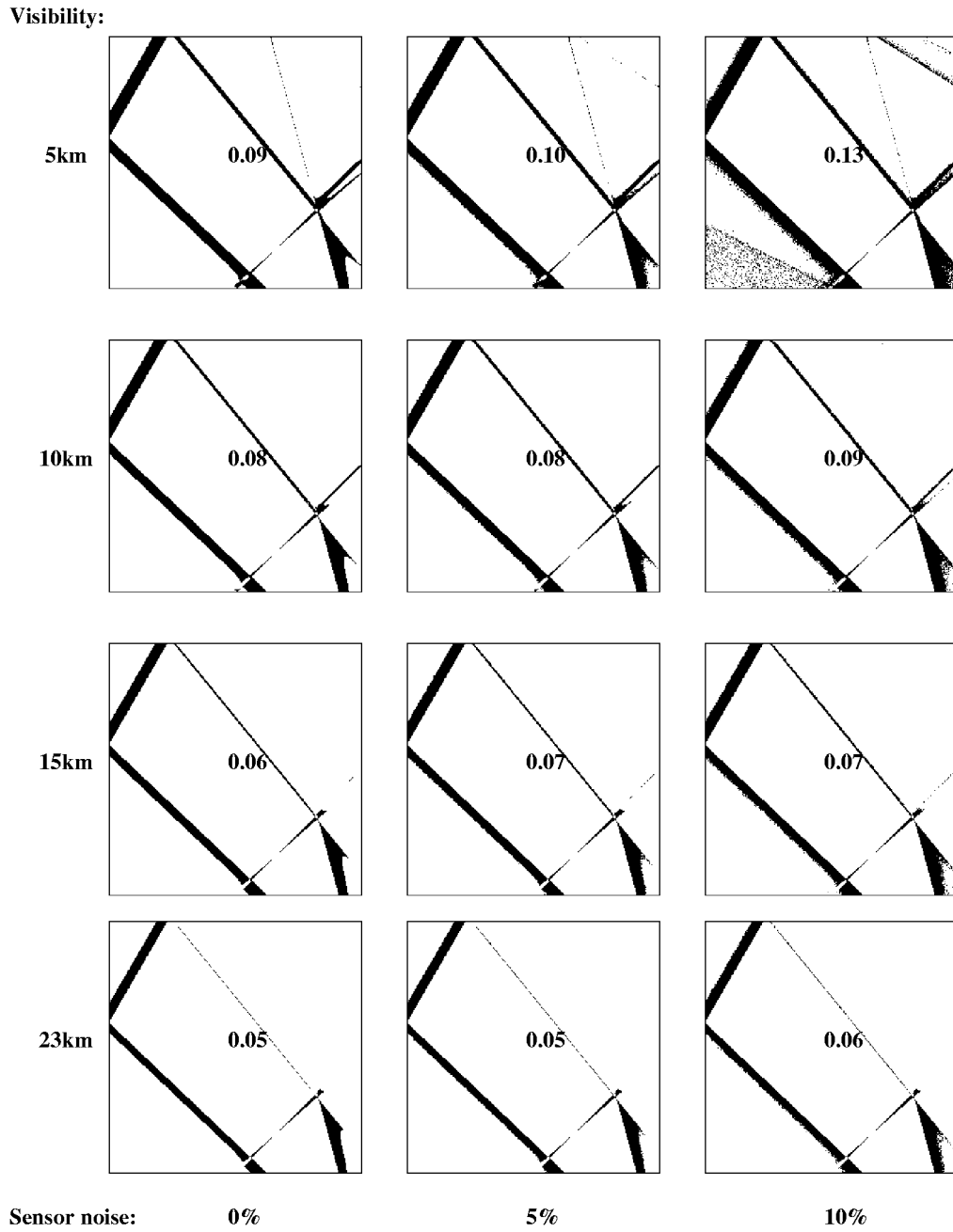


Figure 24: Location of misidentified reflectance signatures in Fig. 23. The global fraction of mismatched pixels is marked on each recovered image.



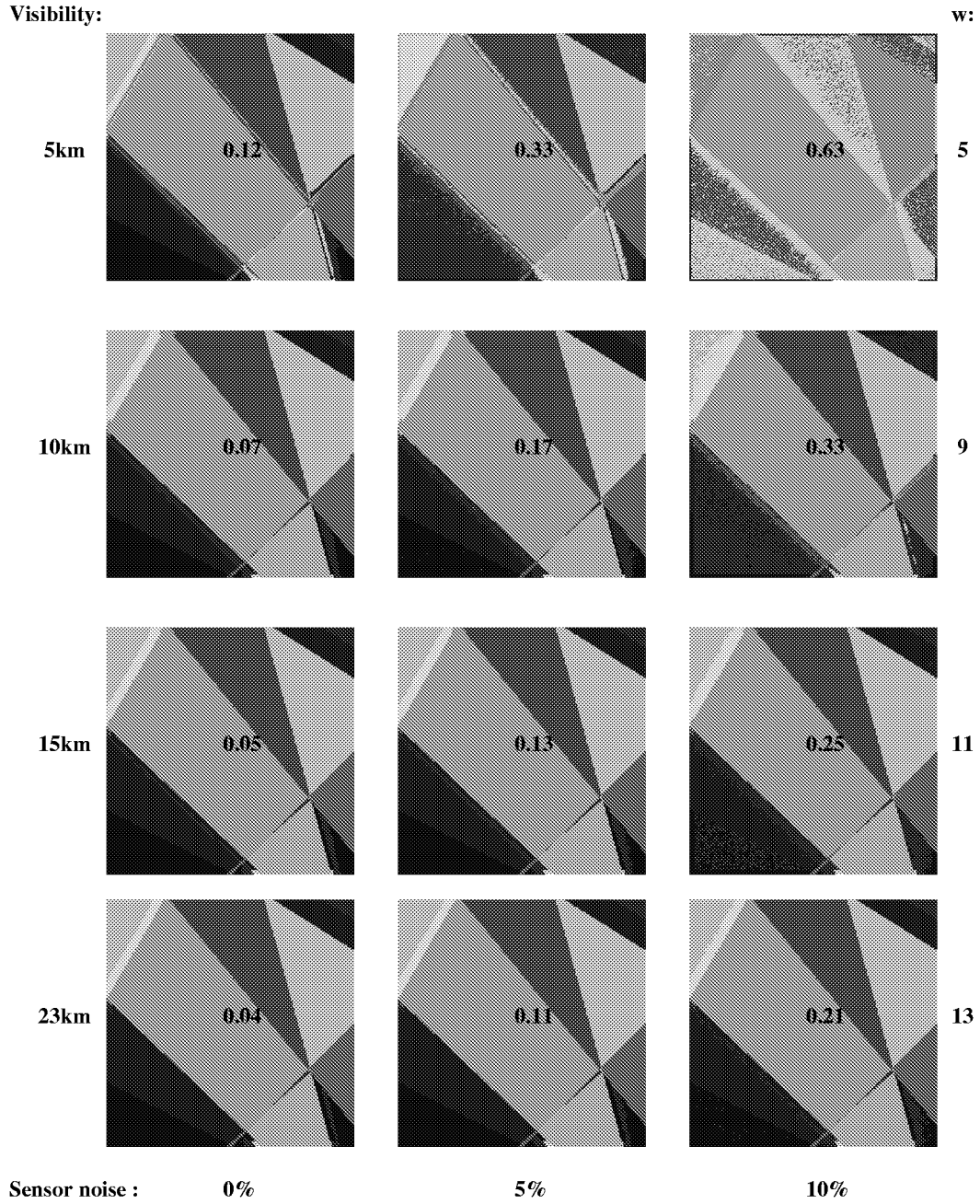


Figure 25: Richter's spatial reflectance recovery as a function of sensor random noise. The global *rmse* is marked on each recovered image.

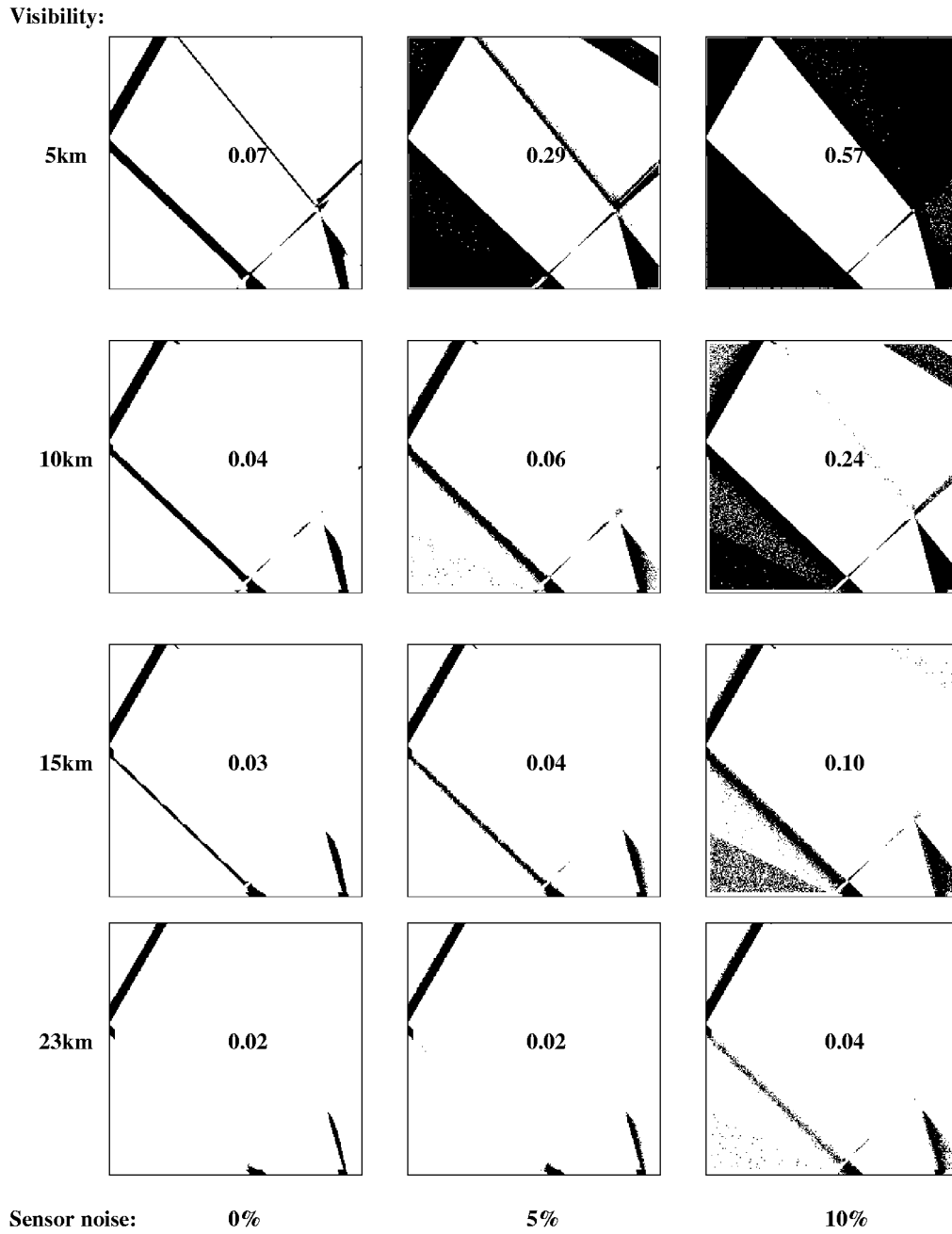


Figure 26: Location of misidentified reflectance signatures in Fig. 25. The global fraction of mismatched pixels is marked on each recovered image.

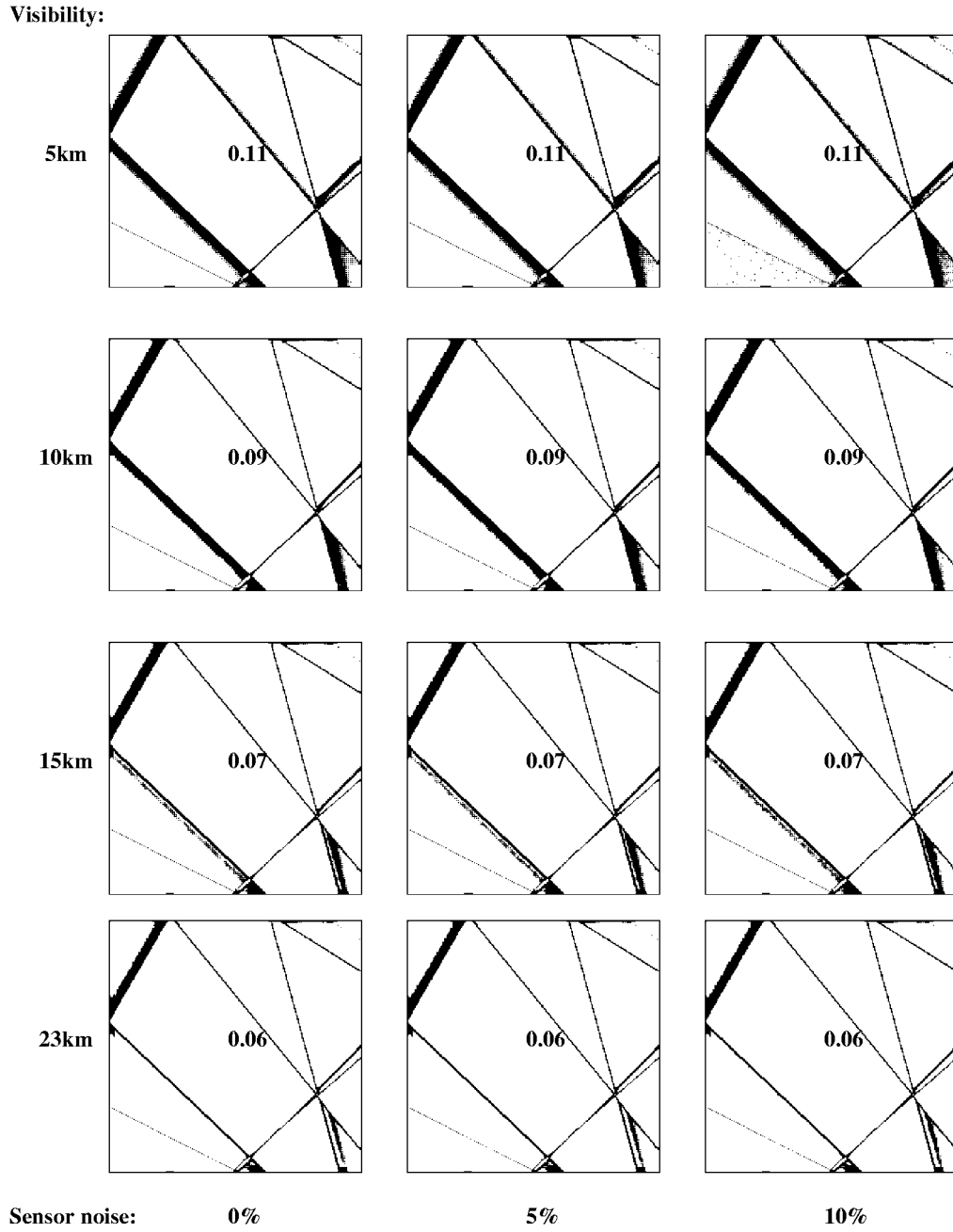


Figure 27: Location of misidentified reflectance signatures after applying Richter's spatial correction in a simulation that includes an optical blur of a camera. The global fraction of mismatched pixels is marked on each image.

Figure 27 assesses the effects of the camera’s optical blur on the performance of Richter’s spatial recovery. The simulation adds a camera with an optical-index of  $\sigma_g(\lambda_i) = 0.6$  and an electronic noise with a signal-to-noise ratio (SNR) of 64 across the spectral bands. This relatively high SNR ensures that the sensor noise remains the main noise source for this simulation. A comparison of this figure to Figs. 24 and 26 shows that optical blur stabilizes the performance of the spatial Richter correction by attenuating the sensor noise, thereby enabling Richter’s spatial correction to improve the identification near the reflectance transitions without increasing the misidentified pixels within each reflectance area. Significant improvement is observed, especially for low visibility, where the fraction of misidentified pixels decreased from 29% and 57% to 11% for sensor noise levels of 5% and 10% around the received radiance signal, respectively.

### 7.3 Perturbation of the Initial Reflectance Signature

This section evaluates the sensitivity of the Richter technique to uncertainties in the database of reflectance signatures, as well as natural non-uniformities, when measuring a single reflectance area under the same atmospheric conditions. The uncertainty in the reflectance signature database is typically about 10% around the signature’s mean [4]. To simulate 5%, 10%, and 15% uncertainties, the stochastic process perturbs the deterministic hyper-spectral reflectance cube  $\rho(x, y, \lambda)$ , illustrated in Fig. 12, at each  $(x, y)$  location with a random additive noise of uniform distribution in the range  $[-n\%, n\%]\rho(x, y, \lambda)$ , where  $n = 5, 10$ , and  $15$ , respectively. The simulation then uses the perturbed cube to recalculate  $L_s(x, y, \lambda)$  (Eq. 8) and substitutes the result in Eqs. 10 and 11 to recalculate  $L_T(x, y, \lambda)$  (Eq. 19). Other simulation components, such as the irradiance and transmittance components, remain the unperturbed deterministic components, as extracted from the MODTRAN simulations for the deterministic case. While not completely accurate, this simulation is a practical approximation to a complete MODTRAN simulation of each perturbed pixel under each atmospheric condition.

Figs. 28 and 29 compare the sensitivity of Richter’s spatial recovery techniques to uncertainties in the initial reflectance signatures, with and without the simulation of a camera, by depicting the spatial location of misidentified reflectance signatures. The adjacency effects are simulated with 10% perturbation of the path radiance  $L_p$ , and a spatial spread factor of  $s = 3$ , and the sensor noise level is set to 2% around the measured radiance. Camera parameters are  $\sigma_g(\lambda_i) = 0.6$  and electronic SNR of 64 across the spectral bands. The low level of electronic and sensor noise sources ensure that the dominant source of error remains the perturbations in the initial reflectance signature. Results show that the Richter recovery technique is robust to uncertainties in the initial reflectance signature. The fraction of unidentified pixels for 5% perturbation in Figs. 28 and 29 is similar to the fraction of unidentified pixels for the stochastic case

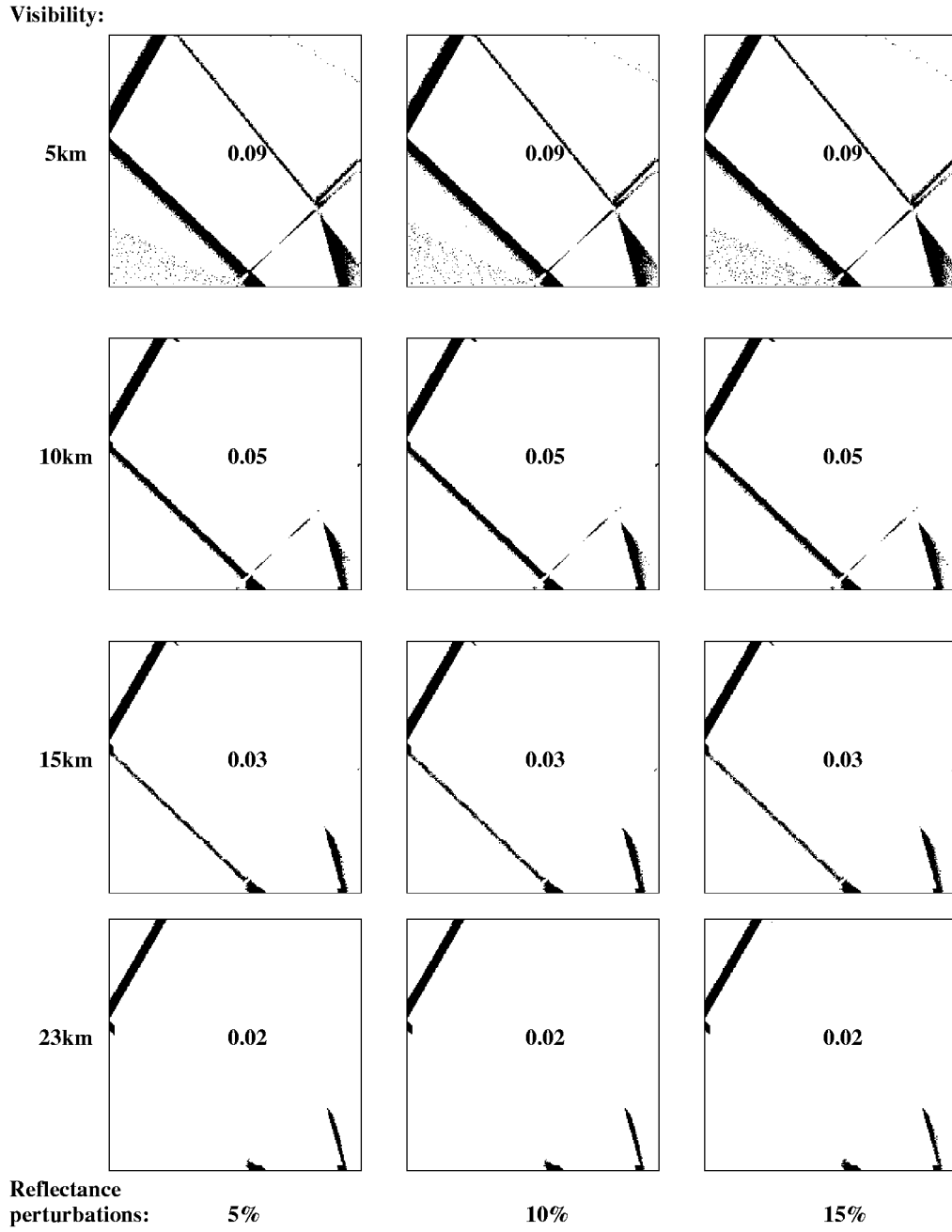


Figure 28: Location of misidentified reflectance signatures after Richter's spatial reflectance recovery for initial reflectance perturbations of 5%, 10% and 15%, for  $\theta_z = 30^\circ$ . The global fraction of mismatched pixels is marked on each image.

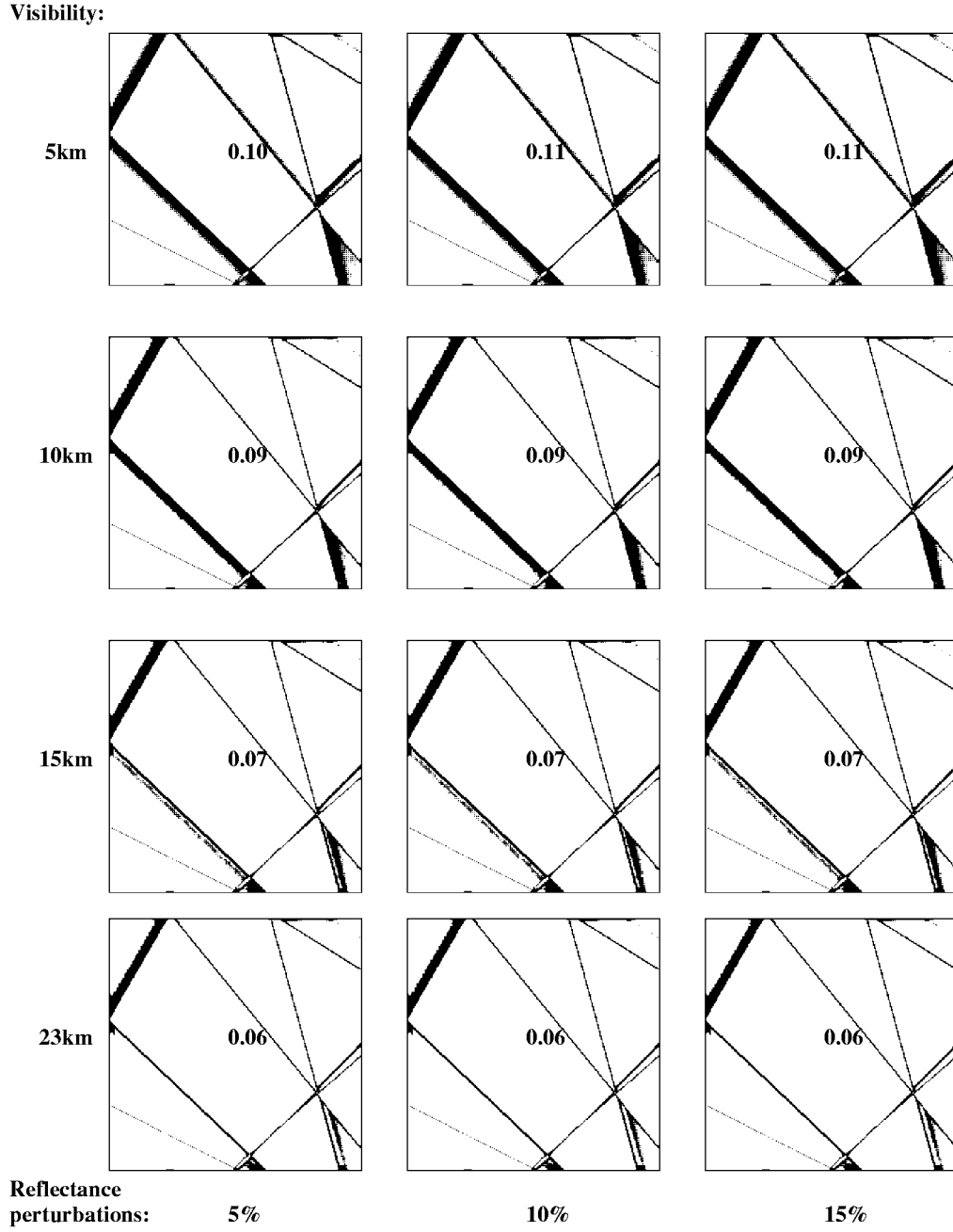


Figure 29: Location of misidentified reflectance signatures after Richter's spatial reflectance recovery for initial reflectance perturbations of (a) 5%, (b) 10% and (c) 15%, for  $\theta_z = 30^\circ$ ,  $\sigma_g(\lambda_i) = 0.6$  and electronic SNR of 64 across the spectral bands. The global fraction of mismatched pixels is marked on each image.

with no sensor noise, illustrated in Figs. 26 and 27 respectively. The addition of optics to the simulations illustrated in Fig. 29 reduces the fraction of misidentified pixels within each reflectance area, where optical blur is the dominant camera degradation, and increases the fraction of these pixels near the reflectance transitions, where optical aliasing is the dominant camera degradation. Nevertheless, both simulations demonstrate that this technique is relatively robust to uncertainties up to 15% in the initial reflectance signature for a wide range of visibility conditions.

## 7.4 Perturbations in the Atmospheric Conditions

This section evaluates the sensitivity of Richter’s recovery technique to perturbations in the irradiance  $E(\lambda)$ , which simulate inaccuracies and local perturbations in the assumed atmospheric conditions, such as visibility, and aerosol types and densities. These perturbations do not simulate shadowing effects. To simulate 5%, 10%, and 15% inaccuracies, a stochastic process perturbs the deterministic hyper-spectral total irradiance  $E(x, y, \lambda)$  at each  $(x, y)$  location with a random additive noise of uniform distribution in the range  $[-n\%, n\%]E(x, y, \lambda)$ , where  $n = 5, 10$ , and  $15$ , respectively. The simulation then uses the perturbed cube to recalculate  $L_s(x, y, \lambda)$  (Eq. 8) and substitutes the result in Eqs. 10 and 11 to recalculate  $L_T(x, y, \lambda)$  (Eq. 19).

Figures 30 and 31 assess the sensitivity of the identification process to uncertainties in the irradiance at acquisition time, with and without the simulation of a camera, by depicting the spatial location of misidentified reflectance signatures. The adjacency effects are simulated with 10% perturbation of the path radiance  $L_p$ , and a spatial spread factor of  $s = 3$ , the sensor noise level is set to 2% around the measured radiance, and reflectance perturbations are set to 5% around the initial reflectance signature. Camera parameters are  $\sigma_g(\lambda_i) = 0.6$  and electronic SNR of 64 across the spectral bands. The low level electronic and sensor noise sources and low reflectance perturbation level ensure that the dominant source of error is due to perturbations in the total irradiance. Results show that the Richter recovery technique is robust to uncertainties in the atmospheric acquisition conditions, as the fraction of unidentified pixels remains almost unchanged as the perturbation level increases from 5% to 15%. This fraction is also similar to the fraction of unidentified pixels for the stochastic case with no sensor noise illustrated in Figs. 26 and 27. The addition of optics to the simulation, illustrated in Fig. 31, reduces the fraction of misidentified pixels within each reflectance area, where optical blur is the main source of error, and increases the fraction of these pixels near the reflectance transitions, where spatial aliasing becomes the main source of error. Nevertheless, both simulations demonstrate that Richter’s recovery technique is robust to atmospheric uncertainties, i.e., perturbations in the surface irradiance of up to 15%, for a wide range of visibility

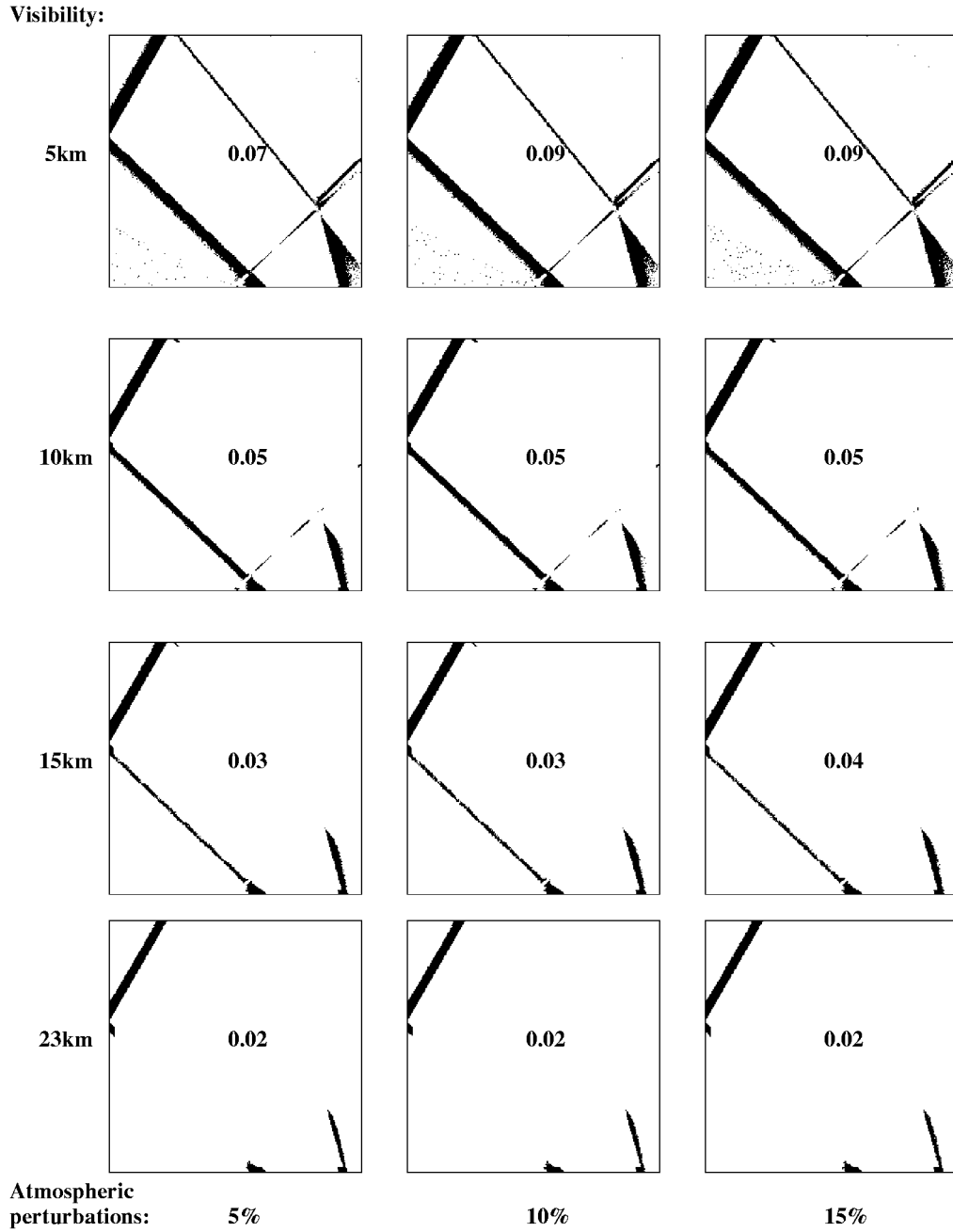


Figure 30: Location of misidentified reflectance signatures after applying Richter reflectance recovery from radiance acquired with perturbations of the total irradiance of 5%, 10% and 15%, for  $\theta_z = 30^\circ$ . The global fraction of mismatched pixels is marked on each image.



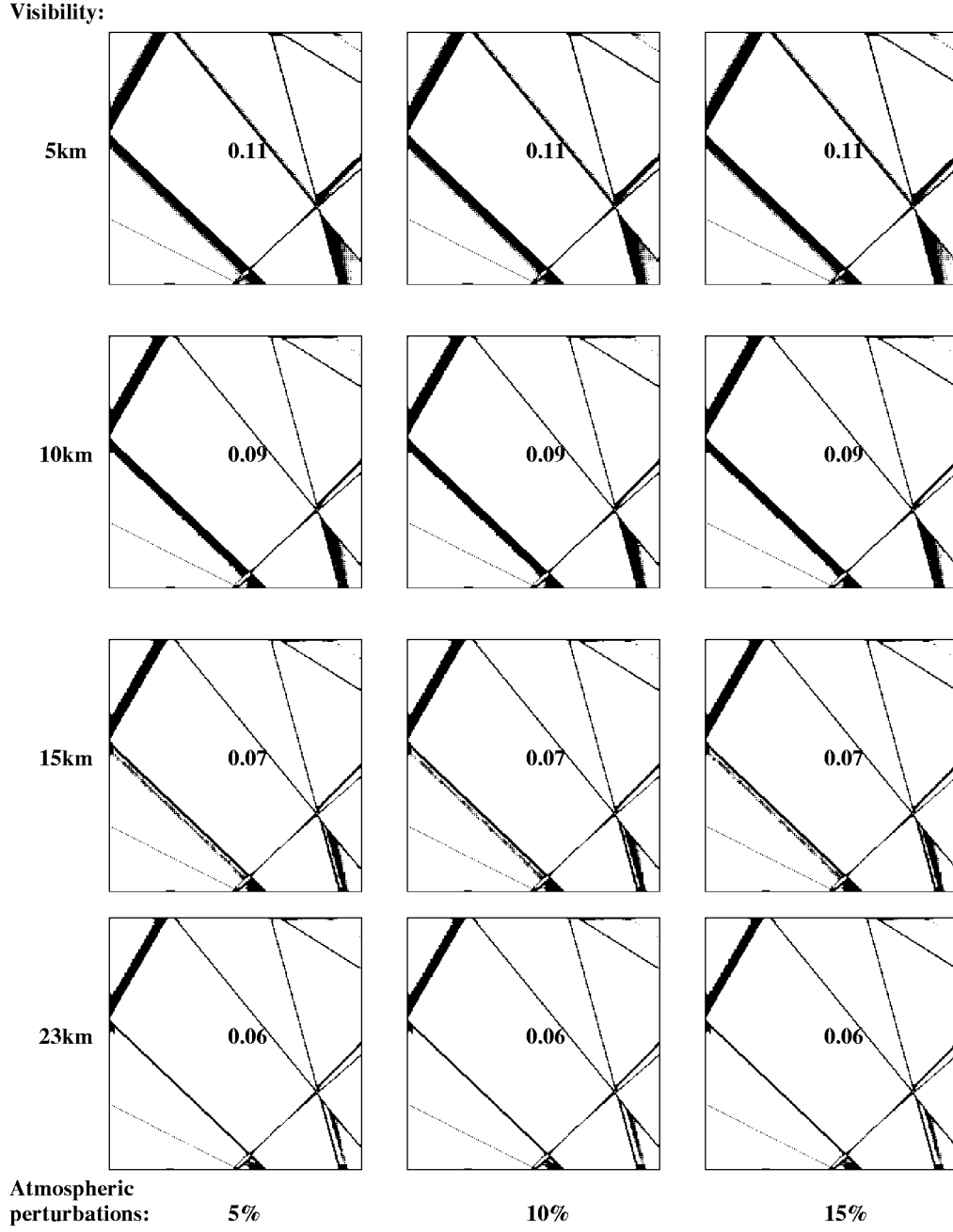


Figure 31: Location of misidentified reflectance signatures after applying Richter reflectance recovery from radiance acquired with perturbations of the total irradiance of 5%, 10% and 15%, for  $\theta_z = 30^\circ$ ,  $\sigma_g(\lambda_i) = 0.6$ , and electronic SNR of 64 across the spectral bands. The global fraction of mismatched pixels is marked on each image.

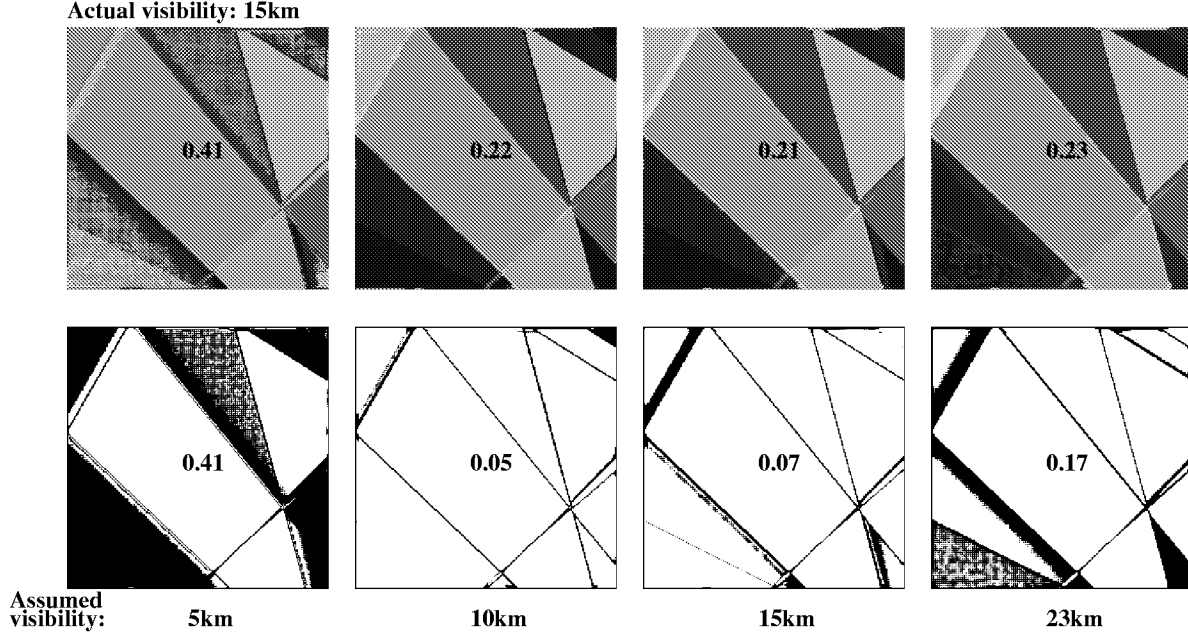


Figure 32: Image of the recovered reflectance (top) and the location of misidentified pixels (bottom) after Richter’s reflectance recovery. The global *rmse* is marked on the top row, and the global fraction of mismatched pixels is marked on the bottom row.

conditions, provided that the sensor noise is relatively low.

## 7.5 Incorrect Acquisition Assumptions

This section evaluates the robustness of Richter’s recovery technique to wrong acquisition assumptions. Figure 32 shows the identification results of simulations with Richter’s recovery from radiance measurements with an actual visibility of 15km, when the recovery process incorrectly assumes visibilities of 5km, 10km, and 23km, respectively. Table A.11 in Appendix A.3 summarizes the local performance of the identification of each reflectance area in the target. The hyper-spectral radiance target is acquired with  $\theta_z = 30^\circ$ , 10% uncertainty in the reflectance signature  $\rho$ , 10% perturbations of the irradiance  $E$ , 10% perturbation of the path radiance  $L_p$ , adjacency effects with  $s = 3$ , sensor noise of 5%, and camera parameters characterized by  $\sigma_g(\lambda_i) = 0.6$  and electronic noise with SNR of 64 across the spectral bands. As before, the hyper-spectral reflectance cube is visualized by assigning the pre-designated gray level to each recovered spectral signature, where the global *rmse* is marked on each recovery (Fig. 32 top). The identification process is visualized by assigning a black level to misidentified pixels, where the global fraction of misidentified pixels

is marked on each visualization (Fig. 32 bottom).

Results show a misidentification error of 7% for correct visibility assumption, where the location of most of the misidentified pixels is at the borders between reflectance signatures. Oats is completely misidentified when assuming a slightly worse visibility condition of 10km instead of the actual visibility of 15km (Table A.11). However, the global misidentification fraction slightly decreases from 7% to 5%, mainly at the borders between reflectance areas, and probably because of the change in  $w$  from 11 to 9 pixels. Assuming a slightly better visibility condition of 23km instead of the actual 15km increases the fraction of misidentified pixels to 17%, where barley is mainly identified as oats (64%), burr oak as sycamore (59%), multi-mineral soil sample as wet sand (52%), and misidentification at the borders increases. Incorrect assumption of  $V = 5\text{km}$  results in a sharp decrease in the identification accuracy, where the misidentified fraction increases to 41%. Assessment of the local identification errors in Table A.11 shows only three correctly-identified reflectance signatures: gypsum sand, silicon sand, and the Whitley county soil sample signatures, and a partial identification of 26% and 22% for the wheat and multi-mineral soil sample signatures respectively. Consequently, these results indicate that the Richter correction technique is robust to slight differences between the actual and assumed visibilities, but is increasingly sensitive to larger differences between the two.

Figures 33 and 34 show simulations of Richter’s recovery from radiance measurements with an assumed visibility of 15km and 5km respectively, when the actual visibility is 5km, 10km, 15km, and 23km, respectively. Tables A.12 and A.13 in Appendix A.3 summarize the local performance of the identification of each reflectance area in the target. All the other simulation parameters remain the same as in Fig. 32. Results indicate a misidentification error of 7% and 11% for correct visibility assumption of 15km and 5km respectively, where the location of most of the misidentified pixels is at the borders between reflectance signatures. A comparison between Fig. 32 for assumed visibility of 5km and actual visibility of 15km, and Fig. 34 for actual visibility of 15km and assumed visibility of 15 shows similar performance. A comparison between Fig. 33 and 34 shows that Richter’s recovery technique is extremely sensitive to the mismatched visibility conditions particularly when the assumed visibility is lower than the actual visibility.

Figure 33 shows that the global identification error for actual visibility of 5km and assumed visibility of 15km increases from 11% (correct visibility assumption) to 59%, where only gypsum sand and silicon sand are correctly identified. The identification error decreases as the actual visibility increases. The misidentification fraction in Fig. 33 decreases from 59% to 31% when the actual visibility increases from 5km to 10km. The process in this case correctly identifies oats, wheat, silver maple, gypsum sand, silicon sand and the Whitley county soil reflectance signatures. The identification near the edges for an actual

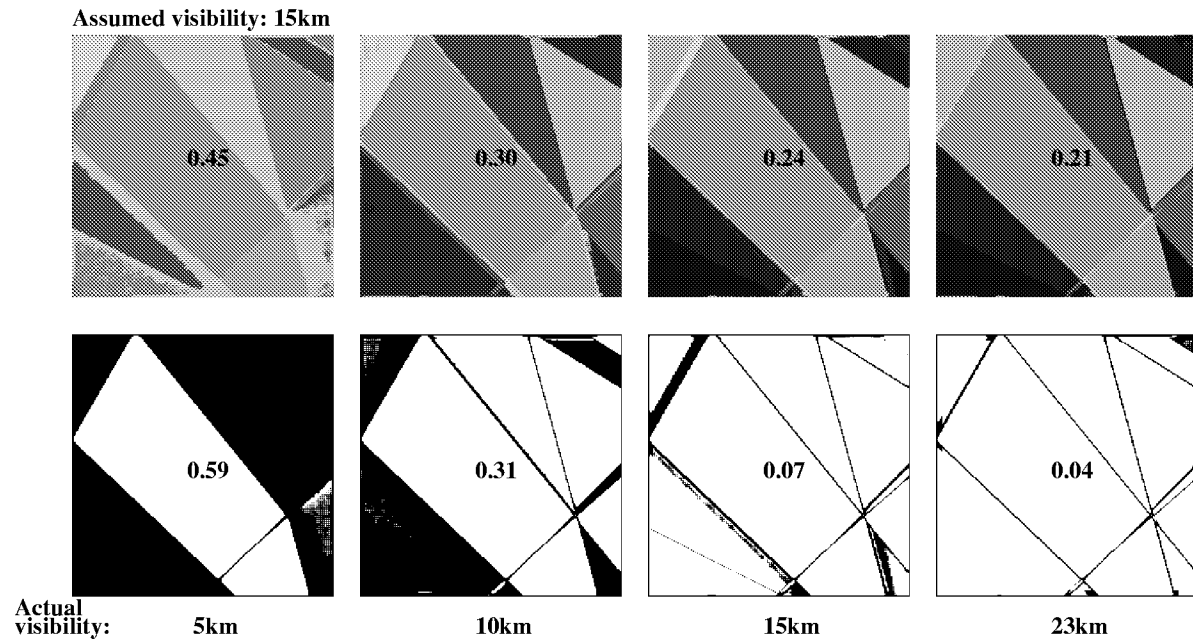


Figure 33: Image of the recovered reflectance (top) and the location of misidentified pixels (bottom) after Richter's reflectance recovery. The global  $rmse$  is marked on each recovered image (top), and the global fraction of mismatched pixels is marked on location image (bottom).

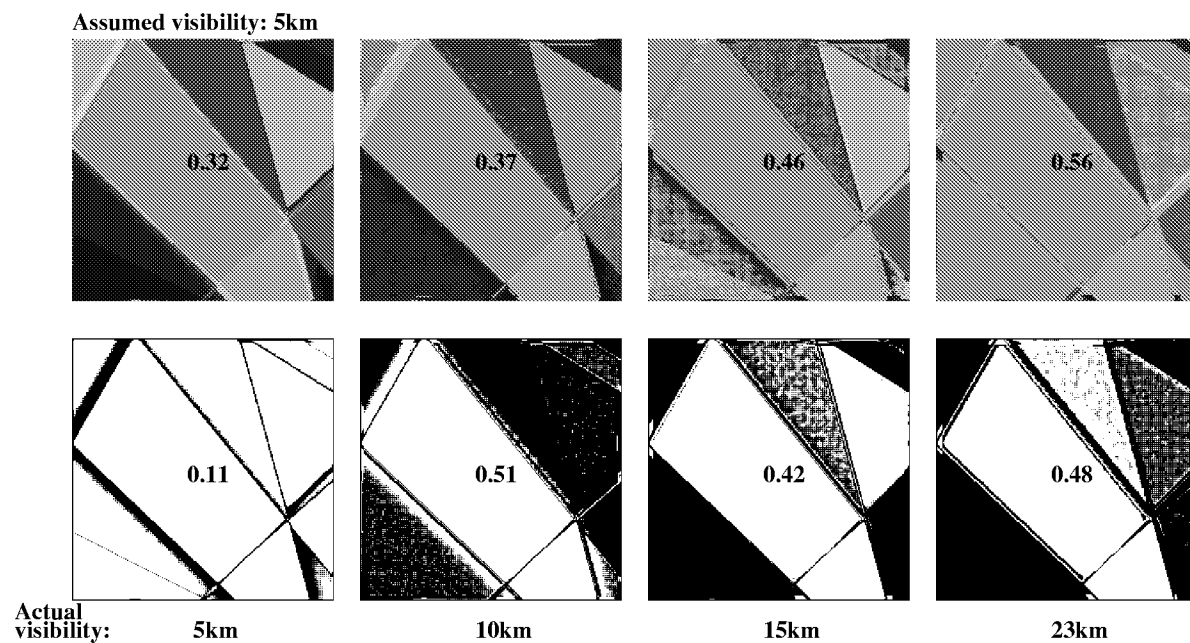


Figure 34: Image of the recovered reflectance (top) and the location of misidentified pixels (bottom) after Richter's reflectance recovery. The global  $rmse$  is marked on each recovered image (top), and the global fraction of mismatched pixels is marked on location image (bottom).

visibility of 23km is more accurate, but the process misidentifies oats as barley. The further decrease in the misidentification fraction from 7% (correct assumptions) to 4% is probably due to the change of the width parameter  $w$  from 11 to 13 pixels. This case demonstrates that the recovery and identification processes are robust to the assumption of a slightly lower visibility than the actual one.

The global identification error in Fig. 34 increases from 11% to 51%, 42%, and 48%, when the actual visibility increases to 10, 15, and 23km respectively, and the assumed visibility remains 5km. As indicated from Table A.13, only gypsum sand and silicon sand are correctly identified when the actual visibility is 10km; only gypsum sand, silicon sand, and Whitley county soil are correctly identified when the actual visibility is 15km; and only gypsum sand, silicon sand, and wheat are correctly identified when the actual visibility further increases to 23km. Consistent with previous results, these figures and the corresponding assessment tables re-emphasize that more than any other parameter, the Richter recovery technique is sensitive to incorrect estimates of the actual visibility during acquisition.

## 8 Summary

This report assessed the performance of four reflectance-recovery techniques in the context of a controlled spatio-spectral simulation that mimics the remote-sensing acquisition of hyper-spectral data. The database of reflectance signatures included 27 signatures from five different categories. The random hyper-spectral cube target consisted of 14 randomly-selected signatures from that database. Simulations included spectral and spatio-spectral deterministic evaluation of each recovery technique, and a comprehensive stochastic spatio-spectral set of simulations which assessed the sensitivity and robustness of these techniques to typical uncertainties encountered in real acquisition scenarios.

The tight control on all the simulation parameters, from reflectance, to measured radiance, to recovered signatures, enabled a close and controlled assessment of each recovery technique. Results for the albedo estimate show that albedo estimates are too high for low reflectances, and too low for high reflectances. As a result, the identification process based on albedo estimates performs poorly. Bowker’s recovery technique performs well when the original reflectance is known *a priori*, but performs poorly when this reflectance has to be estimated. Its performance for an *a priori* known reflectance signature is sensitive to decreased visibility, and is suitable for detecting irregularities in areas of known reflectance signatures.

Comparison between Richter’s spectral and spatial recoveries show that the spatial recovery technique is sensitive to noise, and boosts small perturbations in its attempt to deblur the spatial scattering blur. This technique is particularly sensitive to sensor noise. Results show high identification errors for sensor

noise above 5%, particularly for low visibility conditions. However, simulation results also suggest two ways to enhance the identification process in case of dominant sensor noise. The identification process improves when applied on Richter’s spectral recovery, without any spatial correction. Identification results improve even further with optical blur, provided that the electronic noise is relatively low. Richter’s technique is also sensitive to large inaccuracies in the estimation of the actual visibility.

In general though, results strongly indicate that Richter’s reflectance recovery technique is robust and relatively insensitive to stochastic noise, perturbations, and minor uncertainties in the atmospheric conditions. Identification results remained remarkably stable for up to 15% uncertainties in the initial reflectance signatures, and 15% perturbations in the assumed atmospheric conditions, when the sensor noise is low and the location of misidentified pixels remained centered at the reflectance boundaries. Misidentification after Richter’s recovery has more to do with the particular geometry and size of each individual reflectance area than with the ability of the recovery technique to identify the reflectance signature. Therefore, these results suggest that this recovery technique performs well for applications that require reflectance identification from remote-sensing measurements.

## Acknowledgment

This work was performed under NASA Langley Research Center contract NAS1-20431. The authors would like to recognize the extensive involvement of Richard E. Davis of NASA Langley Research Center, and express their gratitude for his substantial guidance and invaluable contribution to this research, from the initial modeling phase and throughout the analysis and interpretation phase of the results.

## A Appendix: Assessment Tables

### A.1 Deterministic Recovery Summary

Tables A.1–A.3 summarize the *rmse* of recovered reflectance signatures by the albedo, Bowker, and Richter recovery techniques, respectively, relative to the database of signatures. Both the Bowker and Richter techniques are carried out with an assumed constant initial reflectance of  $\rho(\lambda) = 0.4$ . The results confirm that this assumption does not affect the performance of the Richter recovery technique, as it performs well almost independent of the visibility and solar zenith angle conditions. By contrast, the assumption of a

constant initial reflectance of  $\rho(\lambda) = 0.4$  reduces the accuracy of the Bowker technique over its performance for known reflectances, particularly for low visibility, while it performs relatively better for high visibility of 23km.

Tables A.4–A.6 summarize the quantitative assessment of the deterministic recovery and identification process for three different atmospheric acquisition conditions. These tables summarize the *rmse* of the albedo, Bowker, and Richter recovery techniques for an assumed initial reflectance of  $\rho(\lambda) = 0.4$ . The value of  $F$  indicates the fraction of the mainly identified reflectance within the area of each reflectance in the spatio-spectral random polygon cube. For example,  $F = .99$  for the barley category in Table A.4 indicates that 99% of the barley area in the spatio-spectral random polygon cube was identified as basalt, while  $F = 0.94$  for the burr oak category indicates that 94% of the oak area in the spatio-spectral random polygon cube was identified as American elm. No  $F$  value is assigned in cases where a particular reflectance is completely unidentified. The global *rmse*, and the global fraction of correctly identified pixels  $F$  is summarized under “Global”. These tables show that the albedo approximation correctly identifies only two reflectance signatures and misidentifies 60% of the cube, while the Bowker recovery technique correctly identifies only four spectral signatures. For the same conditions, the spectral Richter technique correctly identifies all the spectral signatures, while the spatial correction with  $w = 9$  decreases the number of misidentified pixels by a factor of two. Some of the inaccuracy can be attributed to the adjacency blurring effects, particularly for reflectance signatures with few pixels and narrow geometrical areas. However, Richter’s spatial correction techniques minimizes these defects.

## A.2 Bowker Recovery with Known Reflectance Signatures

Tables A.7–A.9 summarize the performance of a stochastic simulation with Bowker’s recovery techniques, assuming known reflectances. The performance of Bowker’s technique is simulated for the set of acquisition conditions identified in this report, namely, solar zenith angle of  $\theta_z = 0^\circ$ ,  $30^\circ$ , and  $45^\circ$ , for visibility conditions of  $V = 5\text{km}$ ,  $10\text{km}$ ,  $15\text{km}$ , and  $23\text{km}$ . Adjacency effects are simulated by 10% perturbation of the path radiance  $L_p$ , and a spatial spread factor of  $s = 3$ . Additional stochastic perturbations include 10% uncertainty in the reflectance signature, irradiance perturbations of 10%, and a random sensor noise of 5% of the received radiance signal.

The tables summarize the *rmse* for each reflectance in the the hyper-spectral cube, and lists the two main identified reflectances for each category, together with their local fraction  $F$  within that category, and the global misidentification fraction  $F_m$ . Finally, the global information summarizes the global *rmse* for



Category	$\theta_z = 0^\circ$				$\theta_z = 30^\circ$				$\theta_z = 45^\circ$			
	5km	10km	15km	23km	5km	10km	15km	23km	5km	10km	15km	23km
Barley	1.322	1.046	0.932	0.849	1.342	1.045	0.926	0.842	1.489	1.145	1.003	0.902
Beans	0.981	0.739	0.640	0.568	0.987	0.729	0.627	0.555	1.105	0.802	0.680	0.595
Oats	0.838	0.640	0.560	0.501	0.840	0.629	0.546	0.488	0.937	0.689	0.590	0.520
Potatoes	0.575	0.392	0.317	0.263	0.563	0.371	0.297	0.246	0.638	0.410	0.322	0.262
Soybeans	1.008	0.813	0.733	0.674	1.023	0.813	0.728	0.668	1.130	0.886	0.785	0.71
Tobacco	1.451	1.142	1.015	0.922	1.475	1.143	1.010	0.915	1.639	1.254	1.095	0.982
Wheat	0.876	0.696	0.623	0.569	0.884	0.691	0.614	0.561	0.979	0.754	0.662	0.597
Fallow field	1.113	0.901	0.813	0.748	1.131	0.902	0.809	0.744	1.249	0.984	0.874	0.795
American Elm	0.382	0.258	0.209	0.173	0.370	0.242	0.194	0.161	0.419	0.266	0.209	0.171
Silver Maple	0.326	0.220	0.179	0.149	0.317	0.207	0.167	0.140	0.359	0.229	0.181	0.149
Burr Oak	2.331	1.847	1.646	1.500	2.380	1.859	1.649	1.499	2.642	2.042	1.792	1.613
Ponderosa Pine	1.201	0.963	0.864	0.793	1.220	0.963	0.860	0.788	1.349	1.052	0.930	0.843
Sycamore	1.308	1.035	0.923	0.841	1.328	1.035	0.917	0.835	1.474	1.134	0.993	0.894
Blue Grass	4.086	3.219	2.861	2.599	4.183	3.253	2.877	2.609	4.651	3.582	3.136	2.816
Basalt	0.286	0.234	0.214	0.200	0.278	0.224	0.204	0.190	0.305	0.239	0.214	0.197
Dry Red Clay	0.277	0.208	0.180	0.159	0.282	0.207	0.178	0.157	0.317	0.229	0.194	0.170
Wet Red Clay	0.642	0.466	0.393	0.340	0.644	0.456	0.382	0.330	0.725	0.505	0.417	0.355
Gypsum Sand	0.140	0.111	0.098	0.089	0.169	0.133	0.116	0.103	0.195	0.155	0.135	0.120
Silicon Sand	0.169	0.128	0.112	0.099	0.198	0.150	0.129	0.113	0.228	0.175	0.150	0.130
Multi-Mineral	1.045	0.710	0.573	0.472	1.030	0.679	0.543	0.448	1.168	0.756	0.594	0.482
Whitley County	0.345	0.237	0.194	0.163	0.333	0.222	0.181	0.153	0.375	0.244	0.194	0.162
Powell Grassland	0.164	0.126	0.111	0.101	0.167	0.127	0.112	0.102	0.187	0.140	0.123	0.110
Dry Sand	0.149	0.116	0.104	0.095	0.155	0.120	0.107	0.097	0.174	0.133	0.118	0.107
Wet Sand	0.613	0.440	0.369	0.319	0.602	0.420	0.351	0.303	0.677	0.462	0.378	0.322
Water	2.749	2.029	1.732	1.514	2.785	2.017	1.711	1.494	3.134	2.240	1.876	1.618

Table A.1: The *rmse* between the original reflectance signature and its albedo recovery.

Category	$\theta_z = 0^\circ$				$\theta_z = 30^\circ$				$\theta_z = 45^\circ$			
	5km	10km	15km	23km	5km	10km	15km	23km	5km	10km	15km	50km
Barley	9.655	4.444	2.975	2.067	9.376	4.363	2.933	2.044	8.889	4.218	2.857	2.001
Beans	7.139	3.329	2.222	1.528	6.970	3.278	2.196	1.540	6.652	3.185	2.151	1.490
Oats	6.218	2.891	1.932	1.331	6.065	2.846	1.908	1.320	5.784	2.765	1.869	1.350
Potatoes	4.452	2.129	1.419	0.962	4.367	2.104	1.407	0.957	4.211	2.058	1.386	0.946
Soybeans	7.445	3.411	2.288	1.596	7.220	3.346	2.254	1.578	6.829	3.227	2.192	1.544
Tobacco	10.486	4.832	3.236	2.245	10.188	4.745	3.189	2.221	9.663	4.590	3.108	2.174
Wheat	6.487	2.986	2.001	1.391	6.303	2.933	1.974	1.377	5.979	2.837	1.923	1.350
Fallow field	8.230	3.767	2.527	1.764	7.979	3.694	2.489	1.744	7.541	3.561	2.419	1.705
American Elm	3.013	1.447	0.966	0.655	2.957	1.432	0.958	0.652	2.857	1.403	0.946	0.645
Silver Maple	2.546	1.227	0.819	0.555	2.501	1.214	0.813	0.553	2.418	1.190	0.803	0.548
Burr Oak	16.777	7.710	5.164	3.590	16.278	7.563	5.086	3.548	15.407	7.299	4.947	3.469
Ponderosa Pine	8.852	4.063	2.725	1.899	8.587	3.986	2.685	1.877	8.124	3.846	2.611	1.836
Sycamore	9.509	4.377	2.932	2.037	9.234	4.298	2.890	2.016	8.752	4.155	2.815	1.973
Blue Grass	29.159	13.417	8.985	6.241	28.290	13.160	8.847	6.164	26.769	12.695	8.602	6.024
Basalt	2.353	1.089	0.730	0.508	2.292	1.072	0.722	0.504	2.185	1.041	0.707	0.497
Dry red clay	2.028	0.949	0.632	0.433	1.985	0.937	0.626	0.430	1.906	0.914	0.616	0.425
Wet red clay	4.793	2.250	1.497	1.020	4.688	2.218	1.481	1.013	4.500	2.162	1.453	1.037
Gypsum sand	0.117	0.060	0.040	0.026	0.116	0.059	0.040	0.027	0.115	0.059	0.040	0.027
Silicon sand	0.262	0.130	0.089	0.062	0.260	0.130	0.090	0.063	0.256	0.131	0.091	0.065
Multi-mineral	7.770	3.721	2.479	1.679	7.617	3.677	2.457	1.668	7.343	3.594	2.417	1.646
Whitley County	2.938	1.401	0.933	0.633	2.881	1.386	0.926	0.630	2.779	1.356	0.913	0.623
Powell Grassland	1.366	0.645	0.430	0.294	1.340	0.638	0.427	0.293	1.292	0.624	0.422	0.290
Dry sand	1.193	0.563	0.376	0.257	1.171	0.557	0.373	0.256	1.129	0.545	0.368	0.254
Wet sand	4.762	2.251	1.501	1.023	4.661	2.223	1.487	1.016	4.480	2.169	1.462	1.003
Water	19.343	9.052	6.035	4.131	18.885	8.913	5.962	4.092	18.048	8.665	5.837	4.02

Table A.2: The *rmse* between the original reflectance signature and its Bowker recovery.

Category	$\theta_z = 0^\circ$				$\theta_z = 30^\circ$				$\theta_z = 45^\circ$			
	5km	10km	15km	23km	5km	10km	15km	23km	5km	10km	15km	23km
Barley	0.021	0.017	0.017	0.017	0.024	0.019	0.019	0.019	0.028	0.023	0.022	0.022
Beans	0.019	0.016	0.015	0.015	0.021	0.018	0.017	0.017	0.025	0.021	0.021	0.020
Oats	0.018	0.015	0.014	0.014	0.021	0.017	0.016	0.016	0.025	0.020	0.020	0.020
Potatoes	0.015	0.013	0.013	0.013	0.018	0.015	0.015	0.015	0.021	0.018	0.018	0.017
Soybeans	0.020	0.016	0.016	0.016	0.022	0.018	0.018	0.018	0.027	0.022	0.021	0.021
Tobacco	0.021	0.017	0.017	0.017	0.024	0.020	0.019	0.019	0.029	0.024	0.023	0.023
Wheat	0.020	0.016	0.016	0.016	0.023	0.019	0.018	0.018	0.027	0.022	0.022	0.022
Fallow field	0.020	0.016	0.016	0.016	0.023	0.018	0.018	0.018	0.027	0.022	0.021	0.021
American Elm	0.014	0.013	0.013	0.013	0.017	0.015	0.014	0.014	0.020	0.017	0.017	0.017
Silver Maple	0.014	0.013	0.013	0.013	0.016	0.015	0.015	0.015	0.019	0.017	0.017	0.017
Burr Oak	0.025	0.021	0.020	0.020	0.029	0.023	0.022	0.022	0.034	0.028	0.027	0.027
Ponderosa Pine	0.021	0.018	0.017	0.017	0.024	0.020	0.020	0.020	0.029	0.024	0.023	0.023
Sycamore	0.021	0.018	0.017	0.017	0.024	0.020	0.020	0.020	0.029	0.024	0.023	0.023
Blue Grass	0.028	0.023	0.023	0.022	0.031	0.026	0.025	0.025	0.036	0.030	0.029	0.029
Basalt	0.015	0.013	0.013	0.013	0.017	0.014	0.014	0.015	0.020	0.017	0.017	0.017
Dry red clay	0.012	0.012	0.012	0.012	0.014	0.013	0.013	0.013	0.016	0.015	0.015	0.016
Wet red clay	0.014	0.013	0.013	0.013	0.017	0.014	0.014	0.014	0.020	0.017	0.017	0.017
Gypsum sand	0.008	0.009	0.010	0.011	0.009	0.010	0.011	0.012	0.009	0.011	0.012	0.013
Silicon sand	0.011	0.011	0.011	0.012	0.013	0.012	0.013	0.013	0.015	0.015	0.015	0.015
Multi-mineral	0.016	0.014	0.013	0.013	0.019	0.016	0.015	0.015	0.023	0.019	0.018	0.017
Whitley County	0.014	0.012	0.012	0.012	0.016	0.014	0.014	0.014	0.019	0.016	0.016	0.016
Powell Grassland	0.012	0.011	0.011	0.012	0.013	0.012	0.013	0.013	0.016	0.014	0.015	0.015
Dry sand	0.011	0.011	0.011	0.012	0.013	0.012	0.012	0.013	0.015	0.014	0.014	0.015
Wet sand	0.017	0.014	0.013	0.013	0.019	0.016	0.015	0.015	0.023	0.019	0.018	0.018
Water	0.022	0.017	0.016	0.016	0.025	0.020	0.018	0.018	0.030	0.024	0.023	0.022

Table A.3: The *rmse* between the original reflectance signature and its Richter recovery.

Category	Albedo (Eq. 18)			Bowker (Eq. 26)			Richter (spectral) (Eq. 27)			Richter (spatial) (Eq. 28)		
	$\epsilon$	Identified mainly as	$F$	$\epsilon$	Identified mainly as	$F$	$\epsilon$	Identified mainly as	$F$	$\epsilon$	Identified mainly as	$F$
Barley	0.49	Basalt	0.99	1.04	Gypsum	1.0	0.04	Barley	0.84	0.02	Barley	0.89
Beans	0.51	Elm	0.50	1.03	Gypsum	1.0	0.04	Beans	0.84	0.02	Beans	0.91
Oats	0.44	Basalt	1.0	1.06	Gypsum	1.0	0.02	Oats	1.0	0.01	Oats	1.0
Potatoes	0.83	D. sand	0.74	0.20	Potatoes	0.70	0.54	D. sand	0.62	0.09	Potatoes	1.0
Wheat	0.54	D. sand	0.97	0.95	Silicon	1.0	0.04	Wheat	0.98	0.02	Wheat	1.0
Fallow field	0.42	Basalt	1.0	1.06	Silicon	1.0	0.05	Fallow	1.0	0.05	Fallow	1.0
Silver Maple	0.51	D. sand	0.98	0.96	Silicon	1.0	0.02	Maple	1.0	0.02	Maple	1.0
Burr Oak	0.73	Elm	0.94	1.02	Silicon	0.89	0.09	Oak	0.93	0.04	Oak	1.0
Wet Red Clay	0.91	Basalt	1.0	0.21	W R Clay	0.69	0.60	Powell	0.97	0.05	W R Clay	1.0
Gypsum sand	0.28	Gypsum	1.0	0.19	Gypsum	1.0	0.05	Gypsum	1.0	0.03	Gypsum	1.0
Silicon sand	0.53	Silicon	1.0	0.21	Silicon	1.0	0.08	Silicon	1.0	0.05	Silicon	1.0
Multi-mineral	0.54	Basalt	1.0	1.01	Silicon	1.0	0.09	M. mineral	0.66	0.06	M. mineral	0.67
Whitley soil	0.43	Basalt	1.0	1.04	Gypsum	1.0	0.02	Whitley	1.0	0.01	Whitley	1.0
Water	0.77	Basalt	1.0	0.64	Silicon	0.5	0.39	W. sand	1.0	0.02	Water	1.0
Global	0.45		0.4	0.80		0.4	0.09		0.94	0.04		0.96

Table A.4: Performance assessment of the identification process for  $\theta_z = 0^\circ$  and  $V = 23\text{km}$ .

Category	Albedo (Eq. 18)			Bowker (Eq. 26)			Richter (spectral) (Eq. 27)			Richter (spatial) (Eq. 28)		
	$\epsilon$	Identified mainly as	$F$	$\epsilon$	Identified mainly as	$F$	$\epsilon$	Identified mainly as	$F$	$\epsilon$	Identified mainly as	$F$
Barley	0.54	Basalt	1.0	1.48	Silicon	1.0	0.04	Barley	0.83	0.03	Barley	0.88
Beans	0.56	Powell	1.0	1.47	Silicon	1.0	0.05	Beans	0.83	0.03	Beans	0.89
Oats	0.48	Basalt	1.0	1.50	Silicon	1.0	0.02	Oats	1.0	0.02	Oats	1.0
Potatoes	0.92	Gypsum	0.60	0.28	Potatoes	0.60	0.67	D. sand	0.80	0.11	Potatoes	1.0
Wheat	0.61	D. sand	0.93	1.36	Silicon	1.0	0.05	Wheat	0.95	0.03	Wheat	1.0
Fallow field	0.45	Basalt	1.0	1.50	Silicon	1.0	0.07	Fallow	1.0	0.07	Fallow	1.0
Silver Maple	0.56	D. sand	0.97	1.37	Silicon	1.0	0.03	Maple	1.0	0.02	Maple	1.0
Burr Oak	0.83	Elm	0.66	1.45	Silicon	1.0	0.11	Oak	0.89	0.05	Oak	1.0
Wet Red Clay	1.01	Basalt	0.54	1.30	W R Clay	0.59	0.75	Powell	0.49	0.07	W R Clay	0.69
Gypsum sand	0.34	Gypsum	1.0	0.27	Gypsum	1.0	0.06	Gypsum	1.0	0.03	Gypsum	1.0
Silicon sand	0.65	Silicon	1.0	0.31	Silicon	1.0	0.10	Silicon	1.0	0.06	Silicon	1.0
Multi-mineral	0.60	Basalt	1.0	1.44	Silicon	1.0	0.11	M. mineral	0.62	0.08	M. mineral	0.64
Whitley soil	0.47	Basalt	1.0	1.48	Silicon	1.0	0.02	Whitley	1.0	0.01	Whitley	1.0
Water	0.86	Basalt	1.0	0.91	Silicon	1.0	0.49	Whitley	1.0	0.03	Water	1.0
Global	0.50		0.4	1.13		0.4	0.10		0.93	0.05		0.96

Table A.5: Performance assessment of the identification process for  $\theta_z = 30^\circ$  and  $V = 15\text{km}$ .

Category	Albedo (Eq. 18)			Bowker (Eq. 26)			Richter (spectral) (Eq. 27)			Richter (spatial) (Eq. 28)		
	$\epsilon$	Identified mainly as	$F$	$\epsilon$	Identified mainly as	$F$	$\epsilon$	Identified mainly as	$F$	$\epsilon$	Identified mainly as	$F$
Barley	0.84	Basalt	0.99	4.49	Silicon	1.0	0.07	Barley	0.81	0.14	Barley	0.89
Beans	0.87	Basalt	0.97	4.50	Silicon	1.0	0.07	Beans	0.80	0.06	Beans	0.89
Oats	0.77	Basalt	1.0	4.55			0.03	Oats	1.0	0.04	Oats	1.0
Potatoes	1.25	Gypsum	1.0	0.82	Wheat	0.27	1.12	Gypsum	0.80	3.00	Elm	0.57
Wheat	0.94	D. sand	0.99	4.13	Silicon	0.89	0.09	Wheat	0.89	0.12	Wheat	0.99
Fallow field	0.71	Basalt	1.0	4.55			0.12	Fallow	1.0	0.12	Fallow	1.0
Silver Maple	0.87	D. sand	1.0	4.15	Silicon	0.98	0.05	Maple	0.97	0.22	Maple	0.99
Burr Oak	1.27	D. sand	1.0	4.43	Silicon	0.99	0.20	Oak	0.62	1.52	Oak	0.99
Wet Red Clay	1.37	Gypsum	0.95	0.87	Silicon	0.26	1.23	Gypsum	0.64	2.92	Fallow	0.85
Gypsum sand	0.52	Gypsum	1.0	0.87	Gypsum	1.0	0.09	Gypsum	1.0	0.04	Gypsum	1.0
Silicon sand	1.01	Silicon	1.0	0.93	Silicon	1.0	0.16	Silicon	1.0	0.35	Silicon	1.0
Multi-mineral	0.94	Basalt	1.0	4.39	Silicon	0.93	0.18	M. mineral	0.58	0.11	M. mineral	0.62
Whitley soil	0.75	Basalt	1.0	4.48			0.04	Whitley	0.96	0.03	Whitley	0.99
Water	1.27	Basalt	1.0	2.78	Silicon	0.5	0.84	Basalt	1.0	5.34	Water	1.0
Global	0.78		0.4	3.44		0.43	0.17		0.91	0.07		0.96

Table A.6: Performance assessment of the identification process for  $\theta_z = 45^\circ$  and  $V = 5\text{km}$ .

Category	$V = 5\text{km}$				$V = 10\text{km}$				$V = 15\text{km}$				$V = 23\text{km}$			
	$\epsilon$	Identified mainly as	$F$	$F_m$	$\epsilon$	Identified mainly as	$F$	$F_m$	$\epsilon$	Identified mainly as	$F$	$F_m$	$\epsilon$	Identified mainly as	$F$	$F_m$
Barley	0.41	Oats	0.78	1.0	0.21	Barley	0.65	0.35	0.16	Barley	0.76	0.24	0.13	Barley	0.78	0.22
		Powell	0.09			Oats	0.21			Oats	0.13			Oats	0.13	
Beans	0.43	Elm	0.39	0.99	0.22	Beans	0.62	0.38	0.17	Beans	0.72	0.28	0.14	Beans	0.77	0.23
		Oats	0.37			Oats	0.15			Elm	0.11			Elm	0.11	
Oats	0.25	Oats	1.0	0.0	0.13	Oats	1.0	0.0	0.11	Oats	1.0	0.0	0.10	Oats	1.0	0.0
Wheat	0.47	Wheat	0.66	0.34	0.26	Wheat	0.79	0.21	0.21	Wheat	0.84	0.16	0.18	Wheat	0.90	0.10
		D. sand	0.15			D. sand	0.15			D. sand	0.11			D. sand	0.06	
Silver Maple	0.33	Maple	0.86	0.14	0.20	Maple	0.94	0.06	0.17	Maple	0.97	0.03	0.16	Maple	1.0	0.0
		D. sand	0.06			D. sand	0.03			D. sand	0.01					
Burr Oak	0.68	D R clay	0.58	1.0	0.37	D R clay	0.78	1.0	0.29	Oak	0.21	0.79	0.24	Oak	0.69	0.31
		D. sand	0.30			Sycamore	0.17			Sycamore	0.57			Sycamore	0.21	
Gypsum sand	0.60	Gypsum	0.99	0.01	0.34	Gypsum	1.0	0.0	0.27	Gypsum	1.0	0.0	0.24	Gypsum	1.0	0.0
		Silicon	0.004													
Silicon sand	0.91	Silicon	1.0	0.0	0.51	Silicon	1.0	0.0	0.41	Silicon	1.0	0.0	0.35	Silicon	0.0	0.0
Multi-mineral	0.77	W. sand	0.58	1.0	0.36	M. Min	0.44	0.56	0.25	M. Min	0.51	0.49	0.18	M. Min	0.56	0.44
		Basalt	0.22			W. sand	0.28			W. sand	0.29			W. sand	0.31	
Whitley soil	0.25	Whitley	0.86	0.14	0.13	Whitley	0.96	0.04	0.10	Whitley	0.98	0.02	0.09	Whitley	1.0	0.0
		Oats	0.07			Oats	0.03			Oats	0.01					
Global	0.71			0.36	0.36			0.16	0.27			0.11	0.22			0.09

Table A.7: Performance assessment of Bowker's recovery for  $\theta_z = 0^\circ$ .

Category	$V = 5\text{km}$				$V = 10\text{km}$				$V = 15\text{km}$				$V = 23\text{km}$			
	$\varepsilon$	Identified mainly as	$F$	$F_m$	$\varepsilon$	Identified mainly as	$F$	$F_m$	$\varepsilon$	Identified mainly as	$F$	$F_m$	$\varepsilon$	Identified mainly as	$F$	$F_m$
Barley	0.42	Oats	0.78	1.0	0.21	Barley	0.60	0.39	0.16	Barley	0.76	0.24	0.13	Barley	0.78	0.21
		Powell	0.09			Oats	0.25			Oats	0.13			Oats	0.14	
Beans	0.43	Elm	0.54	1.0	0.22	Beans	0.61	0.39	0.17	Beans	0.72	0.28	0.14	Beans	0.77	0.22
		Oats	0.23			Oats	0.15			Elm	0.11			Elm	0.11	
Oats	0.26	Oats	0.98	0.02	0.13	Oats	1.0	0.0	0.11	Oats	1.0	0.0	0.10	Oats	1.0	0.0
		Elm	0.02													
Wheat	0.47	Wheat	0.64	0.35	0.26	Wheat	0.79	0.21	0.21	Wheat	0.85	0.15	0.18	Wheat	0.90	0.10
		D. sand	0.15			D. sand	0.15			D. sand	0.11			D. sand	0.05	
Silver Maple	0.34	Maple	0.87	0.13	0.20	Maple	0.94	0.06	0.17	Maple	0.97	0.02	0.16	Maple	1.0	0.0
		D. sand	0.06			D. sand	0.03			D. sand	0.01					
Burr Oak	0.67	D R clay	0.61	1.0	0.27	D R clay	0.76	0.99	0.29	Oak	0.22	0.78	0.24	Oak	0.67	0.31
		D. sand	0.29			Sycamore	0.19			Sycamore	0.55			Sycamore	0.22	
Gypsum sand	0.60	Gypsum	0.99	0.005	0.34	Gypsum	1.0	0.0	0.27	Gypsum	1.0	0.0	0.24	Gypsum	1.0	0.0
		Silicon	0.004													
Silicon sand	0.90	Silicon	1.0	0.0	0.51	Silicon	1.0	0.0	0.41	Silicon	1.0	0.0	0.35	Silicon	1.0	0.0
Multi-mineral	0.76	W. sand	0.58	1.0	0.36	M. Min	0.43	0.57	0.25	M. Min	0.51	0.49	0.18	M. Min	0.56	0.43
		Basalt	0.23			W. sand	0.29			W. sand	0.29			W. sand	0.32	
Whitley soil	0.27	Whitley	0.85	0.15	0.13	Whitley	0.96	0.04	0.10	Whitley	0.98	0.02	0.09	Whitley	1.0	0.0
		Basalt	0.06			Oats	0.03			Oats	0.01					
Global	0.70			0.36	0.36			0.16	0.27			0.11	0.22			0.09

Table A.8: Performance assessment of Bowker's recovery for  $\theta_z = 30^\circ$ .



Category	$V = 5\text{km}$				$V = 10\text{km}$				$V = 15\text{km}$				$V = 23\text{km}$			
	$\varepsilon$	Identified mainly as	$F$	$F_m$	$\varepsilon$	Identified mainly as	$F$	$F_m$	$\varepsilon$	Identified mainly as	$F$	$F_m$	$\varepsilon$	Identified mainly as	$F$	$F_m$
Barley	0.44	Oats	0.74	1.0	0.22	Barley	0.42	0.58	0.16	Barley	0.74	0.26	0.13	Barley	0.78	0.22
		Powell	0.14			Oats	0.43			Oats	0.15			Oats	0.14	
Beans	0.45	Elm	0.74	1.0	0.22	Beans	0.43	0.43	0.17	Beans	0.72	0.28	0.14	Beans	0.77	0.23
		Gypsum	0.09			Oats	0.19			Elm	0.11			Elm	0.11	
Oats	0.30	Oats	0.72	0.28	0.15	Oats	1.0	0.0	0.11	Oats	1.0	0.0	0.10	Oats	1.0	0.0
		Elm	0.26													
Wheat	0.49	Wheat	0.56	0.44	0.26	Wheat	0.79	0.21	0.21	Wheat	0.85	0.15	0.18	Wheat	0.90	0.10
		D. sand	0.17			D. sand	0.15			D. sand	0.10			D. sand	0.05	
Silver Maple	0.37	Maple	0.80	0.20	0.21	Maple	0.95	0.05	0.17	Maple	0.98	0.02	0.16	Maple	1.0	0.0
		Elm	0.09			D. sand	0.03			D. sand	0.01					
Burr Oak	0.65	D R clay	0.62	1.0	0.36	D R clay	0.75	1.0	0.28	Oak	0.22	0.78	0.24	Oak	0.69	0.31
		D. sand	0.26			Sycamore	0.21			Sycamore	0.56			Sycamore	0.11	
Gypsum sand	0.62	Gypsum	0.99	0.0	0.34	Gypsum	1.0	0.0	0.28	Gypsum	1.0	0.0	0.24	Gypsum	1.0	0.0
		Silicon	0.004													
Silicon sand	0.90	Silicon	1.0	0.0	0.51	Silicon	1.0	0.0	0.41	Silicon	1.0	0.0	0.35	Silicon	1.0	0.0
Multi-mineral	0.75	W. sand	0.58	1.0	0.36	M. Min	0.42	0.58	0.25	M. Min	0.50	0.50	0.18	M. Min	0.56	0.44
		Basalt	0.24			W. sand	0.08			W. sand	0.30			W. sand	0.32	
Whitley soil	0.30	Whitley	0.61	0.39	0.14	Whitley	0.96	0.04	0.11	Whitley	0.98	0.02	0.09	Whitley	1.0	0.0
		Basalt	0.34			Oats	0.03			Oats	0.01					
Global	0.69			0.41	0.35			0.18	0.27			0.12	0.22			0.09

Table A.9: Performance assessment of Bowker's recovery for  $\theta_z = 45^\circ$ .

Category	V = 5km				V = 10km				V = 15km				V = 23km			
	$\varepsilon$	Identified mainly as	$F$	$F_m$	$\varepsilon$	Identified mainly as	$F$	$F_m$	$\varepsilon$	Identified mainly as	$F$	$F_m$	$\varepsilon$	Identified mainly as	$F$	$F_m$
Barley	0.25	Oats	0.81	0.92	0.13	Barley	0.92	0.08	0.11	Barley	0.87	0.13	0.09	Barley	0.78	0.21
		Powell	0.10			Oats	0.25			Oats	0.12			Oats	0.08	
Beans	0.26	Elm	0.53	0.96	0.14	Beans	0.82	0.18	0.11	Beans	0.90	0.10	0.10	Beans	0.99	0.22
		Oats	0.35			Oats	0.13			Oats	0.10			Oats	0.006	
Oats	0.21	Oats	1.0	0.0	0.11	Oats	1.0	0.0	0.09	Oats	1.0	0.0	0.08	Oats	1.0	0.0
Wheat	0.29	Wheat	0.86	0.14	0.18	Wheat	1.0	0.0	0.16	Wheat	1.0	0.0	0.15	Wheat	1.0	0.0
		D R clay	0.9													
Silver Maple	0.28	Maple	0.98	0.02	0.18	Maple	1.0	0.0	0.16	Maple	1.0	0.0	0.14	Maple	1.0	0.0
		D. sand	0.01													
Burr Oak	0.33	D R clay	0.74	0.93	0.23	Oak	0.94	0.06	0.21	Oak	1.0	0.0	0.20	Oak	0.67	0.31
		Sycamore	0.17			Sycamore	0.05									
Gypsum sand	0.44	Gypsum	1.0	0.0	0.27	Gypsum	1.0	0.0	0.23	Gypsum	1.0	0.0	0.21	Gypsum	1.0	0.0
Silicon sand	0.54	Silicon	1.0	0.0	0.36	Silicon	1.0	0.0	0.32	Silicon	1.0	0.0	0.29	Silicon	1.0	0.0
Multi-mineral	0.29	W. sand	0.72	0.92	0.15	M. Min	0.57	0.42	0.12	M. Min	0.63	0.37	0.09	M. Min	0.67	0.33
		Basalt	0.23			W. sand	0.41			W. sand	0.36			W. sand	0.33	
Whitley soil	0.24	Whitley	0.97	0.03	0.12	Whitley	1.0	0.0	0.09	Whitley	1.0	0.0	0.08	Whitley	1.0	0.0
		Oats	0.02													
Global	0.36			0.30	0.22			0.07	0.19			0.04	0.17			0.02

Table A.10: Performance assessment of the identification process after Richter recovery for  $\theta_z = 30^\circ$ .

the entire cube, and the global fraction of misidentified pixels. This stochastic assessment shows that the main weakness of the Bowker recovery technique is the necessity to have an accurate knowledge of the path radiance. With that knowledge, this technique is as robust to perturbations as is the Richter technique. It also demonstrates that the identification process improves with improved visibility conditions.

### A.3 Richter Reflectance Recovery Summary

Table A.10 summarizes the quantitative performance of Richter’s recovery technique for a stochastic spatio-spectral end-to-end radiance measurement simulation. The atmospheric acquisition conditions are  $\theta_z = 30^\circ$ , and  $V = 5\text{km}, 10\text{km}, 15\text{km}, \text{ and } 23\text{km}$ . Adjacency effects are simulated by 10% perturbation of

the path radiance  $L_p$ , and a spatial spread factor of  $s = 3$ . Additional stochastic perturbation includes a 10% uncertainty in the reflectance signature, irradiance perturbations of 10%, and a random sensor noise  $n_{\Phi_i}$  of 5% of the received radiance signal. This table summarizes the *rmse* of the recovery process for each reflectance area in the hyper-spectral polygon, and lists the two main identified reflectances for each category in the cube, together with their local fraction  $F$  and the global misidentification fraction  $F_m$ . The table excludes the assessment of water, fallow fields, wet red clay and potatoes, all of which have fewer than 100 pixels in the hyper spectral cube, and therefore their stochastic assessment is meaningless.

Tables A.11–A.13 summarize the identification process for incorrect assumptions about the visibility conditions during acquisition time. The simulation parameters include  $\theta_z = 30^\circ$ , 10% perturbation of  $\rho(x, y, \lambda)$ , 10% perturbation of  $E$ , 10% perturbation of  $L_p(x, y, \lambda)$ , a spatial spread factor of  $s = 3$ , and a random sensor noise  $n_{\Phi_i}$  of 5% of the received radiance signal. Camera parameters include an optical index of  $\sigma_g(\lambda_i) = 0.6$  and an electronic noise with a SNR of 64 across the spectral bands.

Category	Assumed $V = 5\text{km}$				Assumed $V = 10\text{km}$				Assumed $V = 15\text{km}$				Assumed $V = 23\text{km}$			
	$\varepsilon$	Identified mainly as	$F$	$F_m$	$\varepsilon$	Identified mainly as	$F$	$F_m$	$\varepsilon$	Identified mainly as	$F$	$F_m$	$\varepsilon$	Identified mainly as	$F$	$F_m$
Barley	0.45	Gypsum	0.44	0.92	0.16	Barley	0.95	0.05	0.11	Barley	0.84	0.16	0.14	Oats	0.64	0.72
		Powell	0.28			Powell	0.01			Oats	0.10			Barley	0.28	
Beans	0.44	Potatoes	0.49	0.89	0.15	Beans	0.95	0.05	0.11	Beans	0.87	0.13	0.14	Beans	0.62	0.38
		Gypsum	0.36			Soybeans	0.02			Oats	0.07			Oats	0.31	
Oats	0.47	Potatoes	0.80	0.97	0.17	Barley	0.82	0.99	0.11	Oats	0.89	0.11	0.12	Oats	0.95	0.05
		Basalt	0.06			Beans	0.10			Barley	0.06			Powell	0.03	
Wheat	0.44	Sycamore	0.45	0.74	0.17	Wheat	0.96	0.04	0.15	Wheat	0.96	0.04	0.17	Wheat	0.95	0.05
		Tobacco	0.26			D. sand	0.02			D. sand	0.03			D. sand	0.04	
Silver Maple	0.45	Oak	0.90	1.0	0.19	Maple	0.89	0.11	0.15	Maple	0.95	0.05	0.17	Maple	0.97	0.03
		Elm	0.04			Sycamore	0.08			Wheat	0.04			Wheat	0.02	
Burr Oak	0.51	Silicon	0.91	0.95	0.34	Oak	0.96	0.04	0.38	Oak	0.68	0.32	0.44	Sycamore	0.59	0.69
		Oak	0.05			Sycamore	0.02			Sycamore	0.30			Oak	0.31	
Gypsum sand	0.27	Gypsum	0.996	0.004	0.19	Gypsum	0.997	0.003	0.18	Gypsum	0.997	0.003	0.19	Gypsum	0.997	0.003
		D. sand	0.002			D. sand	0.002			D. sand	0.002			D. sand	0.002	
Silicon sand	0.50	Silicon	0.998	0.002	0.32	Silicon	0.998	0.002	0.31	Silicon	0.996	0.004	0.34	Silicon	0.995	0.005
		D. sand	0.002			D. sand	0.002			D. sand	0.004			D. sand	0.005	
Multi-mineral	0.41	Gypsum	0.52	0.78	0.15	M. Min	0.82	0.16	0.14	M. Min	0.60	0.40	0.19	W. sand	0.52	0.61
		M. Min	0.22			W. sand	0.10			W. sand	0.32			M. Min	0.39	
Whitley soil	0.44	Whitley	0.92	0.08	0.14	Whitley	0.92	0.08	0.08	Whitley	0.94	0.06	0.10	Whitley	0.94	0.06
		Oats	0.03			Barley	0.06			Oats	0.04			Oats	0.04	
Global	0.41			0.41	0.22			0.05	0.21			0.07	0.23			0.17

Table A.11: The sensitivity of the Richter technique to incorrect visibility assumptions for actual visibility of 15km.

Category	True $V = 5\text{km}$				True $V = 10\text{km}$				True $V = 15\text{km}$				True $V = 23\text{km}$			
	$\varepsilon$	Identified mainly as	$F$	$F_m$	$\varepsilon$	Identified mainly as	$F$	$F_m$	$\varepsilon$	Identified mainly as	$F$	$F_m$	$\varepsilon$	Identified mainly as	$F$	$F_m$
Barley	0.41	Basalt	0.49	1.0	0.20	Oats	0.89	1.0	0.11	Barley	0.84	0.16	0.14	Barley	0.94	0.06
		Powell	0.48			Powell	0.05			Oats	0.10			Powell	0.01	
Beans	0.42	Elm	0.69	1.0	0.21	Oats	0.82	0.99	0.11	Beans	0.87	0.13	0.13	Beans	0.95	0.05
		Powell	0.26			Elm	0.12			Oats	0.07			Powell	0.01	
Oats	0.34	Basalt	0.77	1.0	0.17	Oats	0.95	0.05	0.11	Oats	0.89	0.11	0.15	Barley	0.80	0.92
		Powell	0.20			Powell	0.03			Barley	0.06			Beans	0.08	
Wheat	0.47	Powell	0.80	1.0	0.26	Wheat	0.95	0.05	0.15	Wheat	0.96	0.04	0.16	Wheat	0.96	0.04
		D. sand	0.19			D. sand	0.05			D. sand	0.03			D. sand	0.02	
Silver Maple	0.41	Powell	0.72	0.82	0.24	Maple	0.98	0.02	0.15	Maple	0.95	0.05	0.17	Maple	0.90	0.10
		Maple	0.18			Wheat	0.01			Wheat	0.04			Wheat	0.05	
Burr Oak	0.82	D R clay	0.70	1.0	0.54	Sycamore	0.69	1.0	0.38	Oak	0.68	0.32	0.34	Oak	0.95	0.05
		Elm	0.21			Elm	0.13			Sycamore	0.30			Sycamore	0.03	
Gypsum sand	0.39	Gypsum	0.998	0.002	0.30	Gypsum	0.997	0.004	0.18	Gypsum	0.997	0.003	0.18	Gypsum	0.997	0.003
		Silicon	0.001			D. sand	0.002			D. sand	0.002			D. sand	0.002	
Silicon sand	0.69	Silicon	0.99	0.01	0.49	Silicon	0.995	0.005	0.31	Silicon	0.996	0.004	0.31	Silicon	0.998	0.002
		D. sand	0.01			D. sand	0.005			D. sand	0.004			D. sand	0.002	
Multi-mineral	0.52	W. sand	0.56	1.0	0.26	W. sand	0.84	0.97	0.14	M. Min	0.60	0.40	0.12	M. Min	0.87	0.13
		Basalt	0.39			Basalt	0.10			W. sand	0.32			W. sand	0.06	
Whitley soil	0.33	Basalt	0.97	1.0	0.14	Whitley	0.94	0.06	0.08	Whitley	0.94	0.06	0.11	Whitley	0.93	0.07
		Powell	0.02			Oats	0.03			Oats	0.04			Barley	0.05	
Global	0.45			0.59	0.30			0.31	0.21			0.07	0.21			0.04

Table A.12: The sensitivity of the Richter technique to an incorrect visibility assumption of 15km.

Category	True $V = 5\text{km}$				True $V = 10\text{km}$				True $V = 15\text{km}$				True $V = 23\text{km}$			
	$\varepsilon$	Identified mainly as	$F$	$F_m$	$\varepsilon$	Identified mainly as	$F$	$F_m$	$\varepsilon$	Identified mainly as	$F$	$F_m$	$\varepsilon$	Identified mainly as	$F$	$F_m$
Barley	0.19	Barley	0.80	0.20	0.36	Oats	0.73	0.82	0.50	Gypsum	0.49	0.99	0.61	Gypsum	0.89	0.99
		Oats	0.09			Barley	0.18			Powell	0.31			Silicon	0.05	
Beans	0.20	Beans	0.67	0.23	0.35	Potatoes	0.64	0.69	0.49	Gypsum	0.54	0.99	0.61	Gypsum	0.90	0.99
		Oats	0.09			Beans	0.31			Potatoes	0.39			Silicon	0.05	
Oats	0.17	Oats	0.84	0.16	0.36	Beans	0.77	0.94	0.46	Potatoes	0.75	0.93	0.54	Potatoes	0.70	0.99
		Powell	0.20			Barley	0.12			Oats	0.07			Gypsum	0.23	
Wheat	0.27	Wheat	0.91	0.09	0.37	Tobacco	0.85	0.92	0.50	Sycamore	0.42	0.59	0.61	Wheat	0.76	0.24
		D R clay	0.05			Wheat	0.08			Wheat	0.41			Silicon	0.16	
Silver Maple	0.26	Maple	0.94	0.06	0.38	Sycamore	0.68	0.99	0.47	Oak	0.85	0.99	0.54	Oak	0.79	0.98
		Wheat	0.05			Oak	0.27			Sycamore	0.06			Elm	0.08	
Burr Oak	0.53	Sycamore	0.48	0.56	0.50	Silicon	0.60	0.73	0.62	Silicon	0.98	0.99	0.76	Silicon	0.99	1.0
		Oak	0.44			Oak	0.27			Elm	0.01			Wheat	0.005	
Gypsum sand	0.34	Gypsum	0.997	0.003	0.31	Gypsum	0.997	0.003	0.34	Gypsum	0.993	0.007	0.39	Gypsum	0.94	0.06
		D. sand	0.002			D. sand	0.002			Silicon	0.004			Silicon	0.06	
Silicon sand	0.54	Silicon	0.993	0.007	0.53	Silicon	0.997	0.003	0.61	Silicon	0.999	0.001	0.73	Silicon	1.0	0.0
		D. sand	0.007			D. sand	0.003			D. sand	0.001					
Multi-mineral	0.24	M. Min	0.53	0.47	0.31	Basalt	0.44	0.61	0.48	Gypsum	0.71	0.97	0.62	Gypsum	0.79	0.98
		W. sand	0.28			M. Min	0.39			Basalt	0.21			Silicon	0.12	
Whitley soil	0.14	Whitley	0.91	0.09	0.34	W R clay	0.95	0.98	0.44	Whitley	0.90	0.10	0.52	Basalt	0.71	0.78
		Oats	0.06			Whitley	0.02			W. sand	0.04			Whitley	0.22	
Global	0.32			0.11	0.37			0.51	0.46			0.42	0.56			0.48

Table A.13: The sensitivity of the Richter technique to an incorrect visibility assumption of 5km.

## References

- [1] *PcModWin User manual* Version 3.7, 1998. Ontar Corporation.
- [2] *Users' Guide to LOWTRAN-7*. AFGL-TR-88-0177, 1988.
- [3] D. E. Bowker, R. E. Davis, W. Von Ofenheim and D. L. Myrick, "Estimation of spectral reflectance signatures from spectral reflectance profiles," *Proc. of the seventh Inter. Symp. on Remote Sensing of Environment*, vol. II, pp. 795-814, 1983.
- [4] D. E. Bowker, R. E. Davis, D. L. Myrick, K. Stacy and W. T. Jones, "Spectral reflectance of natural targets for use in remote sensing studies", NASA RP-1139, 1985.
- [5] R. Richter, "A fast atmospheric correction algorithm applied to Landsat TM images," *Int. J. Remote Sensing*, vol. 11, pp. 159-166, 1990.
- [6] R. Richter, "A spatially adaptive fast atmospheric correction algorithm," *Int. J. Remote Sensing*, vol. 17, pp. 1201-1214, 1996.
- [7] P. N. Slater, *Remote Sensing: Optics and Optical Systems*, Addison-Wesley Publishing Company, 1980.
- [8] F. O. Huck, R. E. Davis, S. K. Park, R. M. Aherron and R. F. Arduini, "Computational Modeling for the study of multispectral sensor systems and concepts," *Opt. Eng.*, vol. 21, pp. 519-527, 1982.
- [9] F. O. Huck, R. E. Davis, S. K. Park, R. M. Aherron, R. F. Arduini and R. W. Samms, "Study on remote sensor responses and data processing algorithms for feature classification," *Opt. Eng.*, vol. 23, pp. 650-666, 1984.
- [10] N. S. Kopeika, *A system Engineering Approach to Imaging*, SPIE Optical Engineering Press, 1998.
- [11] Y. J. Kaufman, "Atmospheric effects on spatial resolution of surface imagery," *Applied Optics*, vol. 23, pp. 3400-3408, 1984.
- [12] F. O. Huck, C. L. Fales, R. E. Davis and R. Alter-Gartenberg, "Visual Communication with Retinex Coding", *App. Opt.*, April 2000.
- [13] E. Land, "An alternative technique for the computation of the designator in the Retinex theory of color vision," *Proc. Nat. Acad. Sci*, vol. 83, pp. 3078-3080, 1986.

<b>REPORT DOCUMENTATION PAGE</b>			Form Approved OMB No. 0704-0188	
Public reporting burden for this collection of information is estimated to average 1 hour per response, including the time for reviewing instructions, searching existing data sources, gathering and maintaining the data needed, and completing and reviewing the collection of information. Send comments regarding this burden estimate or any other aspect of this collection of information, including suggestions for reducing this burden, to Washington Headquarters Services, Directorate for Information Operations and Reports, 1215 Jefferson Davis Highway, Suite 1204, Arlington, VA 22202-4302, and to the Office of Management and Budget, Paperwork Reduction Project (0704-0188), Washington, DC 20503.				
<b>1. AGENCY USE ONLY</b> (Leave blank)		<b>2. REPORT DATE</b> May 2000		<b>3. REPORT TYPE AND DATES COVERED</b> Contractor Report
<b>4. TITLE AND SUBTITLE</b> Identification of Terrestrial Reflectance From Remote Sensing			<b>5. FUNDING NUMBERS</b>  C NAS1-20431 WU 258-70-21-16	
<b>6. AUTHOR(S)</b> Rachel Alter-Gartenberg Scott R. Nolf				
<b>7. PERFORMING ORGANIZATION NAME(S) AND ADDRESS(ES)</b>  Computer Sciences Corporation 3217 N. Armistead Ave. Hampton, virginia 23666			<b>8. PERFORMING ORGANIZATION REPORT NUMBER</b>	
<b>9. SPONSORING/MONITORING AGENCY NAME(S) AND ADDRESS(ES)</b> National Aeronautics and Space Administration Langley Research Center Hampton, VA 23681-2199			<b>10. SPONSORING/MONITORING AGENCY REPORT NUMBER</b>  NASA/CR-2000-210116	
<b>11. SUPPLEMENTARY NOTES</b> Langley Technical monitor: Kathryn Stacy Langley Subtask Managers: Richard E. Davis Friedrich O. Huck				
<b>12a. DISTRIBUTION/AVAILABILITY STATEMENT</b> Unclassified-Unlimited Subject Category 43                      Distribution: Standard Availability: NASA CASI (301) 621-0390			<b>12b. DISTRIBUTION CODE</b>	
<b>13. ABSTRACT</b> (Maximum 200 words) Correcting for atmospheric effects is an essential part of surface-reflectance recovery from radiance measurements. Model-based atmospheric correction techniques enable an accurate identification and classification of terrestrial reflectances from multi-spectral imagery. Successful and efficient removal of atmospheric effects from remote-sensing data is a key factor in the success of Earth observation missions. This report assesses the performance, robustness and sensitivity of two atmospheric-correction and reflectance-recovery techniques as part of an end-to-end simulation of hyper-spectral acquisition, identification and classification.				
<b>14. SUBJECT TERMS</b> Remote sensing, Hyper-spectral imagery, Terrestrial reflectance recovery, Identification, Classification			<b>15. NUMBER OF PAGES</b> 80	
			<b>16. PRICE CODE</b> A05	
<b>17. SECURITY CLASSIFICATION OF REPORT</b> Unclassified	<b>18. SECURITY CLASSIFICATION OF THIS PAGE</b> Unclassified	<b>19. SECURITY CLASSIFICATION OF ABSTRACT</b> Unclassified	<b>20. LIMITATION OF ABSTRACT</b> UL	